NTNU

Norwegian University of
Science and Technology

Computation of impinging gas jets

Eirik Martin Stuland

Master of Science in Product Design and Manufacturing
Submission date: June 2008
Supervisor: Helge Ingolf Andersson, EPT

Norwegian University of Science and Technology
Department of Energy and Process Engineering

Problem Description

Master Thesis

Eirik Martin Stuland

Spring 2008

Computation of Impinging Gas Jets

(Beregning av kolliderende gasstråler)

Background

CFD (Computational Fluid Dynamics) plays an important role in the development and improvement of complex industrial flow and energy processes. Gas jets that impinge on solid surfaces are a commonly used means of influencing and/or controlling quantities related to cooling, heating, or drying.
The impingement area is characterized by complex flow conditions, bearing importance to the practical applications of the impinging gas-jet geometry.
These conditions can with benefit be investigated by means of CFD, where both velocity and temperature related phenomena can be thought of as relevant quantities for investigation.
Likewise, the nozzle heigth and angle relative to the impingement plane are important quantities that affect the flow.
Resulting from the chosen physical and geometrical parameters, the numerical parameters like the domain size, grid size and choice of turbulence model, will affect the computational results.

Goal
Flowrelated parameters shall be computed for impinging gas jets. It shall also be investigated how the aforementioned parameters influence the computational results. The work will serve as a background experience for future computations, and shall therefore result in recommendations for e.g. what turbulence models, grid sizes etc that should be used for similar cases.

The thesis will be produced based on the following points:

1.   The commercial software FLUENT shall be used.
2.   Validation of CFD code against a representative referance case.
3.   Choice of, and reasoning for approach: RANS, URANS and/or LES.
4.   Choise of computational domain and mesh.
5.   Presentation, comparison and discussion of the computed cases.

Abstract

This dissertation has been produced during the spring semester of 2008 to serve to the requirements for the degree of "Master of Technology" at the Norwegian University of Science and Technology (NTNU).
The thesis has been written at the department of Energy and Process Engineering, with supervision of Professor Helge I. Andersson from the Fluid Dynamics department.

The thesis has the title "Computation of Impinging Gas Jets", and aims to investigate the Impinging Jet Flow (IJF) problem presented in section[2] by means of Computational Fluid Dynamics (CFD).
For the work of this thesis the commercially available program package of FLUENT 6.3, and Gambit 2.4 was used for all the simulation and geometry generation tasks.

The specific IJF case treated in the thesis work, is the Single Round Nozzle (SRN) IJF geometry explained in section[2.2] , and displayed in Figure 2.2 .
The numerical simulations were carried out by means of 2D and 3D Reynolds Averaged Navier Stokes (RANS) simulations , and Large Eddy Simulation (LES) with related theory described in the theory section[3].

The work with the simulations of this thesis can roughly be divided into two main components.
Firstly there is the part comprising all tasks and operations involved in creating and running the simulations, about which relevant information is provided in section[4].

Secondly, there is the work involving all the tasks related to gathering, interpreting, and analyzing the yielded simulation results.
These tasks and their results are mainly treated in sections[5 to 9].

Both numerical and experimental reference IJF cases were used in this thesis work.
The reference cases were at first used to guide the beginning of the simulation effort (Figure 6.1).
In the later stages of the thesis, the reference results were used to analyze and interpret the results of the thesis simulations.

Overall the results from the RANS simulations of this thesis, are found to give good agreement with the reference simulations and experiments, within the limits of what can be expected from the RNG k-ε model which was used.
The LES simulations on the other hand, proves to be far more demanding both computation wise, and in relation to issues concerning simulation preparations and setup.
In addition the LES simulation is found to be outperformed by the RANS simulations in some regions of the IJF geometry.
When analyzed, it is found that this is probably caused by an unfortunate combination of regions with low local mesh quality, and a quite mesh sensitive feature in the Sub Grid Scale model.
Nevertheless the LES simulation is found to provide results of good agreement with experimental data in some of the most difficult regions to simulate on the IJF geometry.
In this region the LES simulation is also found to outperform the RANS simulations.

Sammendrag

Denne avhandlingen er skrevet i løpet av vårsemesteret 2008, for å tilfredsstille kravene som stilles for oppnåelse av graden "Master of Technology".
Oppgaven er skrevet ved institutt for energi og prosessteknikk, under veiledning av Helge I Andersson, fra strømningsteknisk institutt.

Oppgaven har tittelen "Beregning av kolliderende gasstråler", og har som mål å undersøke problemet med kolliderende gasstråler som er beskrevet i seksjon[2], ved hjelp av Numerisk Strømnings Beregninger (CFD).
Simuleringsarbeidet i oppgaven er utført ved hjelp av den kommersielt tilgjengelige programpakken FLUENT6.3,og GAMBIT 2.4.

Den spesifike geometrien som er behandlet i oppgaven, består av en enkel rund dyse, som sender ut en gassjet, vinkelrett mot en flat plate, som beskrevet i seksjon[2.2], og figur[2.2].
De numeriske simuleringene ble utført på både 2 og 3dimensjonale geometrier ved hjelp av Reynolds Midlet Navier Stokes (RANS) simuleringer, og LES simuleringer nærmere beskrevet i seksjon[3].

Simulerings arbeidet med denne oppgaven kan deles inn i to hoved deler:
Først er det den delen som består av alle oppgaver relatert til å igangsette, og kjøre de numeriske beregningene, nærmere beskrevet i seksjon[4].

Dernest er det den delen som innbefatter alle oppgaver forbundet med innhenting, tolkning, og analysering av simulerings resultatene, beskrevet mer i detalj i seksjon[5 og 9].

Både numeriske og eksperimentelle referanse studier av den aktuelle gasstrømmen ble funnet og anvendt til å igangsette og sammenligne simuleringene fra prosjektet.

Totalt sett viser RANS simuleringene fra dette prosjektet god overensstemmelse med eksperimenter, og referanse simuleringer, i forhold til det som kan forventes av den anvendte RNG k-ε turbulens modellen.
LES simuleringene viser seg å være mye mer krevende, både med tanke på krav til datakraft, og med tanke på forhold knyttet til simulerings forberedelse og oppsett.
I tillegg viste RANS simuleringene seg å gi bedre resultater i noen soner innenfor beregnings området.
Når simuleringene ble analysert, ble det funnet at de "dårlige" resultatene fra LES beregningene kan skyldes en uheldig kombinasjon av lokalt lav kvalitet på beregnings gridet, kombinert med en grid sensitiv egenskap i modelleringen av småskala turbulens i LES beregningene.
Likevel ga LES simuleringene gode resultater i noen av de områdene av geometrien, som regnes som de vanskeligste å beregne.
I disse områdene ga LES simuleringene bedre resultater enn RANS simuleringene.

1 Table of contents

Nomenclature:

l	mixing length
N	Newtons $[=] \frac{kg \cdot m}{s^2}$
p	pressure
e	specific internal energy $[=] \frac{Nm}{kg}$
h	specific enthalpy $= e + \frac{p}{\rho}$
c_p	Heat capacity $= \left.\frac{\partial h}{\partial T}\right|_p$
$[=]$	Quantity has the dimension
D	Nozzle outlet diameter
r	radial distance away from nozzle centre axis
R	Maximum domain radius
$R_{\frac{1}{2}}$	Radius at half of the domains maximum radius
H	height of nozzle above impingement plane
u	total velocity in radial direction $\quad u = \bar{u} + u'$
v	total velocity in axial direction $\quad v = \bar{v} + v'$
u'	(RANS)fluctuating velocity in radial direction
v'	(RANS)fluctuating velocity in axial direction
$\bar{u}$	(RANS)time averaged velocity radial direction
$\bar{v}$	(RANS)time averaged velocity axial direction
$\overline{u_i u_j}$	(RANS)Reynolds stress tensor
u'	(LES) SGS velocity in radial direction
v'	(LES) SGS velocity in axial direction
$\bar{u}$	(LES) filtered velocity radial direction
$\bar{v}$	(LES) filtered velocity axial direction
T	temperature
U_b	Bulk velocity (mean nozzle outlet velocity) = 3.45 m/s
U	Mean velocity
Pr	Prandtl number $Pr = \frac{\mu c_p}{k}$
Nu	Nusselt number
Re	Reynolds number
Re_0	Reynolds number at nozzle outlet
y^+	Dimensionless length scale
u^+	Dimensionless velocity scale
u_*	Friction velocity
κ	Kármán constant ≈0.40 - 0.41
l_s	Subgrid mixing length
σ	Stress
τ_{ij}	Stress tensor
δ	Boundary layer thickness
δ_{ij}	Kronecker delta operator $= \begin{cases} 1 \text{ for } i = j \\ 0 \text{ otherwise} \end{cases}$
ε	Turbulent dissipation $[=]\frac{m^2}{s^3}$
k	turbulent kinetic energy $= \frac{1}{2}\overline{u'_i u'_i}$ $[=]\frac{m^2}{s^2}$

S_{ij} Mean deformation velocity $= \frac{1}{2}\left(\frac{\partial u_i}{\partial x_j} + \frac{\partial u_j}{\partial x_i}\right)$

Terms And Abbreviations:

GB	Giga Byte (10^6 bytes)
NS	Navier Stokes(equations[xx-xx])
DNS	Direct Numerical simulation
LES	Large Eddy Simulation
RANS	Reynolds Averaged Navier Stokes
URANS	Unsteady Reynolds Averaged Navier Stokes
SRN	Single Round Nozzle
SGS	SubGrid Scale
SGSRS	SubGrid Scale Reynolds Stress
S-L	Smagorinsky-Lilly SGS model
SSN	Single Slot Nozzle
IJF	Impinging Jet Flow
K	Kilo: denotes thousand e.g. 10 000 =10K
M	Million: denotes millions e.g. 10 000 000=10M
RST	Reynolds Stress
RNG	Renormalisation Group
O( )	Denotes order of magnitude
eq[]	Equation citation
Fig[]	Figure citation
Ref[]	Reference citation

Preface

This master thesis concludes my work on the topic "Impinging Jet Flow" at NTNU during the spring semester of 2008.
 In addition the work itself, the thesis also brings a conclusion to five years of technology studies at NTNU, the last of which were spent studying subjects related to process engineering and Fluid Dynamics.
My specialization has been in numerical computation and turbulence physics, thus making CFD a relevant area for my master thesis.

The thesis has been written in the program package Office 2007 which, in comparison to earlier Office versions, has performed excellently except for some minor problems related to working with plots and graphics. These issues however "minor", sometimes took hours to work around and at times caused <u>major</u> frustration.

The writing of a master thesis has proved a new experience, and while the previous nine semesters at NTNU at times have been rather hectic, this last semester has allowed for a kind of concentrated and focused effort previously unfamiliar to me.
Admittedly the freedom to define my own investigations and progress has at times appeared somewhat disconcerting.
In this respect the steady guidance of my advisor Helge I. Andersson has been of great use, helping to direct the work effort in a purposeful direction.
He has been of great help in coming up with ideas for further investigations when I was confused or at a loss.
He has also helped in leading the thesis work on a "steady course".
Helge I. Andersson has also proved to be of great help in contributing with a well of experience and knowledge about issues related to CFD or general fluid dynamics.

Introduction

This thesis reports the work related to the numerical simulation and post simulation analysis of a Single Round Nozzle Impinging Jet Flow geometry (Figure 2.2).
The simulations have been conducted by means of LES and RANS computations, and have been analyzed and compared to relevant theory and earlier published reference studies.

The thesis starts with an introductory section about the Impinging Jet Flow, and an explanation of the geometry chosen for the simulations of this thesis.

In the following section, theory relevant to the understanding the background for the analysis and discussion coming in later sections is presented.
The theory section may also be of help in understanding the physics of the Impinging Jet Flow.
 Some basic concepts explaining how the involved physics are dealt with computation wise, are also presented .

After the Theory section follows a section describing the tasks and operations involved in creating and running the simulations. This section describes the reference work, the computer and simulation setup, the mesh generation, and the initial and boundary conditions.

Thereafter there come four sections, respectively treating the gathering, processing and compilation, observation, and discussion of post simulation data.
In short these sections deal with the treatment, analysis, and interpretation of the finished simulation results.

After these four sections, a section follows where overall conclusions are drawn based on observations and discussions of the previous sections, after which follows a section with suggestions for further work and improvements.

2   The Impinging Jet Flow

In the following section, the Impinging Jet Flow will be explained with regards to different variants, reasons for scientific and practical interest, and practical applications. Then the Impinging Jet Flow version to be studied in this thesis is presented along with its reference coordinate system, and a general description of how the flow develops for the Impinging Jet Flow.

2.1   About the Impinging jet flow:

The impinging jet flow (IJF) problem has previously been a case of interest mostly due to the research of heat transfer phenomena. This interest has been based on the high heat transfer characteristics of the IJF, having a number of practical application both for scientific and industrial applications, where the IJF setup has been used for heating, cooling, and drying purposes.

More recently the IJF case has awakened a new interest for other purposes.
With the past years rapid increase in available computer power, the application of Computational Fluid Dynamics (CFD) is being applied and tested on an ever increasing number of flow problems.
The IJF problem has been found to provide a good test ground for CFD codes and models.
The IJF has been found to be especially useful for the testing of turbulence models, since the simple IJF geometry brings about a number of not so simple flow phenomena.
For instance the IJF flow involves a jet-flow with its inherent wake development, entrainment, shear and mixing layer development.
Then the jet stagnates against a flat plate, and disperses orthogonally to the jet axis, where a wall jet type of flow is reached at some distance downstream of the impingement point.
In other words the IJF problem involves shear, mixing, stagnation, entrainment, and near wall flows, all in a relatively simple geometry.

There are also different variants of the impinging jet flow, each bringing about new interesting flow phenomena to be investigated. Some of the main variants are
- Single Slot Nozzle(SSN)
- Single Round Nozzle(SRN)
- Array of Round Nozzles(ARN)
- Array of Slot Nozzles (ASN)

In addition, different variants of all the above geometries can be made by changing the inflow axis angle relative to the impingement plane. The IJF flow has also been investigated with the use of a moving impingement plane.
The latter bearing interest for industrial applications like the cooling of metal sheets in production. Anyone having been to a mechanized car-washer, will probably remember the drying mechanism resembling some variety of the SSN geometry.
Among other practical applications for the IJF cases are:
- Cooling of microchips
- Industrial drying processes

- Defrosting of Aeroplanes
- Vertical Lift off and landing of certain fighter jet planes like the F22 or the Harrier Jump jet.

Obviously the IJF comes in many variants and disguises.

In this thesis however, only the Single Round Nozzle (SRN) IJF case as explained in section[2.2] will be treated.

2.2   The Impinging jet flow topography:

The Impinging Jet Flow (IJF) problem is a geometry where a jet exits from a nozzle from where it develops approximately like a free jet-flow for some distance, before it impinges on (collides with) a flat plate referred to as the "impingement plane".

Upon impingement the flow disperses to create a flow moving along the impingement plane. Outside what ref[4] refers to as the impingement zone , the dispersed flow takes on the characteristics of a wall jet like visualized in Figure 2.1. For the SRN variant of the IJF case the ref[4] defines the impingement region to extend to $\frac{r}{D} \approx 3$, outside of which the flow takes on the characteristics of an axis symmetrical wall jet.
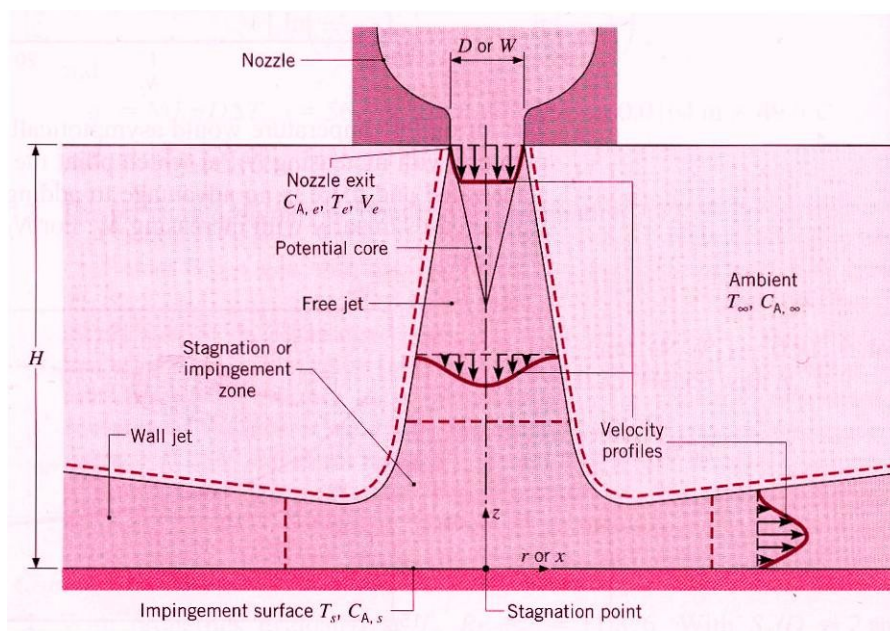

Figure 2.1
Impinging Jet Flow geometry from ref[12]

In this thesis, the geometry used for all simulations and reference work is the Single Round Nozzle (SRN) type displayed in Figure 2.1 and Figure 2.2, and described in this section[2]. The same geometry is also of the SRN type for all reference simulations (ref[6 and 8]), and the experiments of ref[4].

As a result of emphasis refs[4, 6 and 8] puts on the geometry where $\frac{H}{D} = 2$, all the simulations of this thesis are made on geometries where $\frac{H}{D} = 2$.

Further the jet exit nozzle (**J**) is oriented perpendicularly to the impingement plane (**I**) for all mentioned reference work, and all the simulations of this study/ thesis.
An overview of the data for the geometries of this thesis are displayed in Table 2.1.
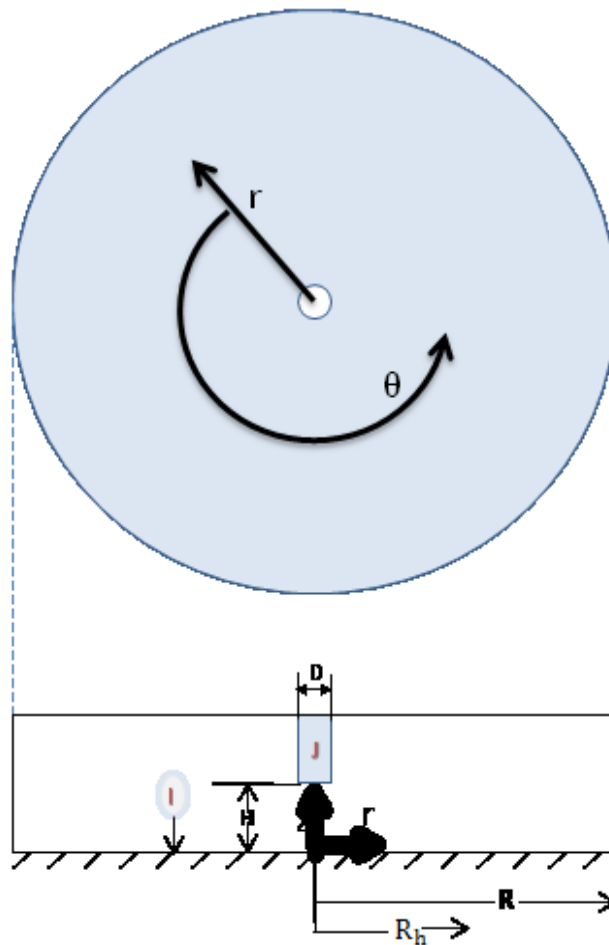

Figure 2.2
Figure 2.2 displays the geometry used for the simulations of this thesis, with the coordinate system used to refer the geometry in the following discussions.

Figure symbol explanation:
D   Jet nozzle diameter
I   impingement plane
H   Nozzle-exit height over impingement plane
J   Jet exit nozzle
z   symmetry axis of geometry, perpendicular to the impingement plane
r   radial direction normal to z axis
θ   Direction normal to radial direction
R   Total maximum Radius of domain
R_h Half of total maximum Radius of domain

Geometry table				
$\dfrac{H}{D}$	$\dfrac{R}{D}$	D	U_b	Re_0
2	9	0.1[m]	3.45 [m/s]	23K / 230K

Table 2.1
Table 2.1 provides the tabulated spec of the SNR geometry of this thesis:

3 Theory

In the following sections, relevant theory to the thesis work is presented.

3.1 On Turbulence

Turbulence and its implications are important for the work done in this thesis.
A large part of the theory section will therefore be devoted to turbulence and turbulence related topics.
In this section an introduction to turbulence as phenomena will be given.
Then in the following sections[3.2 - 3.5] more elaborated theory and descriptions will be given on the phenomenon.
Relevant related topics will also be treated in appendices [B & D].

Characteristic features:
There is no absolute definition that defines the phenomenon of turbulence exactly. However turbulent flows inhere certain characteristic features that helps to recognize a turbulent flow.
Turbulent flows are ref[7]:

- Irregular and random, often with a high signal to noise ratio. This irregular behaviour prevents a deterministic prediction of turbulent movements. I.e. turbulent movements cannot for instance be exactly calculated by analytical means.

- Diffusive: Turbulence acts to mix and diffuse quantities and properties affiliated with the flow. For instance smell and heat is distributed more quickly with a turbulent flow.

- Occurs at high Reynolds numbers: Reynolds numbers (Re) are ratios of impulse related forces to viscosity related forces. Turbulent flows occur when a critical threshold in this ratio is surpassed.

- Three dimensional: Turbulence is a phenomenon of the real world, fluctuating randomly in all coordinate directions. Otherwise turbulence would not be truly irregular and diffusive.

- Dissipative process: Turbulence dissipates the energy of the mean flow through a cascading process of larger eddies generating ever smaller eddies. The energy from this process eventually dissipates as heat or noise. In order to maintain a turbulent flow, a continual supply of energy from the mean flow is therefore required.

- Continuum: Turbulence occurs in fluids. Fluid can be treated as continuums, hence an event somewhere in the flow, will affect the rest of the flow.

- Flow phenomena not fluid property: As a flow can pass from laminar to turbulent and back again, it is clear that turbulence is not a fluid property, but a phenomena occurring for certain flow conditions.

3.2 The Navier Stokes (NS) equations

The governing equations for fluid motions and energy, can be expressed like eq 3.1 - eq 3.3. These equations are called the Navier Stokes (NS) equations, and are a vital part of fluid dynamics.

In computational fluid dynamics (CFD), the NS equations are treated numerically and solved with the use of algorithms like e.g. SIMPLE or SIMPLEC.

In this section, and section[3.5.1], details on approaches to the modelling of turbulence are presented, all of which are closely bound to the NS equations.

The NS equations are therefore first presented in their general tensor-notation form, in order to show the origin of the RANS and filtered NS equations of sections[3.2.1 and 3.53.5.1].

The Navier Stokes (NS) equations:

Continuity: $\quad \frac{\partial \rho}{\partial t} + \frac{\partial (\rho u_i)}{\partial x_i} = 0$

$$\text{eq 3.1}$$

Impulse: $\quad \frac{D(\rho u_i)}{Dt} = -\frac{\partial p}{\partial x_i} + \rho f + \frac{\partial \sigma'_{ij}}{\partial x_j}$

$$\text{eq 3.2}$$

Energy: $\quad \rho \frac{De}{Dt} = \frac{\partial}{\partial x_j}\left(k\frac{\partial T}{\partial x_j}\right) - p\frac{\partial u_i}{\partial x_i} + \sigma'_{ij}\frac{\partial u_i}{\partial x_j}$

$$\text{eq 3.3}$$

(expressed for specific internal energy e).

where $\quad \sigma'_{ij} = \mu\left(\frac{\partial u_i}{\partial x_j} + \frac{\partial u_j}{\partial x_i} - \frac{2}{3}\delta_{ij}\frac{\partial u_k}{\partial x_k}\right)$

$$\text{eq 3.4}$$

, and f is here a field force e.g. gravity or magnetism.

3.2.1 Reynolds time averaging and the RANS equations:

The concepts introduced in this section form the basis for the most common approach to computational fluid dynamics, namely the RANS approach.
RANS is an abbreviation for Reynolds Averaged Navier Stokes. Below follows a brief description of the concept of Reynolds Averaging.

The idea behind Reynolds averaging, is to divide a time varying velocity u into one time averaged velocity component $\bar{u}$, and one fluctuating velocity component u', as shown in Figure 3.1 and Figure 3.2, so that the velocity can be expressed like $u_i = \bar{u}_i + u'_i$ as illustrated by the figures below:
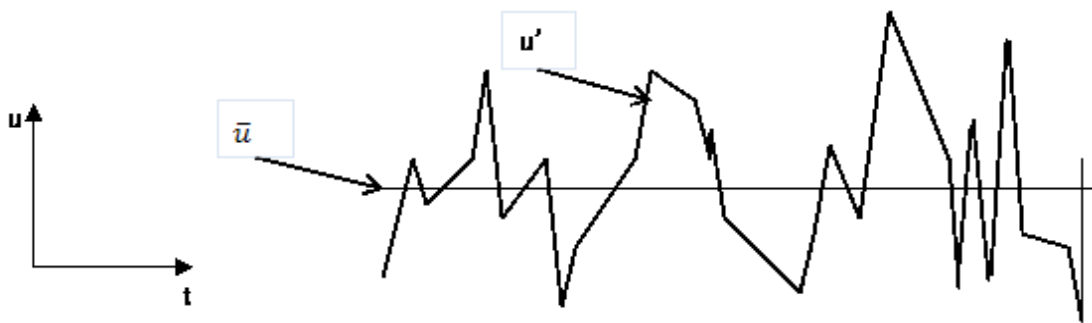

Figure 3.1

$$u_i = \bar{u}_i + u'_i$$

Figure 3.2

The same partition is also introduced for the other variables in the NS equations, e.g. pressure, energy and temperature.
This way of splitting up time varying variables, have a couple of useful features.
Mathematically these features can be displayed as follows for the arbitrary variables f and h:

$$\bar{f} = \frac{1}{T} \int_{t_0}^{t_0+T} f \, dt$$

$$\bar{f'} = 0 \quad \bar{\bar{f}} = \bar{f} \qquad \overline{\bar{f}h} = \bar{f}\bar{h} \qquad \overline{f+g} = \bar{f} + \bar{g} \qquad \overline{f'\bar{h}} = 0$$

$$\frac{\overline{\partial f}}{\partial i} = \frac{\partial \bar{f}}{\partial i} \qquad \overline{fg} = \bar{f}\bar{g} + \overline{f'g'} \qquad \overline{\int f \, di} = \int \bar{f} \, di$$

When inserting $u_i = \bar{u}_i + u'_i$, into the NS equations, the following equations can be deduced with the help of the relations explained with f and g above:

16

For reasons expressed in ref [13] continuity equation can be expressed as:

1) $\frac{\partial \overline{u_i}}{\partial x_i} = 0$

as long as ρ is kept as a non fluctuating quantity.

2) $\rho \frac{D \overline{u_i}}{Dt} = \rho g - \frac{\partial \overline{p}}{\partial x_i} + \frac{\partial}{\partial x_j}\left(\mu \left(\frac{\partial \overline{u_i}}{\partial x_j} + \frac{\partial \overline{u_j}}{\partial x_i}\right) - \rho \overline{u'_i u'_j}\right)$

eq 3.6 and eq 3.7 have been named the Reynolds averaged Navier Stokes equations, or simply the RANS equations.

In RANS simulations, eq 3.6 and eq 3.7 are solved numerically.
RANS simulations have the feature of being well suited for simulation of steady phenomena where only time independent quantities are of interest.
Examples of simulations suited for the RANS approach can be: drag coefficient calculation for a time invariant external flow, e.g. circular cylinder at high Reynolds numbers, or the lift from an aeroplane wing.
When simulated, the RANS equations do not need to describe the three dimensional physics of turbulence directly, since all fluctuations are time averaged (eq 3.7).
Therefore it is possible, and often the best choice, to make a simulation in two dimensions only.
The use of 2D simulation has two major advantages over 3D simulation.
Firstly the often much more complex geometry and grid generation process associated with 3D simulations is avoided.
Secondly the high computational expense and run-time of a 3D simulation, is avoided.
Thus a 2D simulation can often yield an answer to a problem in a quicker and cheaper way than a 3D simulation.
The 2D simulation is nevertheless contingent on the finding of a sensible projection or symmetry plane to represent the 3D problem in two dimensions.

As can be seen from the RANS equations they are similar to the ordinary NS equations, except for the $-\rho \overline{u_i' u_j'}$ term, which is popularly referred to as the Reynolds stresses.
Without the $-\rho \overline{u_i' u_j'}$ term the incompressible (ρ=constant) 3D NS equations have 4 equations and 4 unknown, thus being directly solvable, an approach used in direct numerical simulations or simply DNS, further discussed in section[3.5] and by ref[9].
Of course there is still the issue of the convective terms $u_j \frac{\partial u_i}{\partial x_j}$ preventing the NS equations from being solved by exact analytical means, yet that is a discussion that will be left out from this thesis.

3.2.2 Equation closure:

In order to solve the RANS equations(eq 3.1-eq 3.2) numerically, there is a need for the number of available equations to match the number of variables of the equation set.
By counting the number of available equations for a general 3D problem, the NS equations (eq 3.1 and eq 3.2)consist of the following equations :
    1) Continuity
    2) x-momentum
    3) y-momentum
    4) z-momentum

In other words there are four equations.
By counting the variables, it is found that there are:
    1) Pressure
    2) u (x-velocity)
    3) v (y-velocity)
    4) w (z-velocity)

This poses no problem as long as no new variables are introduced.
However, with the RANS approach, the $\overline{u'_i u'_j}$ term is introduced, which represents the 3x3 tensor of Figure 3.3:

$$\begin{bmatrix} \overline{u'_1 u'_1} & \overline{u'_1 u'_2} & \overline{u'_1 u'_3} \\ \overline{u'_2 u'_1} & \overline{u'_2 u'_2} & \overline{u'_2 u'_3} \\ \overline{u'_3 u'_1} & \overline{u'_3 u'_2} & \overline{u'_3 u'_3} \end{bmatrix}$$

Figure 3.3

Although having 9 elements, only 6 new variables are introduced, since the matrix is symmetrical around the trace $\overline{u'_1 u'_1}$ since $\overline{u'_i u'_j} = \overline{u'_j u'_i}$.
However there are still 6 new variables, which brings the total number of variables of the RANS equations up to 10.
As a result there are but two choices; either to make more equations, or to simplify or collapse the problem variables in some way, so that the number of variables is reduced.
The goal is of course to bring the total number of variables to match the total number of equations, thus rendering the equation set solvable. If this is achieved, the system is said to be closed.
Hence the problem of mismatching number of variables and equations is often referred to as the closure problem.
It is the closure problem which gives rise to the need for turbulence modelling, a problem originating from the need to treat the $\overline{u'_i u'_j}$ term of the RANS equations.
One of the aims of turbulence modelling is to let as few equations and variables as possible, describe as much physics as possible.

3.2.3 Eddy viscosity hypothesis:

One of the simplest approaches to modelling turbulence comes with the introduction of the turbulent viscosity μ_t.

For the 2D case, turbulent shear stress is modelled as:

$$\tau = \mu_t \frac{\partial \bar{u}}{\partial y} = -\rho \overline{u'v'}$$

eq 3.8

Or on the general tensor form:

$$\tau_{ij} = -\rho \overline{u'_i u'_j} = 2\rho \mu_t S_{ij} - \frac{2}{3}\rho k \delta_{ij}$$

eq 3.9

where

$$S_{ij} = \frac{1}{2}\left(\frac{\partial u_i}{\partial x_j} + \frac{\partial u_j}{\partial x_i}\right)$$

eq 3.10

With the introduction of Reynolds averaging the 2D x-momentum RANS equation transforms into

$$\bar{u}\frac{\partial \bar{u}}{\partial x} + \bar{v}\frac{\partial \bar{u}}{\partial y} = -\frac{1}{\rho}\frac{\partial \bar{p}}{\partial x} + \frac{1}{\rho}\frac{\partial}{\partial y}\left((\mu + \mu_t)\frac{\partial \bar{u}}{\partial y}\right)$$

eq 3.11

In other words, the eddy viscosity approach models turbulence by an addition to the laminar viscosity referred to as the turbulent viscosity μ_t.

μ_t can either be set to a constant value, as is the crudest approach to turbulence modeling.

μ_t can in turn be modeled in different ways, like in the k-ε model, where

$\boldsymbol{\mu_t = \rho C_\mu \frac{k^1}{\varepsilon}}$ (appendix[D])

Here k and ε in turn are described with separate differential equations.

For a more comprehensive description of the turbulence models used for the simulations of this thesis, appendix[D] should be consulted

3.3 Near wall flow physics:

The flow close to solid surfaces, are important in all fluid mechanics.
So called wall bounded flows can be associated with many well known, and important phenomena like separation, boundary layer development and transition (laminar-turbulent), and viscous shear stress to mention some.
For the IJF problem, the impingement plane represents a solid surface, thus making near wall flow physics highly relevant. The fact that the IJF geometry both includes free shear flows (jet-flow), and wall bounded flow, or even a combination of the two (wall-jet), are among the reasons why it is viewed as such a good testing ground for computational tools and codes. Hence a short section about near wall flow physics is included in the theory section of this thesis.

In order to describe near wall flow phenomena, it is customary to introduce scaled variables
An important such quantity is the so called friction velocity defined as:

$$u_* = \left(\frac{\tau_w}{\rho}\right)^{\frac{1}{2}} [=] m/s$$

eq 3.12

The friction velocity in turn gives rise to the dimensionless velocity u^+ defined as:

$$u^+ = \frac{\bar{u}}{u_*} [=] 1$$

eq 3.13

The friction velocity also gives rise to the dimensionless length scale y^+ defined as:

$$y^+ = \frac{y \cdot u_*}{\nu} [=] 1$$

eq 3.14

For later use in this section the Prandtl mixing length $l = \kappa y [=] m$, is also introduced.
l is the typical distance an eddy travels vertically, apparently varying constantly with the distance from the wall.

When y^+ is plotted with a logarithmic axis grading against u^+ for any flow close to a solid surface, all the different turbulent boundary profiles described with dimensional coordinates (y, u), collapse into one shared profile described in non dimensional coordinates (y^+, u^+). This shared profile has the well known shape exemplified in Figure 3.4 , taken from reference [3].

As Figure 3.4 taken from ref[3] indicates, any turbulent flow close to a wall can be separated into three main regions:
1. The linear sub layer
2. The log law region
3. The outer layer

According to ref[13] the flow in the linear sub layer follows a linear behavior where $u^+ = y^+$ because in this region molecular shear is the dominating shear contribution.

Between the linear sub layer and the log law region, there is a small region where neither a linear nor a logarithmic profile approximates the profile well. This region is referred to as the buffer layer.

Ref[white viscous] shows the following curve fitting function found by Spalding (1961) which applies from the wall throughout the entire log-law region (i.e. $y^+ \leq 100 - 300$):

$$y^+ = u^+ + e^{-\kappa B}\left(e^{\kappa u^+} - 1 - \kappa u^+ - \frac{(\kappa u^+)^2}{2} - \frac{(\kappa u^+)^3}{6}\right)$$

<u>eq 3.15</u>

Outside of the log-law region, there is no longer any universal u^+ profile curve, since the profile here is affected by the conditions in the flow outside of the boundary layer.

Figure 3.4 applies to all un-separated turbulent boundary layers, thus serving to elucidate their shared physics of flows near solid surfaces.

A perhaps more intuitive representation of what Figure 3.4 describes is exemplified in Figure 3.5, where a non-logarithmic plot using physical variables y and u, instead of dimensionless variables y^+ and u^+, is made.

The profile of Figure 3.4 then turns into a typical boundary layer profile like in Figure 3.5, which is easily interpreted in terms of physical behavior, but lacks the universal validity of the profile of Figure 3.4 where different profiles collapse into one shared dimensionless profile.

In a respect Figure 3.4 and Figure 3.5 complement each other in that Figure 3.4 sets the physics of a turbulent wall bounded flow in a context with other turbulent wall bounded flows, whilst Figure 3.5 shows the velocity profile for a given boundary layer with the perhaps more intuitive variables u and y, compared to the dimensionless variables u^+ and y^+ used in profile of Figure 3.4.
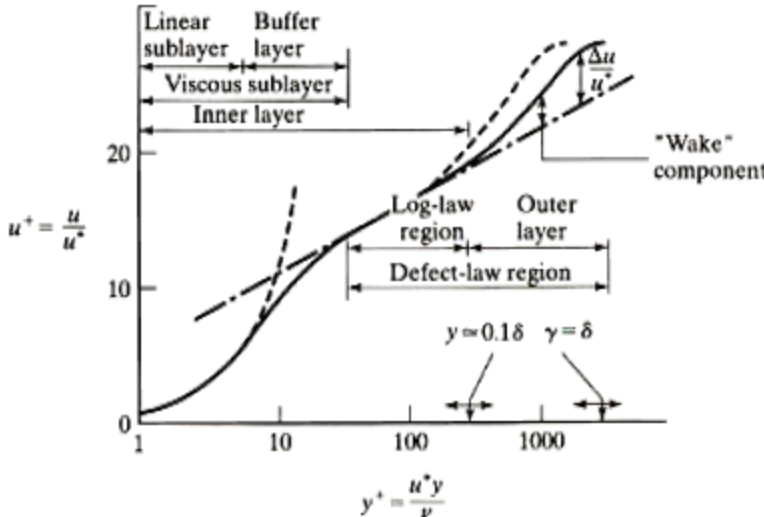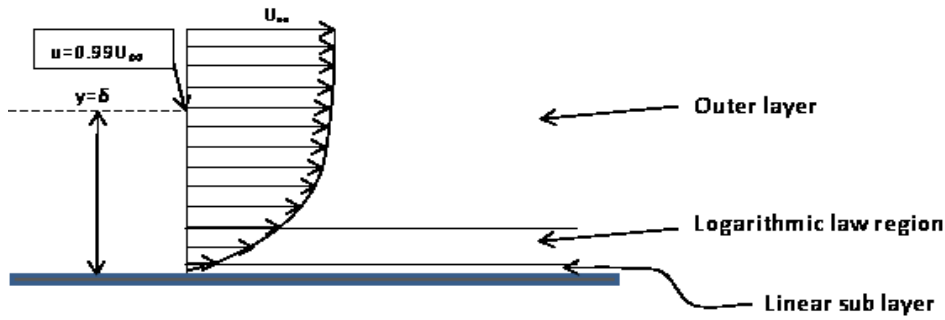

<u>Figure 3.4</u>

21

Figure 3.5

It is worth noting that the logarithmic curve (-·-·-) of Figure 3.4 can be analytically derived as follows:

I. $l = \kappa y$

II. $\mu_t = \rho l^2 \left(\frac{\partial \bar{u}}{\partial y} \right)$

III. $\tau_t = \mu_t \left(\frac{\partial \bar{u}}{\partial y} \right)$

IV. $u_* = \left(\frac{\tau_w}{\rho} \right)^{\frac{1}{2}}$

V. $u^+ = \frac{\bar{u}}{u_*}$

VI. $y^+ = \frac{y \cdot u_*}{\nu}$

III. and II. combines to

VII. $\tau_t = \rho l^2 \left(\frac{\partial \bar{u}}{\partial y} \right)^2$

VII. and IV. combines to

VIII. $u_* = l \left(\frac{\partial \bar{u}}{\partial y} \right)$

VIII. and I. combines to

IX. $\frac{u_*}{\kappa y} = \frac{\partial \bar{u}}{\partial y}$

IX. Is then integrated, and can be rearranged to

X. $u^+ = \frac{1}{\kappa} \ln(y^+) + B$

22

Which describes the behavior of u^+ within the log law region, i.e. (25-30)$\leq y^+ \leq$ (100 - 300) According to ref [10].
The log law region is defined to be the region where the profile can be approximated with eq 3.25:

$$u^+ = \frac{1}{\kappa}\ln(y^+) + B$$

Where $\kappa \approx 0.41$ is the Kármán constant, and $B \approx 5.0 - 5.5$ is an integration constant.
The profile from the wall through the log law region of Figure 3.4 is in general universal, with κ varying between 0.40-0.41 and B varying from $5.0 - 5.5$.

3.4   On wall treatment

When flows are computed numerically, the region close to solid surfaces can be problematic.
The region close to solid surfaces usually requires special attention.
In CFD there are two main approaches to treating the flow close to a solid surface.
One approach is to refine the boundary layer grid so that the boundary layer region y=0→δ has a y^+ value of O(1) closest to the wall. The mesh density throughout the region y=0→δ also has to be quite uniform. Hence the approach of resolving the boundary layer often adds tremendously to the computational expense of a simulation. This approach is often referred to as Enhanced Wall Treatment (EWT).

Another way to deal with near wall flows, is to model the near wall regions for $y^+ \leq 30$ (approximately).
In Figure 3.4 the universal dimensionless near wall profile can be seen.
The shared physics of turbulent boundary layers is applied in various ways to bridge the wall boundary conditions to a new set of boundary conditions given for $y^+ \geq 11.5$ in FLUENT ref[10].
This bridging is done by means of Wall Functions (WF), which come in many variants designed to handle various boundary flows.
For the RANS simulations of this thesis, a Non Equilibrium Wall Function (NEWF) was used, due to its acclaimed good performance on flows with stagnation, and high strain ref[10].
For the LES experiments of this thesis a Werner-Wengle Wall Function (WWWF) was used.
The WWWF is the only wall function available for LES simulations in FLUENT, thus being the only option since an EWT approach would render the mesh impossibly large for the available computational resources.

There is also an option in FLUENT to do a so called Detached Eddy Simulation (DES).
Here regions within the flow are defined to be simulated using RANS turbulence models and wall functions, thus using a RANS simulation as a kind of boundary condition.
Based on a wish to investigate the pure LES simulation option in FLUENT, the DES approach was not applied to the simulations of this thesis.
For more detailed information on wall treatment and wall functions in FLUENT ref[10] is recommended.

3.5 Large Eddy Simulation (LES):

In order to understand the concept of LES simulation, the Direct Numerical Simulation approach is good starting point.

In a Direct Numerical Simulation or DNS, all the scales of the turbulence are resolved, and computed.

For a DNS simulations, the Navier Stokes equations(eq 3.1, eq 3.2 (, and sometimes eq 3.3)) are solved directly, without the time averaging done in the RANS approach[eq 3.5-eq 3.7]. The approach demands that the smallest scales of the problem/geometry are resolved.

These scales are referred to as the Kolmogorov micro scales, and are defined as follows:

$$\eta = \left(\frac{v^3}{\varepsilon}\right)^{\frac{1}{4}} [m]$$

eq 3.26

$$\tau = \left(\frac{v}{\varepsilon}\right)^{\frac{1}{2}} [s]$$

eq 3.27

$$v = (v\varepsilon)^{\frac{1}{4}} [m/s]$$

eq 3.28

Where η, τ, and v are the length, time and velocity scales respectively, associated with the smallest eddies that occurs in a given flow.

Figure 3.6 tries to illustrate how energy is contained and transferred from large eddy scales down to eddies of smaller size, until the eddy energy is dissipated as heat when eddies of Kolmogorov magnitude are ***"killed" by the viscosity.***
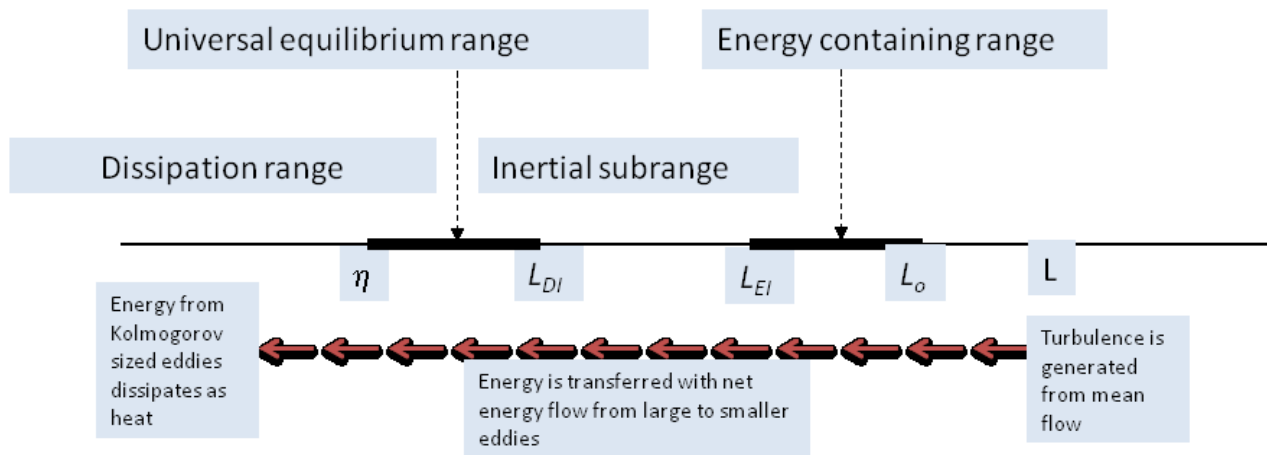
Figure 3.6

Figure 3.6 has been built based on material from ref[2].

In order to reproduce all the physical phenomena of a flow in a simulation, all the eddy sizes from size L down to size η should ideally be resolved and simulated.
This type of simulation is usually referred to as Direct Numerical Simulation or DNS.
Today DNS is mainly carried out on relatively simple geometries for scientific purposes due to the amount of computing power it requires, and the long time it takes for the simulation to give results.
The resulting data from a DNS are also vast, and usually require a lot of post-processing.
The time needed from work is started on a simulation until results are obtained after all post processing is completed, is in the industry often referred to as the "Turnaround time" of a simulation.
DNS can be regarded as the most demanding approach to a simulation with regards to computational expense and turnaround time.
At the other end of this range, the RANS simulation approach is found to be the least "demanding" simulation approach with respect to turnaround time and needed computational resources for a given problem.
This does not mean that all RANS simulations are quick and require little computational resources.
In practise RANS simulations are often applied to problems with complex geometries, high Reynolds numbers and other factors rendering DNS simulations inapplicable .
The features of the simulation cases where a RANS approach is preferable to a DNS approach often bear the characteristics of practical and industrial problems.
For instance the simulation of the flow around an aeroplane is clearly neither a flow which needs nor should or probably even could, be approached by means of a DNS simulation.

Unfortunately, since RANS simulations give time averaged solutions, some of the unsteady physics in a flow may be lost or misrepresented.
An example of this could be the eddy shedding behind a circular cylinder.
For flows where unsteady phenomena are of importance, there is therefore need for a time varying simulation approach.
One way to simulate time varying flows, is to simply use a Unsteady RANS or URANS simulation. The URANS approach can capture the largest eddy structures of a problem, like the Karman vortex street behind a circular cylinder. In fact the URANS approach is a RANS approach to LES, or a VLES (Very Large Eddy Simulation) as mentioned by ref[9].

The picture that forms of the LES approach, is not that of an absolute approach, but rather a balancing between the needed accuracy of a simulation, and available turnaround time and computational resources.

This approach of balancing was also applied for the work done in this thesis.

In the following section, it can be read how the LES approach to a simulation copes with this weighting between modelling and simulating turbulence.

3.5.1   The LES modelling approach:

In the LES approach, the Reynolds averaging of the RANS approach is abandoned.

However the resembling concept of filtering is introduced.

Below follows a brief summary of the filtering of the NS equations and the handling of these equations in LES simulations.

3.5.1.1   Filtering:
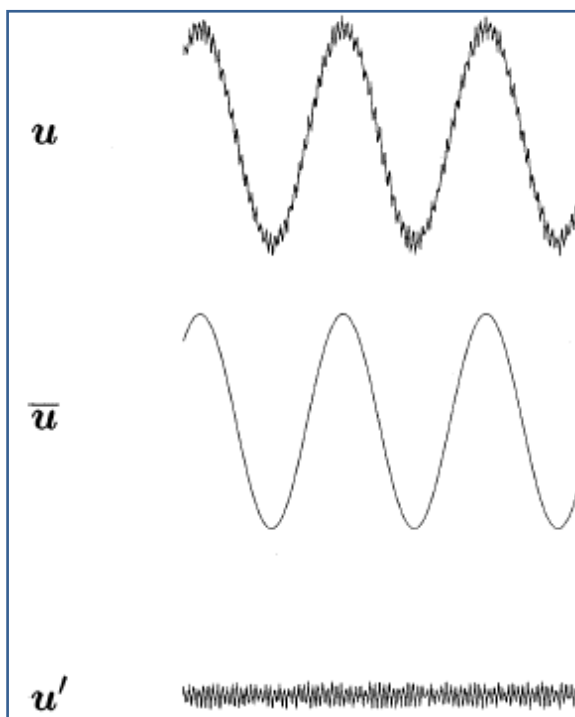
Figure 3.7

Figure 3.7 shows the typical phenomena with turbulent flows, namely that there are several scales of fluctuating velocities present in the total velocity flow field.

The total field velocity is denoted u.

Figure 3.7 has been copied from ref[2].

The total field velocity u is like in the RANS approach separated into two components denoted $\bar{u}$ and u' where

$$u = \bar{u} + u'$$

The difference between the RANS and LES approach lies in the $\bar{u}$ velocity component, which is not a simple time average, but a filtered velocity.

In essence, filtering in the LES context narrows down to sorting the velocity scales you want to be simulated from the velocity scales that are considered small enough to be modelled.

The reason for why smaller turbulence scales are more suitable for modelling, are described closer by ref[9]

There will not be given a detailed account for the filtering process in this thesis, but a brief summary of the main concepts funded on ref[2 & 9] follows below:

The filtering of velocity u, resulting in filtered velocity $\bar{u}$ is exemplified as follows:

$$\bar{u} = \int G(x, x')u_i(x')\,dx'$$

Where G only gets large when x is close to x', and in that way the function G "picks" velocities, dependent on variable x', only when x' is close to a determined value x.

For instance G can take a form like $G(x - x') = \begin{cases} \frac{1}{\Delta} & if\ |x - x'| \le \frac{\Delta}{2} \\ 0 & otherwise \end{cases}$

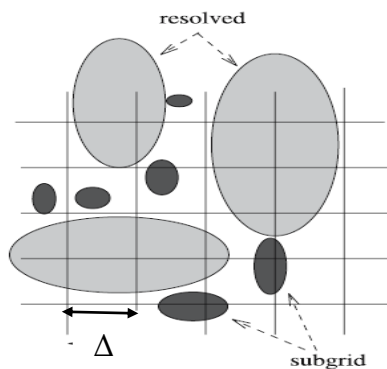Where Δ for instance can be the distance between two grid-points as has been attempted illustrated in Figure 3.8 from ref[2].

Figure 3.8 has been gathered from ref[2]

For more conceptual information on filtering, article ref[9] and ref[10] with relevant listed references are recommended.

In a LES simulation fluctuations related to the $\bar{u}$ term are simulated, whereas fluctuations related to the u' term are modelled.

The modelling is carried out using a Sub Grid Scale model (SGS), in essence similar to the turbulence models of the RANS simulations.

The SGS modelling will be more thoroughly discussed in sections[3.5.1.2, and 3.5.1.3].

How large a portion of the velocity scales should be included in the $\bar{u}$ term

without effecting the results wanted from the simulation, is a balancing that should to be carried out for every simulation case, taking into consideration factors like needed accuracy ,needed resolution of physics, available time and resources, and results from earlier studies of similar cases .

In FLUENT the filtering is done automatically by means of the filter length L_s dependent on the grid resolution ref[10].

3.5.1.2 The filtered Navier Stokes equations.

When the filtering condition $u = \bar{u} + u'$ is applied to the NS equations, and the filtered NS equations can be deduced similarly to how the RANS equations are found.

The main difference in the deduction being that

$$\bar{\bar{u}} \neq \bar{u}$$

I.e. the filtering of a filtered velocity does not necessarily return the same filtered velocity.

The filtered NS equations become:

1)Continuity:

$$\frac{\partial \bar{u}_i}{\partial x_i} = 0$$

2)Impulse:

$$\frac{\partial \bar{u}_i}{\partial t} + \bar{u}_j \frac{\partial \bar{u}_i}{\partial x_j} = -\frac{1}{\rho} \frac{\partial \bar{p}}{\partial x_i} + \frac{\partial}{\partial x_j}\left(\nu \frac{\partial \bar{u}_i}{\partial x_j}\right) + \frac{1}{\rho} \frac{\partial \tau_{ij}}{\partial x_j}$$

Like in the RANS approach, it is the non linear advection term $\left(u_j \frac{\partial u_i}{\partial x_j}\right)$ of eq 3.2 that creates the turbulent stresses.

In the filtered equations the stress tensor takes the form of:

$$\tau_{ij} = \bar{u}_i \bar{u}_j - \overline{u_i u_j}$$

This term is called the Sub Grid Scale Reynolds Stress (SGSRS), and obviously differs from the Reynolds stress term eq 3.8 of the RANS equations, which otherwise in many ways serves as its equivalent.

For instance the SGSRS term that is used to close the filtered NS equations, like the RANS equations are closed with the Reynolds stress term.

The SGSRS term can also be written and explained as ref[9] does:

$$\tau_{ij} = \overline{u_i}\,\overline{u_j} - \overline{u_i u_j} = (\overline{\overline{u_i}\,\overline{u_i}} - \overline{u_i}\,\overline{u_i}) + (\overline{\overline{u_i} u_j'} + \overline{\overline{u_j} u_i'}) + \overline{u_j' u_j'}$$

with labels: Term1, Term2, Term3 above the respective terms.

Where:
- Term1 describes the interaction between two resolved eddy scales producing unresolved turbulence.
- Term2 describes the interaction between resolved and unresolved eddy scales contributing to the unresolved turbulence.
- Term3 describes the interaction between two unresolved eddies and a large scale eddy producing unresolved turbulence.

In terms of energy transport the terms inhere the following characteristics:
- Term1 transfers energy from large to smaller flow structures.
- Term 2 can transfer energy both from small to large, and from large to small eddies. On average the net energy transport goes from larger to smaller structures
- Term3, is able to transfer energy from smaller to larger structures.

Hence it becomes clear that the SGSRS term provides more physics in terms of energy transport than the Reynolds stresses from the RANS equations ref[9].

3.5.1.3 Sub Grid Scale modelling *and implementation*

In order to solve the filtered NS equations (eq 3.31 and eq 3.32) the term τ_{ij} must be closed. This closure is carried out by a Sub Grid Scale Model, analogue to the turbulence modelling of the RANS equations.

In FLUENT the modelling of the τ_{ij} term starts with

$$\tau_{ij} = -2\mu_t \overline{S_{ij}} + \frac{1}{3}\tau_{kk}\delta_{ij}$$

not very unlike the generalized eddy viscosity hypothesis of eq 3.9 of section[3.2.3].

$$\overline{S_{ij}} = \frac{1}{2}\left(\frac{\partial \overline{u_i}}{\partial x_j} + \frac{\partial \overline{u_j}}{\partial x_i}\right)$$

and μ_t here denotes the sub grid turbulent viscosity.
The simulations of this thesis have been made with a dynamic Smagorinsky-Lilly (SL) SGS model.
The standard S-L model models the μ_t term as

$$\mu_t = \rho l_s^2 |\overline{S}|$$

Where

$$|\bar{S}| = \sqrt{2\overline{S_{1j}} \cdot \overline{S_{1j}}}$$

 is the strain rate, and

$$l_s = \min \begin{cases} \kappa y \\ C_s V^{-\frac{1}{s}} \end{cases}$$

is the mixing length of the sub grid scales.

C_s is the Smagorinsky constant,
V is the volume of the grid cell,
κ is the Kármán constant
y is the distance to the nearest wall.
In the Dynamic S-L SGS model the C_s constant is calculated dynamically by active use of information about the resolved scales of motion.

4 The basis for the thesis work:

In section 4, the elements forming the basis for this thesis are explained.
The elements of the basis work, are explained in order to give the reader an overview of the basic tasks, data, and input , on which other elements of the thesis work have been founded.

4.1 Problem definition

In this thesis the SRN IJF geometry of Figure 2.2 is investigated by means of numerical simulations.
The simulations are carried out using the commercially available CFD solver FLUENT 6.3 together with the geometry generation program GAMBIT 2.4.

The final goal of the project work will be to test the LES model of FLUENT on the IJF case, as a means of verifying the models accuracy, and testing how suitable it is for practical simulation purposes, compared to the RANS approach .
By suitability is meant how its overall performance compared to the RANS simulations is with regard to:

- Added/reduced accuracy
- Simulation time consumption
- Computer resource requirements of simulation
- Model suitability as a tool for practical flow investigation.

For more on turbulence, and its modelling through the LES and RANS approach, section[3], ref[7 and 9], together with appendix [B & D] should be consulted.

The simulation work starts off with some steady 2D RANS simulations comparable to earlier reference case work described in sections [4.2.2 and 4.2.3] .
The 2D simulations are later in the project used to make, verify and compare to steady 3D RANS simulations.
 Finally the LES simulation will be carried out, compared, and analyzed in relation to the 2D and 3D RANS simulations, and the reference work of refs[4, 6 and 8].
 After this comparison, an overall conclusion to the thesis work together with an assessment of the LES simulation will be given.
Here the aim will be to make an assessment of the LES approach in FLUENT with regards accuracy and overall suitability to practical applications like explained above.

The analyzing of the various simulations featured in this thesis will be effectuated by means of comparing different plots of flow profiles, and analyzing the simulation data yielded by FLUENT.

In order to save computational resources, it was early in the thesis work agreed that this thesis should focus on the flow behaviour of the IJF problem.
Thereby thermal phenomena were omitted as a focus for the thesis work, resulting in the exclusion of temperature and Nusselt number investigations from further treatment.

It should be noted that thermal simulations were in fact carried out in the starting phases of the thesis. From these, good agreement with the work of refs[4,6&8] was found regarding temperature and Nusselt number profiles.

Further, thermal conditions were(in collaboration with author of ref[8]) found not to influence the pattern of the flow, thus the treatment of thermal phenomena could be left out of the simulations, yet flow characteristics could still be safely be compared to the simulations done with thermal effects. It should be noted that the thermal sources of references[6 and 8] were relatively weak.

4.2   Reference Experiments

Below follows a short description of the experiments which produced the reference data used in this thesis.

The Reference data are of two kinds.

Firstly there are the experimental reference experimental data explained in section[4.2.2], and secondly there are the reference simulations explained in section[4.2.3].

The reference data are used to analyze the yielded simulation results of this thesis in sections[7-0], and can be found in the plots of section[7] labelled as "Experimental" and "SKE".

SKE means Standard k-ε, which is the turbulence model used in reference simulations of ref[8]. All the RANS simulations from this thesis apply the RNG k-ε model.

For more on the SKE and RNG k-ε, Appendix[D] should be consulted.

4.2.1   Reason for choice of reference data.

The works of refs[6 & 8], was considered to feature a sufficiently thorough flow analysis for the requirements of this thesis.

Further Mr Oria Fernández, author of ref[8], was in the period of this thesis work a resident at NTNU, which facilitated easy access to raw data from simulations of refs[6 & 8], since the author of ref[6] Coussirat used to be Mr Oria Fernández' professor.

The two had worked on the IJF problem prior to Mr Oria Fernández' coming to NTNU.

Since the research presented by Coussirat et al., and Mr Oria Fernández in refs[6 & 8] is bench-marked against a set of experimental data, it would seem wise to apply the same dataset as a bench-mark for the simulation results produced in this thesis.

Ref[6] uses experimental data produced from experiments described in paper "Impinging jet studies for turbulence model assessment" ref[4].

Most of the datasets produced in these experiments are readily available on the UMIST database on the net address: http://cfd.mace.manchester.ac.uk/ercoftac ref[5] , where the case is listed as case number 25 "Normally Impinging Jet from a Circular Nozzle".

The purpose of the experiments carried out by ref[4 (or 5)], were according to the authors to produce results idealized for the testing of CFD turbulence models on the SRN IJF problem, which suits the goals of this thesis very well.

Below follows a short description of the experiments of ref [6], and ref[4 (or 5)].

4.2.2 Experimental reference data

The experimental data found in ref[5] were produced with the goal of giving high quality data for the bench-marking of turbulence models.
The yielded results were published in 1992 in "International Journal of Heat and Mass Transfer" in the article of ref[4].
The experiments were made on an impinging jet flow of setup, described below, and more thoroughly discussed in ref[4].

The measurements were made by means of hotwire anemometry, using both single and double wire probes.
The probes were adjusted in parallel to the jet outlet axis by a stepper motor adjustment device, having a minimum step size of just under 2.3μm, thus facilitating fine spatial measurement-resolution in the z direction(Figure 2.2).
However ref[4] reports that measurements taken very close to the impingement-plane were probably affected by heat reflection from the plane I of Figure 2.2.
The impingement-plane itself was devised from a 1275 x 975[mm] printed copper circuit board, set on a plywood base. This base could be lowered or elevated to run tests at desired H/D ratios. It was also possible to adjust the hotwire probe position in parallel to the impingement plane to make measurements at different r/D positions.
The experiments were made for Reynolds numbers of 23000 and 70000, with H/D ratios of 2,3,4,6, and 10. Although according to ref[4] the greatest "emphasis" was put on the H/D=2 case because it would be the case least numerically expensive to simulate due to the smaller domain required by the lower nozzle height.

For quantities being difficult to measure, empirical correlations were used. An example is the calculation of the average nozzle outlet velocity.
The average nozzle exit velocity was calculated from the Centre line velocity by the use of expression:

$$\frac{U_b}{U_{cl}} = 0.811 + 0.038[\log(Re_0) - 4]$$

<div align="right">

eq 4.1

</div>

Reportedly eq 4.1 was found from ref [14].

The paper ref [4] presents a rather comprehensive dataset with regards to mean and turbulent velocity distributions. These distributions are scaled, plotted, compared, and discussed in ref[4].
For a more thorough description and discussion of the experiment, datasets, and results, refs [4 &5] are recommended.

A shortcoming of the data found in ref[5], is that there are only flow data for r/D ratios ≤3, or for what ref [4] describes to be "inside of impingement region" . So even though ref[4] states that measurements were made out to r/D=9, these measurements could unfortunately not be found, not even upon request to UMIST(see ref[4]).

4.2.3 Numerical experiments of Coussirat

The work reported in articles refs[6 & 8] served as a benchmarking case, and an important source of information in the early stages of the project.

The simulations of refs[6 & 8] were all conducted as steady RANS 2D simulations in the CFD program FLUENT.

Ref[6] studies IJF in seven different cases where domains of different D, Re_0 and $\frac{H}{D}$ are analyzed.

On these seven cases, six different turbulence models were tested against the data of ref[4 & 5].

The tested turbulence models in the study were:

- SKE
- Realizable k-ε
- RNG k-ε
- S-A
- V2F
- RSM

Below follows a short description of some important points from ref[6].

For simulations using EWT to give good results for velocity and Nusselt profiles, a maximum near wall $y^+ \approx 3$ was considered necessary.

Further, meshes of resolutions of 5K, 7.5K, 34K and 64K cells were tested in order to determine the mesh sensitivity of the solutions. Ref[6] reports that meshes of 34K and 64K cells were found to give asymptotical, or grid independent, solutions for velocity and Nusselt number profiles.

Since this grid investigation is not described in detail in ref[6], it was nevertheless decided to conduct an independent study of the effects of grid resolution on the simulations results of this thesis.

Based on the results of ref[6], the RNG k-ε model appeared to be one of the best models for overall agreement with the data of ref[4] from ref[5]. Hence the RNG k-ε model was chosen for the RANS simulations of this thesis.

The fact that the RNG k-ε facilitates the application of wall functions, as opposed to the k-ω model which only allows for enhanced wall treatment, was also considered to be one of the models major strengths.

For further information ref[6] should be studied.

4.3 Computer setup

In the following sections [4.3.1-4.5], the computer setup of this thesis is briefly presented . This is done in order to clarify the needed computational resources for repeating and checking the project work, in addition to giving the reader a more comprehensive picture of the conditions and limitations of the simulations.

4.3.1 The hardware setup

Initially all work and simulations were carried out on a HP Compac dc 7700p Convertible with a dual core intel core 2 6400, 2.13 GHz workstation with 1 GB of RAM, running a 32 bit Windows XP operating System .
For the largest LES simulation, there was given access to a HP wx 9300 workstation with dual core AMD opteron 2 GHz CPU and 4GB of RAM, running a 64 bit Windows XP operating system.

4.3.2 The software

The HP wx 9300 workstation was running FLUENT version 6.2, whereas the HP 7700 workstation was running FLUENT version 6.3.
All mesh generation was carried out on the HP 7700 workstation, using the geometry generation program GAMBIT 2.4.

4.3.3 General about boundary meshing

The meshes all had the same boundary layer resolution near the impingement wall.
This was done because it was early on realized that the full LES would have to be conducted using a wall function.
If not so, the near wall resolution of the LES mesh would have to be refined to a level giving y^+ values approaching 1, adding tremendously to the computational expense and probably rendering the LES simulation impossible.
By the use of a wall function, the near wall grid requirement is eased from the level of $y^+ \sim 1$ to $y^+ \sim 25\text{-}100$, i.e. the first grid point has to be within the logarithmic layer described more thoroughly in section[3.3].
Thus the goal of the boundary layer was to place a point within this region.

4.4 Detailed Simulation description

This section gives an overview of the conditions that lay behind the yielded simulation results of this thesis.
The purpose of the section is to clarify the choices that have been made concerning simulations and their setup.
Thus simplifying repeatability, and giving the reader a more comprehensive insight to the simulation process.
In the following sections [4.5 to 4.5.3], the setups of the RANS and LES simulations of this thesis are explained in detail with regards to geometry meshing, and simulation setup.
The latter including information about used boundary conditions, convergence criterions, solver algorithm ,numerical schemes, and turbulence/SGS models.

4.5   Inlet Profiles and Boundary Conditions

As refs[4 & 6] state, the impingement jet **J** of Figure 2.2 needs to be fully developed with respect to velocity and turbulence profiles when it leaves the nozzle in order for simulations and experiments to give results that are comparable.
In order to meet the quality demands for the inlet profiles of the jet, separate simulations for circular pipes were made to deliver fully developed turbulent pipe flows for the simulations of this thesis.
The fully developed turbulent pipe flow profiles were then applied as boundary conditions for the nozzle J of Figure 2.2.
 then for outlet boundary values to be imposed as inlet boundary conditions for **J**.
The advantage with running part of a simulation as a separate module, then to impose values from it as boundary conditions for another simulation, is that computing cost is saved.
For instance the needed amount of memory is reduced, since a smaller mesh is read and iterated on.
FLUENT gives the opportunity to define/ customize boundary profiles so that, for instance, the values at the outlet of a fully developed pipe flow may be set as the inlet boundary conditions for another simulation.
Quantities transferred from the boundary of one simulation to another may involve a number of parameters calculated in separate simulations.
Examples of such quantities may be:

- Velocities (magnitude, components in different coordinate systems, Mach number, etc)
- Turbulent quantities (k, ε, $\overline{u'_i u'_j}$, μ_t, etc)
- Fluid properties (ρ, c_p, μ, etc)
- Temperature
- Various engineering quantities(Pr, Nu, Re, C_f, C_d, etc)

For the RANS simulations of this thesis, pipe outlet values for velocity magnitude, turbulent kinetic energy k, and turbulent dissipation ε, were used to define the inlet conditions for the jet on the IJF geometry.
For LES simulations, FLUENT gives the user the opportunity to synthesize time varying turbulence on boundaries and inside a simulation domain from steady initial conditions.
This may be done using either a Vortex Generation, or a Spectral Synthesizer method.

For the Vortex Generation method, the user needs to define the desired number of vortices on a boundary or domain, as well as profiles or fixed values for k and ε see ref[115] for further information.

For the Spectral Synthesizer method, unsteady turbulence is statistically created from input data like k , ε, and Reynolds stress components $\overline{u'_i u'_j}$ see ref[10] for further information.
It was decided that the Spectral Synthesizer method was the approach best suited for creating unsteady boundary turbulence because the input values required for a good, spectrally synthesized boundary condition were readily available from the pipe flow simulations, whereas the number of vortices on surface needing to be defined for the Vortex method could at best be given a well qualified guess.
Further in the simulation setup process, all boundary conditions were set to match the reported boundary conditions of refs[6 & 8].

4.5.1   The 2D simulations

In the following , there is given background information about the 2D simulations.
This information will help the reader understand the purposes for which the 2D simulations were made, and how they were set up in order to serve these purposes.

4.5.1.1   Purpose of 2D

The goal of the 2D simulations was twofold.
Firstly the 2D simulations were supposed to replicate and verify reference case simulations and experiments done by refs[4 & 8].
In this way the 2D simulations would bridge the reference work of for example ref[4] to the simulations done in this thesis, thus verifying the quality of the simulation results.
Originating from this fundament of verified RANS simulations, there would come detailed data for the flow, usable for creating and analyzing the more complex simulations planned for the later phases of the project.

Secondly, the aim for the 2D simulations were to, in an as quick and easy way as possible, clarify the simulation requirements for the planned simulation studies comprising 3D RANS and LES simulations.
The reason why the 2D simulations were thought to be best suited for clarifying many of the requirements of the 3D simulations, was simply due to the shorter turnaround- time of the 2D simulations.

Quantities yielded by the 2D simulation indicating requirements for the 3D and LES simulations were thus another aim for the 2D simulations.
The sought after measures were identified to be :
- grid resolution
- Best possible geometry meshing and mesh topography
- Verification of turbulence-model
- Boundary condition and boundary value testing.

4.5.1.2 The 2D simulation spec:

Simulation type	2D RANS	
	4K	41K
Mesh type	Quad map	Quad map
Criterion for convergence	10^{-7}	10^{-7}
Solver algorithm	SIMPLE	SIMPLE
Numerical scheme momentum	2. Order upwind	2. Order upwind
Numerical scheme pressure	Standard	Standard
Numerical scheme k & ε	2. Order upwind	2. Order upwind
Turbulence model	RNG k-ε	RNG k-ε
Wall function	non equilibrium	non equilibrium

Table 4.1

Table 4.1 contains tabulated information on the setup for the 2D simulations of this thesis

4.5.1.3 The 2D meshes:

The 2D simulations were made on grids of the same basic geometry shown in Figure 4.2 ,but with different grid resolution with respect to the number of grid cells in each mesh.
As Figure 4.2 shows, the 2D geometry was made for half the geometry in order to save computation time and resources.
Further in order to ensure a fully developed pipe-flow at the jet outlet, a separate pipe profile simulation was run in order to deliver an inlet profile like explained in section[4.5].

For maximum solution quality ref[10] recommends the quad- map meshing scheme, which was used for all the geometries of this thesis.
A bottom-up approach was applied when meshing the geometries, where different boundary edge meshes formed the basis for the different 2D face meshes.
The individual grids that were made, had respective resolutions of :
- 4000 CELLS (hereafter referred to as the 4K mesh),
- 15 000 CELLS *(hereafter referred to as the 15K mesh)*
- 41000CELLS (hereafter referred to as the 41K mesh)
- 71000CELLS *(hereafter referred to as the 71K mesh).*

On examination of simulation results there were found no significant differences between the 4 and 15K meshes, and between the 41 and 71K meshes.
The 15K and 71K meshes were therefore omitted from further analysis, since the interest of the 2D study mainly was to determine the minimum grid requirements for the 3D meshes.

4.5.1.4 Plane vs. Axis symmetry

To gain some initial feeling for the IJF problem, simulations for both axis and plane symmetrical geometries were conducted in the beginning phases of the thesis work. Figure 4.2 and Figure 4.3 show respectively the axis symmetrical and the plane symmetrical velocity magnitude flow fields, where red represents high velocity and blue represents low velocity.

It should be noted that the velocity-value applied to a given colour is scaled to best resolve the presented field, hence the value for a given colour may differ from Figure 4.2 to Figure 4.3. Even so Figure 4.2 and Figure 4.3 give a good qualitative representation of the difference between the axis and plane symmetrical simulations. In short this difference manifests itself mainly in the more rapid decrease of the velocity away from the impingement point for the axis symmetrical flow of Figure 4.2.

 The reason for this more rapid velocity decay comes from the possibility of the axis symmetrical flow to escape in a 360º circle around the impingement zone, whereas the plane symmetrical flow only can move sideways away from the "curtain" of impinging fluid hitting the impingement plane.

In the rest of this thesis, only the axis symmetrical case, often referred to as the Single Round Nozzle IJF (or simply the SRN IJF) case is treated.
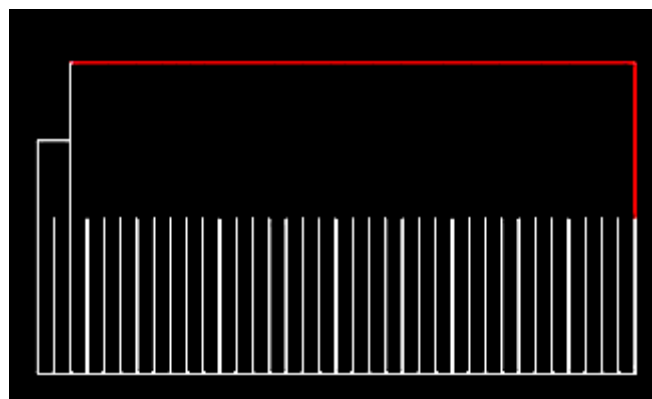
Figure 4.1
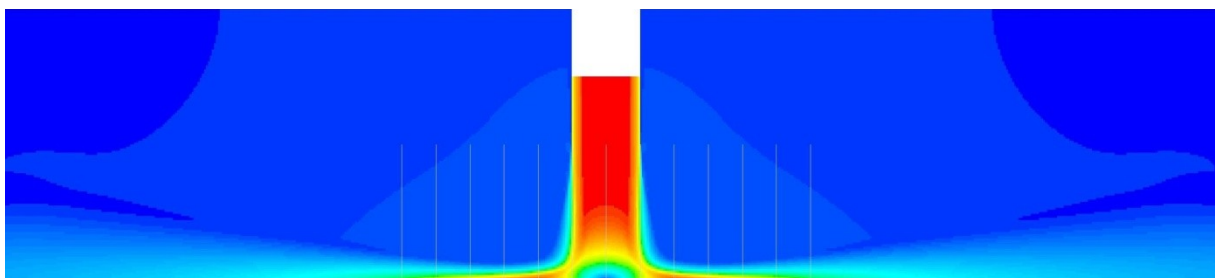
Figure 4.2
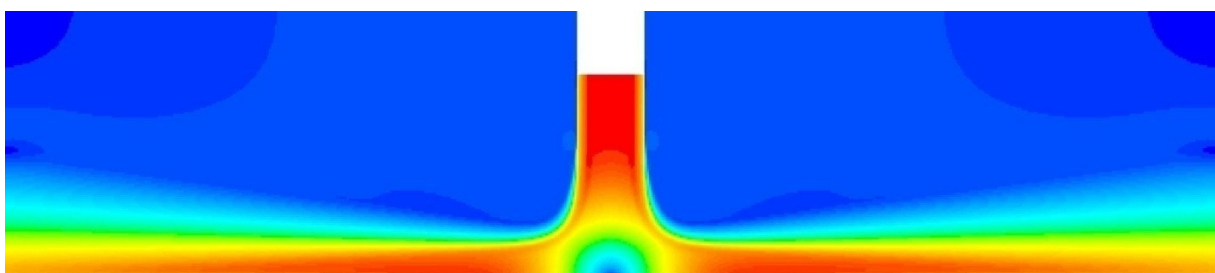
Figure 4.3

4.5.2   The 3D simulations

In the following , there is given background information about the 3D simulations of this thesis (both LES and RANS).
This information will help the reader in understanding the purposes for which the 3D simulations were made, and how they were set up in order to serve to these purposes.
In the following sections, special care is taken to describe the 3D geometry meshing, with focus on the considerations made, and difficulties encountered in the pursuit of high quality meshes.
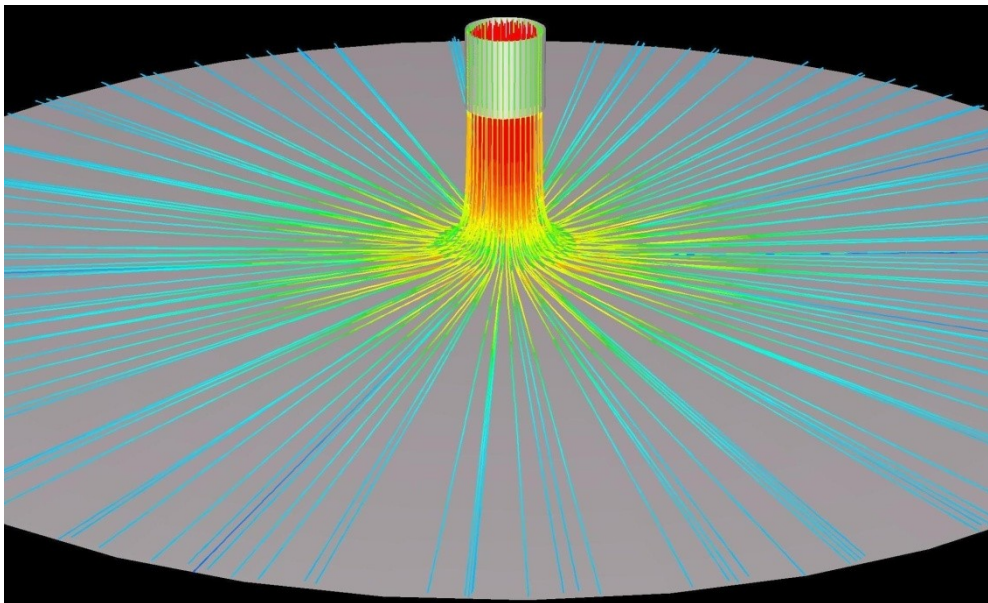
Figure 4.4

Figure 4.4 shows streamlines released from the jet nozzle of the 160K RNG k-ε simulation

4.5.2.1   The purpose of the 3D simulations:

As stated in section[4.1], part the final goal of this project would be to check how LES modelling performed on the SRN IJF problem . In order to do this, a number of 3D simulations (both RANS and LES), would have to be carried out.
At first, three dimensional RANS simulations were conducted in order to check the simulations from the 3D grids against the 2D RANS simulations.
The 3D RANS simulations would later also serve as initial profiles for the LES computations.
The chronology of the simulations, and the information flow between the different stages of the thesis work is more thoroughly explained in section[6.2].

Simulation type	3D RANS		LES (3D)	
	Coarse (160K)	Fine (1300K)	Coarse (160K)	Fine (1300K)
Mesh type	Quad/Hex	Quad/Hex	Quad/Hex	Quad/Hex
Criterion for convergence	10^{-5}	10^{-5}	NA	NA
Number of iterations pr time step	NA	NA	30-300	50
Number of time steps	NA	NA	1000	512
Total number of iterations	-	-	-	25600
Total virtual time simulated	NA	NA	10 sek	5.12 sek
Total physical simulation run-time	<<1h	<<1h	≈1 day	11 days ?
Solver algorithm	SIMPLE	SIMPLE	SIMPLEC	SIMPLEC
Numerical scheme momentum	2.order upwind	2.order upwind	Bounded central difference	Bounded central difference
Numerical scheme pressure	Standard(FLUENT)	Standard(FLUENT)	Standard(FLUENT)	Standard(FLUENT)
Numerical scheme energy	-	-	-	-
Numerical scheme k & ε			NA	NA
Turbulence model	RNG k-ε	RNG k-ε	NA	NA
SGS model	NA	NA	Dynamic Smagorinsky Lilly	Dynamic Smagorinsky Lilly
Wall function	Non equilibrium	Non equilibrium	Werner Wengle	Werner Wengle

Table 4.2

Table 4.2 contains tabulated information on the setup for the 3D simulations of this thesis

4.5.2.2 The 3D meshing strategy:

A goal for the 3D RANS simulations, was to build a fundament of necessary competence and needed material, like computation meshes, boundary conditions, and initial domain solutions, to build up to the full LES simulation.
Thus the strategy for the meshing of the 3D domain, would be aimed at meeting the requirements for a mesh suited for LES.
The FLUENT user manual ref[115] advises on the use of a Quad/Hex meshing.
This means that all cell faces should be shaped like parallelograms, as close to a square shape as possible, and all volume elements should have the form of a Hexahedron, meaning a shape with six faces.

Hexahedral cell
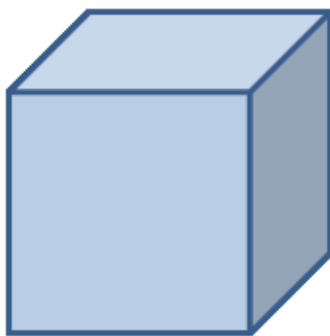
Figure 4.5

Quad cell

Figure 4.6

The implications of using a Quad/Hex meshing scheme brings a number of challenges that will not be mentioned in detail.
However the search for optimal mesh quality and the limitations and difficulties of GAMBIT and FLUENT finally led to a mesh that, looking down onto the impingement plane, would resemble a sliced cake as shown in Figure 4.9 and Figure 4.16.
This mesh layout was chosen because it exploits the inherent axis symmetry of the SRN IJF problem, and gives a regular and controllable cell development in all coordinate directions.
This type of mesh will hereafter be referred to as "the cake mesh" or simply the 3D mesh, since all later 3D meshes were made with the cake type of layout.
However, there were two major problems with the cake mesh

1. Since a Quad-Hex meshing scheme was desired, there would be problems at the centre axis as displayed in Figure 4.7, since the volume elements around the axis would have to be either pentahedral or tetrahedral (having four or five faces).
2. The volume cells would be violently stretched away from the centre region of the domain in the radial direction as can be seen in Figure 4.8.

Centre Axis

Figure 4.7

radial axis
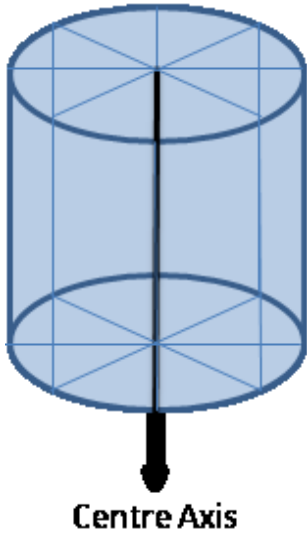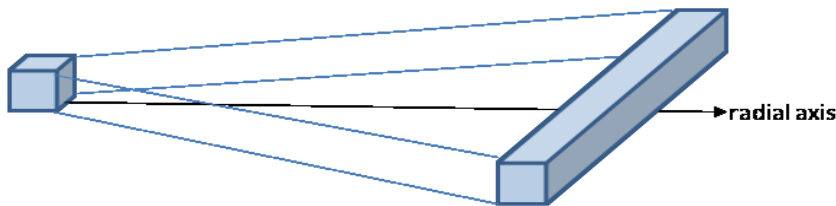
Figure 4.8

For the 3D RANS simulations the cell stretching seen in Figure 4.8 was not thought to be a problem, since the mean flow of the SRN IJF geometry has no inherent θ-wise motions, which can be gathered from Figure 4.4.

The problem with the centre-axis cell geometry, would nevertheless have to be solved in order to make the 3D meshes after the cake slice principle.

Further, the violent cell stretching seen in Figure 4.8 could not be tolerated, or should at least be minimized on the mesh to be used for LES simulations.

It was found that a reasonable approach to solving the issue with the centre axis elements Figure 4.7 would be to segregate the meshing scheme for the region extending from the jet outlet boundary down to the impingement plane, from the rest of the domain.

In short this approach required a separate meshing of the domain regions [$0 \leq r/D \leq 0.5$], and [$0.5 \leq r/D \leq 9$], and then the linking the meshed domains to create one domain.

The domain [$0 \leq r/D \leq 0.5$] would be meshed by the use of the "Quad-Pave" scheme explained further in ref[10], whilst remaining part of the domain [$0.5 \leq r/D \leq 9$] was meshed with a cake geometry by the use of a "Quad-Map Cooper" scheme ref[10].

The result of this segregation can be seen in   Figure 4.11 with the perspective looking down onto the impingement plane.

4.5.2.3 Coarse 160K mesh

As mentioned in section [meshing strategy], the mesh to be used for RANS simulations would not require the grid cells be to very close to cubical in shape (cubical: all sides=equal length and all corners $\approx 90°$), which would be ideal for a mesh to be used for a good quality LES simulation.

A larger allowed stretching of the cells like in Figure 4.9 would allow for fewer "slices" in the cake geometry, meaning fewer cells in the mesh and reduced computational expenses for the simulations.

Since 3D computations inherently require a lot of computational resources in terms of CPU and memory capacity, a mesh of lower quality with inherent lower computational demands, was considered to have practical applications.

Therefore a relatively coarse 3D mesh of 160000 Hexahedral volume cells was made.

Pictures of the grid topography are displayed in Figure 4.9, Figure 4.10, and

Figure 4.11, where Figure 4.9 shows the 160K mesh looking down onto the impingement plane, Figure 4.10 shows two opposing "cake-slices" of one cell width spanning across the meshed volume in the x-direction.

Figure 4.11 shows the region where the segregated meshes merge at r/D=0.5, looking down onto the impingement plane.
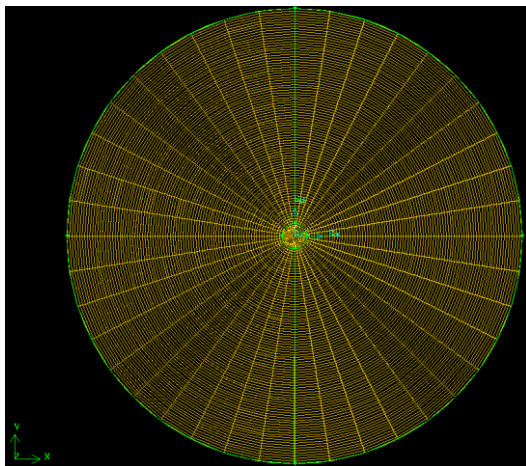
Figure 4.9
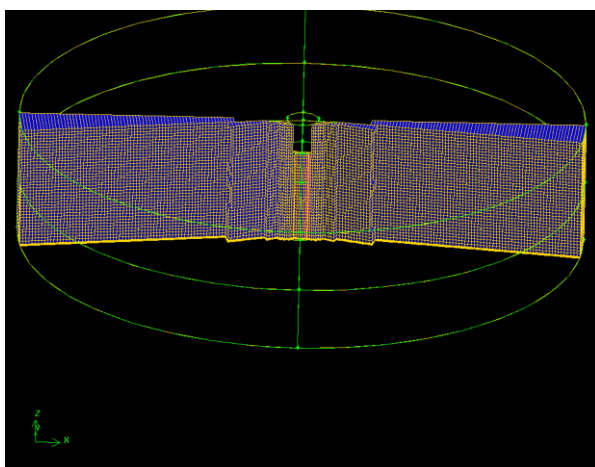
Figure 4.10
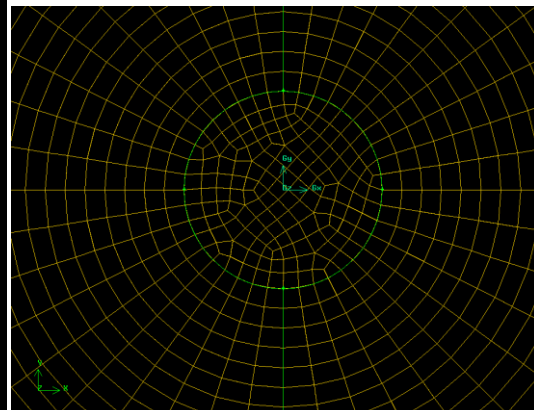
Figure 4.11

4.5.2.4   Fine 1.3M mesh

The final mesh to be made for the simulations of this thesis, was the mesh to be used for the LES simulation of the highest resolution.
Since quite a bit of data and experience had already been gathered by the time this mesh was constructed, its design parameters and design limitations were already quite clear.
From earlier simulation projects it had been found that the hp7700 workstation could manage to iterate on a $1*10^6$ cell mesh with the s-a model, hence 10^6 cells was set as an approximate design limitation for the mesh size.
With the maximum resolution as a "resource frame", the job of making the most of the available resources would determine the finished grid topography and quality.

The initial idea was to use the 160K mesh as a basis, and introduce new radial slices at given r/D positions as shown in Figure 4.13, as opposed to the current 160K mesh topography where all radial lines had to be stretched across the whole domain like in Figure 4.12 WHICH shows an exaggerated representation of the meshing principle behind the geometry of Figure 4.9.
In order to keep the volume cells as even sized as possible throughout the domain.
This strategy however, proved impossible to implement in GAMBIT, so an alternative approach would had to be sought.
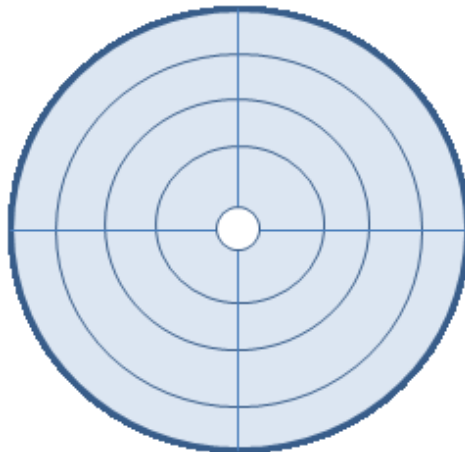
Figure 4.12
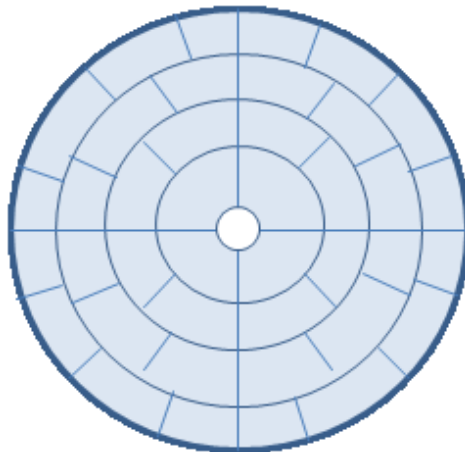
Figure 4.13

Figure 4.12and Figure 4.13 show meshing principles, by looking down onto impingement plane. Both figures violently exaggerate the mesh coarseness. A more realistic picture of the principle of Figure 4.12 is given by Figure 4.9.

In order to minimize the stretching of cells in any one direction for the volume cells, a strategy of evening out the stretching was applied.
Technically this new approach consists of applying a greater number of grid-points around the diameter $r/D=0.5$ (and matching this number at $r/D=9$).
By doing so, a grid cell shape close to $r/D=0.5$ like the one in Figure 4.14 is achieved, and the cell shape of Figure 4.15 is avoided.

The advantage of creating the mesh in this way, lies in making use of the fact that the mesh cells are only stretched in the θ-direction (Figure 4.8) with a "cake slice" topography mesh. The θ-parallel side of the element becomes increasingly large relative to the radial and axial element-sides, which remain constant throughout the grid.
Therefore the cells closest to the centre are made so that the θ side of each element is small relative to the radial and axial sides as Figure 4.14 shows.
As the distance away from the centre increases in the radial direction, the θ side of the element will increase relative to the radial and axial sides, thus the element will become increasingly even sided, before the cell again becomes stretched, but now the θ side is the side larger than the radial and axial sides consult Figure 4.15.
This method brings two major advantages to the grid it produces:
1. It improves cell quality in large areas of the simulation domain.
2. It decreases the maximum skewness of the grid cells.

The concept is tried illustrated in Figure 4.14.
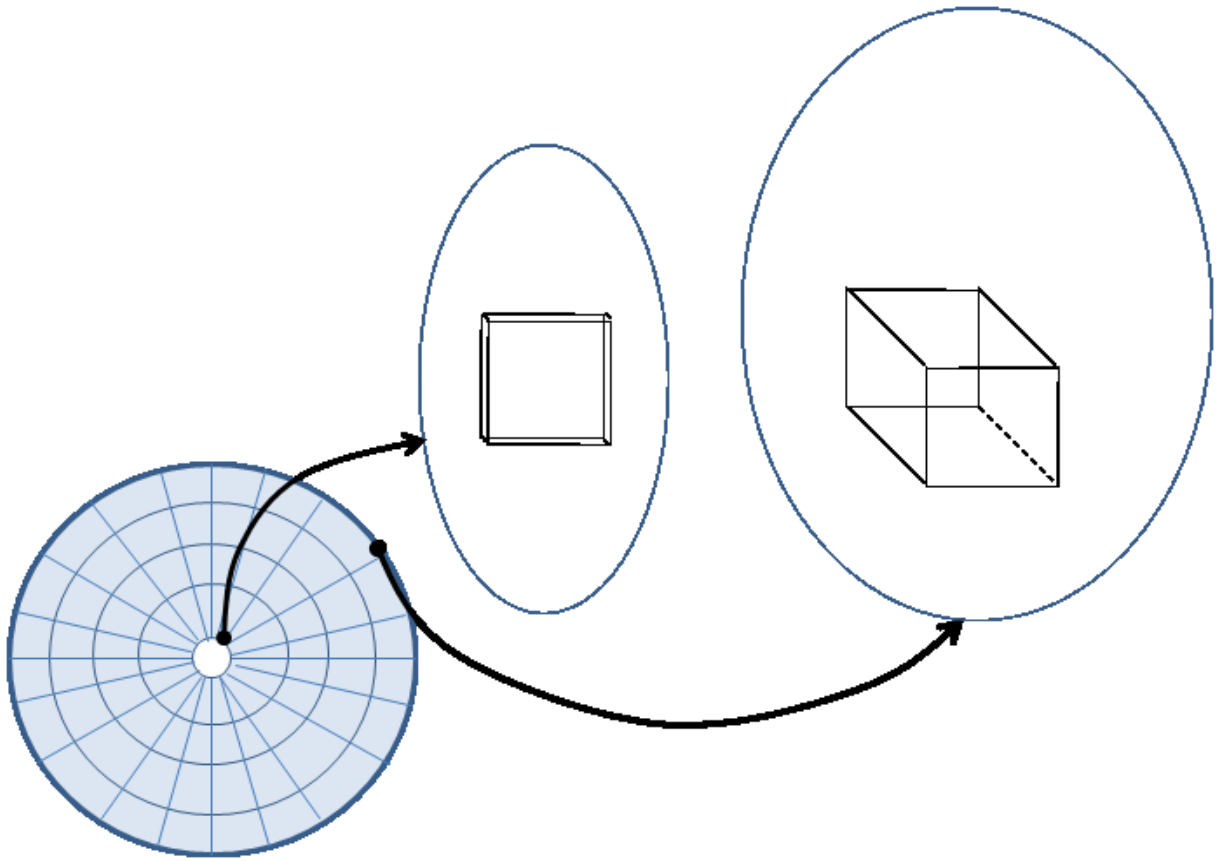
Figure 4.14

47
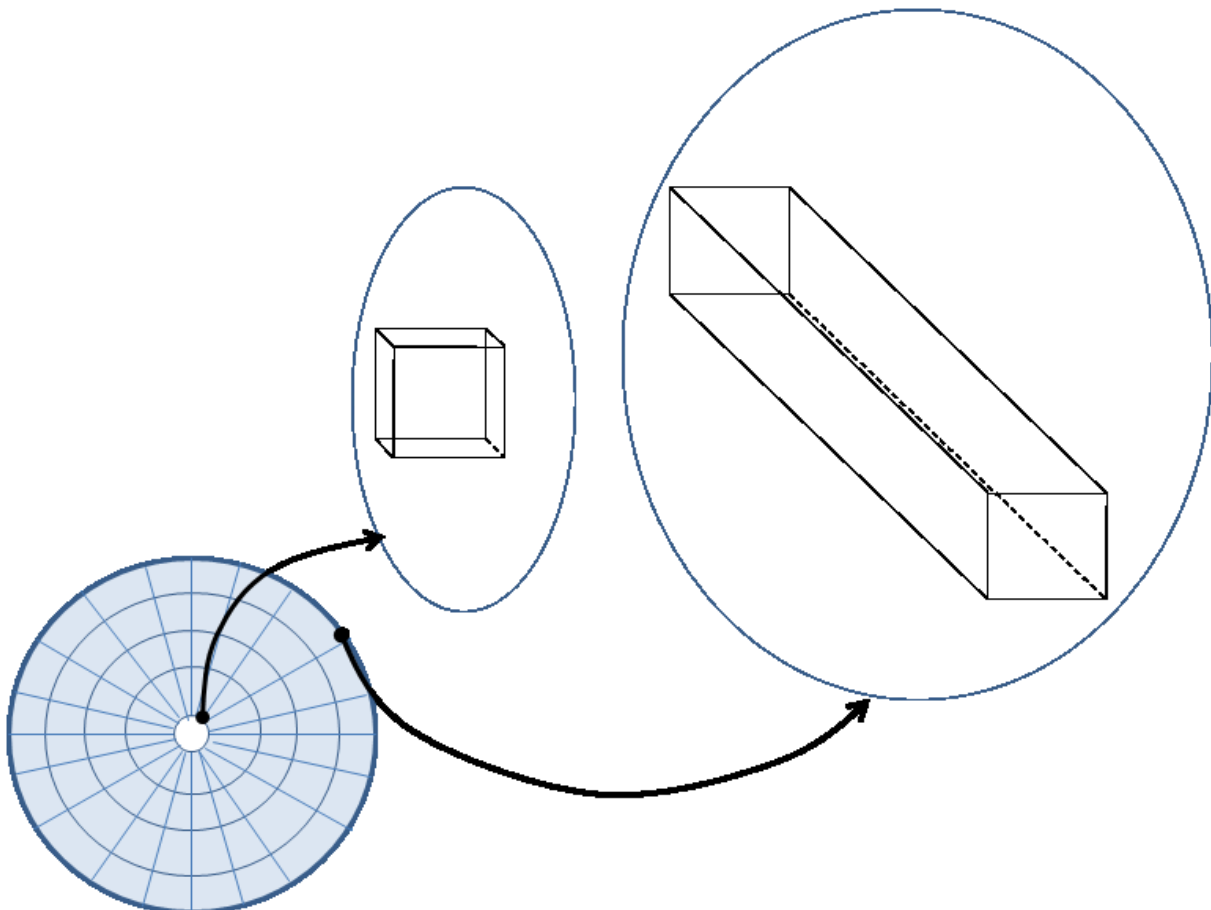
Figure 4.15

If no special attention was paid during a cake strategy meshing, the cells would start out quite even sided, then to become increasingly stretched in the θ direction like Figure 4.15 tries to illustrate.
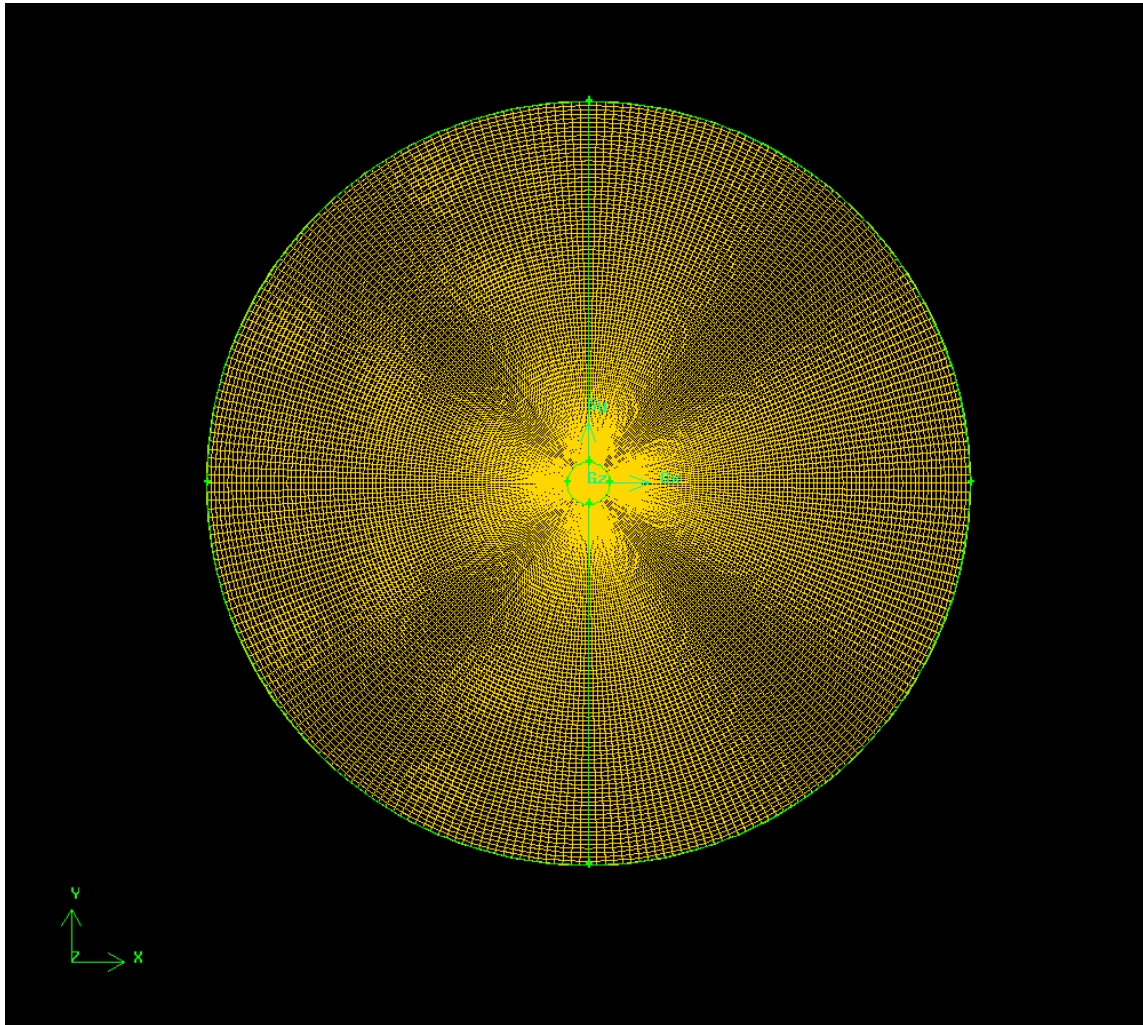
Figure 4.16 displays the finished 1.3M mesh, seen from above looking down onto the impingement plane. The mesh was made by the use of the method explained in section[4.5.2.4], illustrated in Figure 4.14.

4.5.3 Build up to the LES simulation

Before fully committing to the computationally expensive LES simulation on the 1.3M grid, it was thought wise to try to predict some quantities related to its probable time and computer resource consumption.

Data for this study were gathered from available simulations, as well as tasks carried out with the aim of serving other or several different purposes at once like illustrated in the figures of section[6.2].
More in detail, results from the following work was used to elucidate unclear issues around the full LES simulation:

1. The coarser mesh (160K) LES simulation, also carried out to give hands on experience with LES simulations in FLUENT.
2. The steady RANS RNG k-ε 3D 160K and 1.3M simulations, of which the latter was also carried out in order to deliver an "initial profile" to the LES simulation on the 1.3M mesh.

Hence no additional simulations were carried out for the sole purpose of giving data to the pre-LES analysis.

The first issue that had to be clarified was whether it was realistic to expect a full LES simulation to run at all on the 1.3M mesh with the available computing resources of the Compac 7700.
In order to make a qualified assumption on this issue, the steady RANS RNG k-ε simulation on the 1.3M mesh was used as a reference case.
The philosophy being that the SGS model would not prove much more computationally demanding than the RNG k-ε model; hence the need for computing power, and the physical time consumption would not differ greatly between the LES and RANS simulations for each iteration within a time step.
However, the time stepping would obviously add substantially to the overall run-time for the LES 1.3M simulation, compared to the RANS RNG k-ε 1.3M simulation.
This assumption was approximately found to hold true, when the LES simulations were run.

There was then the second issue of how long the LES simulation would take in total physical time on the 1.3M grid, with the available computing resources.
To make a fair estimate of this time, the physical time usage per iteration for the steady RANS RNG k-ε simulation on the 1.3M mesh was considered a likely value to apply to each iteration within a given time step for the 1.3M LES simulation.
From analyzing the coarse LES 160K convergence curves in relation to solution results, the number of iterations pr time step required for sufficient convergence was found to be around 50.
It was found that the iterations exceeding a value of approximately 50, gave small or negligible contributions to solution convergence, and could thus be omitted.
Further it was decided to simulate for a virtual time period equivalent to the 5.12 seconds reported in ref [4] as the sampling time for each data batch.
So with a simulation time step Δt of 0.01 seconds derived or argued for in appendix[A], there would be 512 time steps comprising 50 iterations pr time step.

The expected time pr iteration was estimated to 35-40 seconds, a value found from the iterations of the 1.3M RNG k-ε simulation, being the average time per iteration for this simulation.

T_{tot} = total physical time for LES simulation.
A=number of time steps (512 time stps/total sim)
B=number of iterations pr time step (50 itt/time stp)
C=physical time spent pr iteration in steady RANS simulation (40 seconds/ itt).

$$T_{tot} = A\big(B(C)\big)\ [seconds/total\ sim]$$

eq 4.2

$T_{tot} \approx 512\big(50(40)\big) = 1\ 024\ 000$ secounds $\approx$ 11.9 simulation days
(1 simulation day=24 hours)

Multiplied according to eq 4.2 an estimated physical simulation run time of approximately 12 days was found.
In fact this estimate was found to agree very well with the actual LES simulation run time, when the LES simulation was conducted.

In order for the time averaged values from the LES simulation to be of good quality, the averages would have to be taken from what [10] refers to as a statistically stable solution. According to ref[10] this in short means that the time averages of the solution are constant in time (e.g. mean velocity is not time dependent) for flows that are stationary in the mean..
In order for the solution to reach such a state, the LES simulation was run for 65 hours, from the steady RANS RNG k-ε solution. At that point the solution profiles did not change from time-step to time-step, hence the main LES run was initiated

5 Processing and Analysis of simulation results

The simulation results from FLUENT needed to be analyzed in order to determine the simulation validity and quality.
In order to carry out this analysis, some commonly available quantities from the simulations had to be extracted, and made comparable to the other available simulations and experimental data.
In this section, the extraction, and compiling of "raw" simulation data, is explained

5.1 Data acquisition

In order to facilitate an adequate analysis of the simulations, there was a clear need for a post simulation data-acquisition process. Since the data sets available for post-processing purposes from FLUENT simulations are rather extensive, the post-simulation analysis could easily become complicated by the gathering and treatment of excessive amounts of data.
Hence a plan for how to gather only the needed amount of data, in an as simple way as possible, was needed.

Firstly it had to be decided on what sort of information would likely be the focus for the post-simulation analysis, and the datasets that would be required to produce this information.
Secondly, when the desired data had been identified, there was a need for efficient extraction, combining, and interpretation of the data.

To identify the information to be included in the post-simulation analysis, the studies of refs[4, 6 & 8] were used as references.
 In these reference cases, profiles for velocity magnitude and turbulent quantities were taken at a number of r/D positions.
These types of profiles were considered as a good fundament to build the post-simulation analysis upon.
In order to get these profiles, 27 vertical lines, 2 diameters high and interspaced by 0.25 diameters were created from r/D=0 to r/D=9. The profile lines can be seen in Figure 4.1.
Along these lines selected simulation-values were written to text pad files.
These values comprised quantities like velocity magnitude, grid coordinates, turbulent statistics , and spatial derivatives of respective velocity components.
The gathered data would thus facilitate the production of all the plots presented in section[5.2].
In order to read and perform some manipulation tasks to these data, a Matlab script as can be seen in full in appendix [C] was written.
In addition to the extraction and sorting of the values written directly from FLUENT, algorithms for location and calculation of maximum velocity magnitude Umax, half of maximum velocity magnitude Uh, and vertical positions of Umax and Uh were also implemented in the Matlab code.
Since the initial simulations were made with RANS modelling, using a RNG k-e model, values for turbulent profiles like $\overline{u'u'}$, $\overline{v'v'}$, and $\overline{u'v'}$ were not a part of the post simulation results.

However, following the practise of refs[6 & 8], eq 3.9 from the eddy viscosity hypothesis of section[3.2.3] was used to calculate the turbulent profiles, based on available post simulation values.

5.2   The plots

In later observation and analysis the following plots are used in order to examine the simulation results:
- Velocity Position/Spread
- Velocity Decay
- Mean Velocity Profile
- Fluctuating velocity Profile

Below follows a brief qualitative description of the graphs and plots used to analyze the simulation results in this thesis:

5.2.1   Velocity Position/Spread-rate:

The velocity position plot tracks the position of a velocity magnitude on each of the profile lines in Figure 4.1.
For instance the Max velocity position plot, also referred to as the Max velocity "spread rate plot", displays the z/D position of the maximum velocity at each of the profile lines in Figure 4.1.
The r/D positions of the profiles are appointed to the horizontal axis, whereas the z/D positions of the tracked velocity are appointed to the vertical axis.
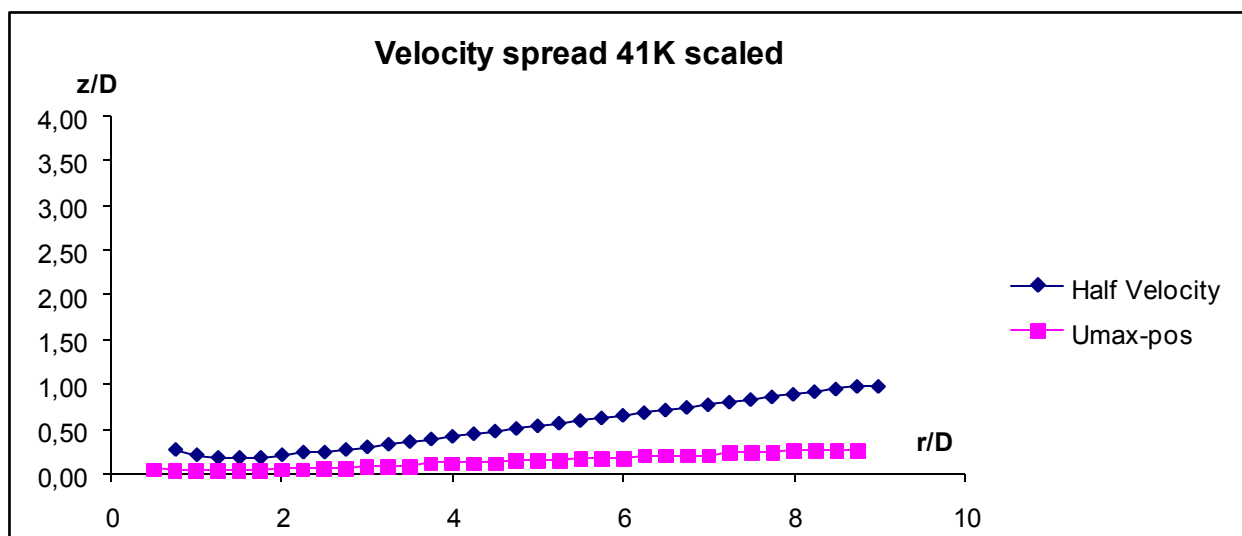
Figure 5.1

5.2.2 Velocity Decay:

The velocity decay plot, displays how a velocity decreases away from the centre axis.
For instance the Max velocity decay plot, displays the value of the maximum velocity for each profile of Figure 4.1, downstream of the centre axis.
The r/D positions of the respective velocities are appointed to the horizontal axis, whereas the velocity magnitudes for each of the r/D positions are correspondingly appointed to the vertical axis.
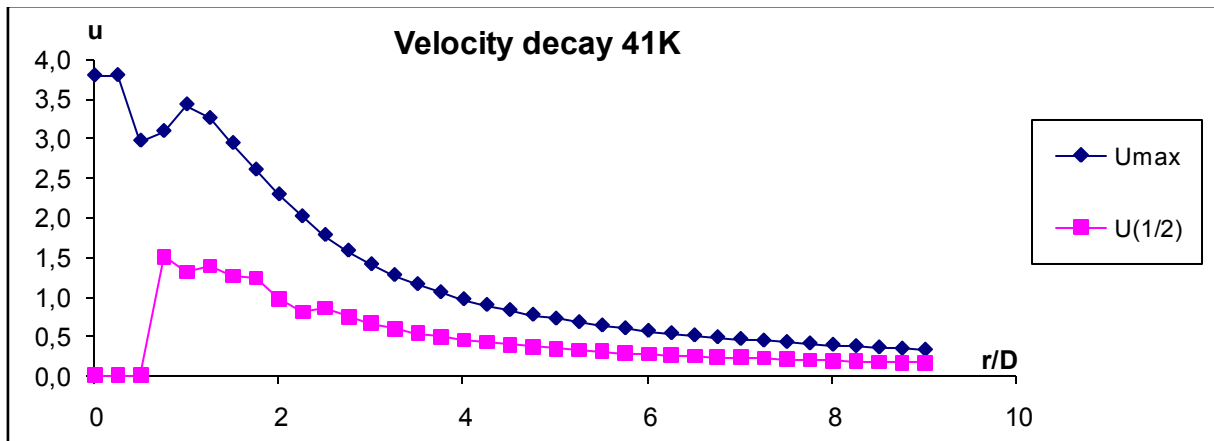
Figure 5.2

5.2.3 Mean Velocity profile

The mean velocity profile plot displays a velocity magnitude profile at fixed r/D positions .
The velocity values for one mean velocity plot, are gathered from one of the z parallel profile lines displayed in Figure 4.1.
Velocity magnitudes are appointed to the horizontal axis, whereas the corresponding positions for each of the velocities are appointed to the vertical axis.
Following the tradition of refs[6 & 8] the vertical axis is plotted in a logarithmic scale.
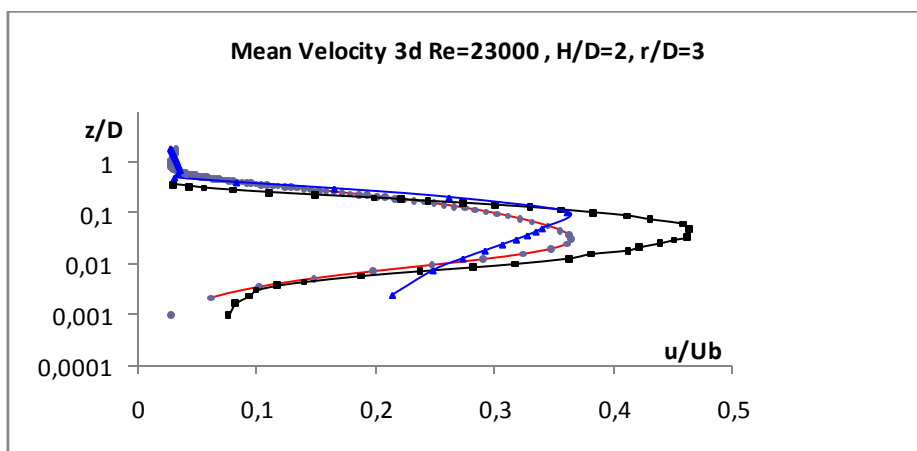
Figure 5.3

5.2.4 Fluctuating Velocity Profiles

The fluctuating velocity profile plots display the profile of the time averaged turbulent fluctuations $\overline{u'_i u'_j}$. The fluctuation values for one plot, are gathered from one profile line as displayed in Figure 4.1.

Fluctuation magnitudes are appointed to the horizontal axis, whereas the corresponding positions for each of the fluctuation values are appointed to the vertical axis.

Following the tradition of ref [6 & 8] the vertical axis is plotted in a logarithmic scale.
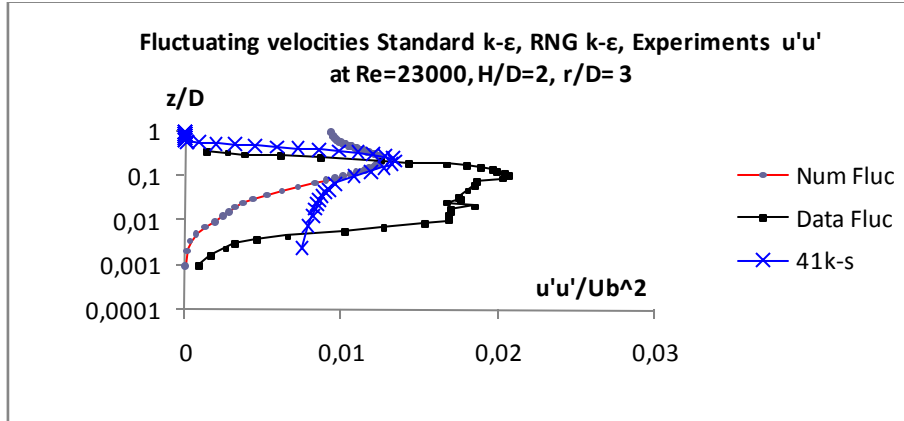
Figure 5.4

6　The comparative study:

In order to acquire and analyze simulation flow field results, and to clarify the uncertain issues related to the oncoming simulations, a study of the completed and in-progress simulations was continuously carried out throughout the course of the project as will be illustrated in Figure 6.1 to Figure 6.9 of section [6.2].
In this study the IJF simulation results are compared to the IJF simulation results of refs[6 & 8], and to the experimental values of ref[4] described more in detail in section[4.2].
The SKE simulation used as reference simulation for this thesis work, originates from ref[8].
The simulation was carried out on a 500 000 cell 2D mesh (hereafter "the 500K mesh").
As this mesh had been analyzed to have y+ value along the wall of O (10^{-3}) for $Re_0 = 23K$ and H/D=2, it was decidedly fine enough. Probably excessively so, but how much yet remained to be verified.

In the article of refs[6 & 8], the flow-field of the IJF is described by means of plotting profiles for normalized velocity magnitude and turbulent fluctuations at different r/D ratios downstream of the outlet centre axis.
In addition ref[4] briefly introduces the spreading rate of the half velocity U_h.
The comparative analysis of this thesis investigates both the individual profiles, and the overall flow picture described by the spread-rate, and decaying plots.

6.1　Method of Approach

The comparative analysis was an ongoing process throughout the whole project. The yielded conclusions and results were often used as means of guiding the further work, for instance with respect to mesh generation and boundary treatment and initial value generation.

A significant issue in the early stages of the comparative study would thus be to determine a sufficient grid resolution for the LES simulations, and to provide good boundary and initial conditions for this simulation.
As ref[9 & 10] states, the importance of mesh quality can be vital for the quality of a LES simulation.
An implication of this was that the grid cells should be kept as close to cubical as possible, resulting in that the 3D mesh resolution was to be dictated by the resolution of the cross section slicing through its centre axis in the radial direction. In other words; a good test for the grid resolution would be to see at what level the numerical results from the 2D simulations started to deteriorate due to the coarseness of the mesh. Then the strategy would be to make a 3D mesh with a coarseness to mach this level in order to keep the computational expenses at a minimum.

6.2   Progress /method visualisations

In this section, [9] block diagrams are presented.

The respective diagrams illustrate the different main operations and processes involved in each of the phases that put together form the whole of the thesis work.
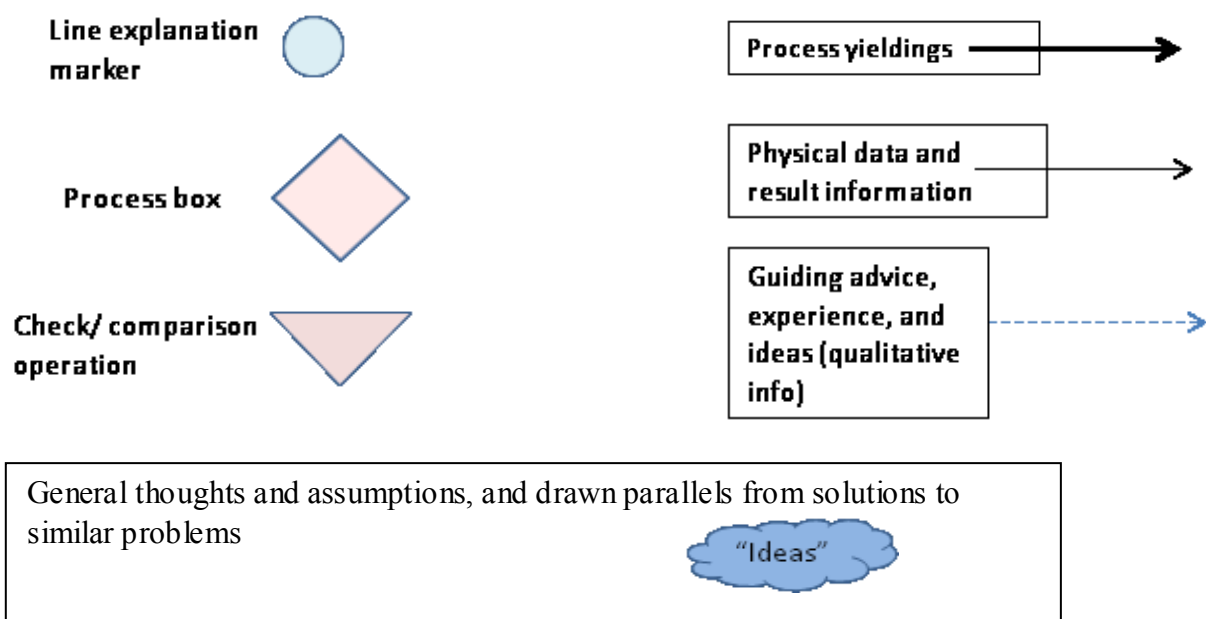
The illustrations also aim to communicate how the results yielded by the individual project phases have been used in order to advance the project work in an as efficient manner as possible.

If studied, illustrations from Figure 6.1 to Figure 6.9 will reveal the benefit of proper task planning, in order to avoid excessive computations and efforts.

To elaborate, the chronology of project tasks, and the systematic usage of simulation data has shortened the necessary number of required simulations and tasks, thus freeing enough for analysis and post processing.

Line marking explanations:
   a. Info from reference simulations regarding turbulence models, mesh coarseness etc.
   b. Simulation data from references
   c. Yielded 2D simulations results
   d. Verified and analyzed 2D RANS simulation results
   e. Info from literature on meshing 3D volumes
   f. Meshing operations and decisions, here the meshes are made from shown input.
   g. Verified 160K 3D RANS simulation results
   h. Verified 1.3M 3D RANS simulation results
   i. Useful info and experience found during coarse-meshed LES simulation to be applied to fine meshed LES simulation.
   j. Verified 1.3M 3D RANS simulation results are paired with useful info and experience found during coarse-meshed LES simulation, before fine meshed LES simulation is initiated.

Figure 6.1
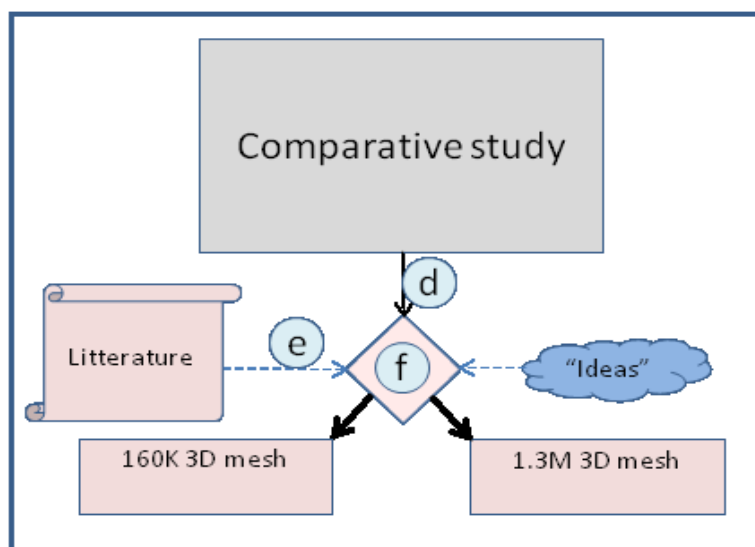
Figure 6.2
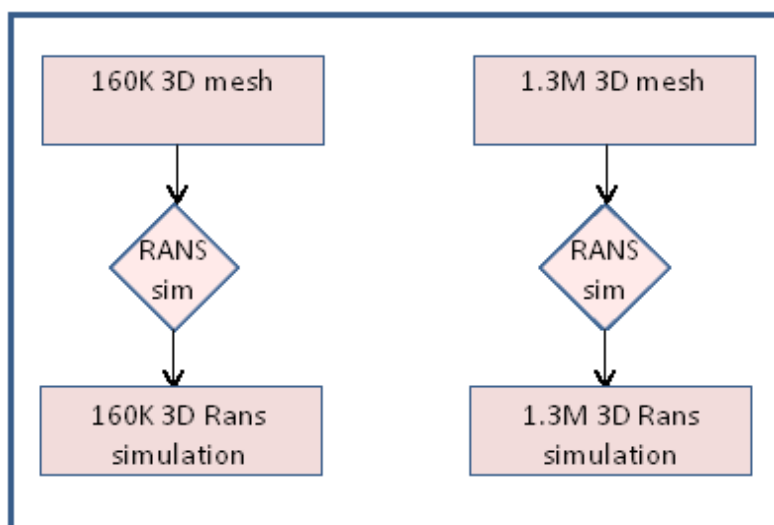
Figure 6.3
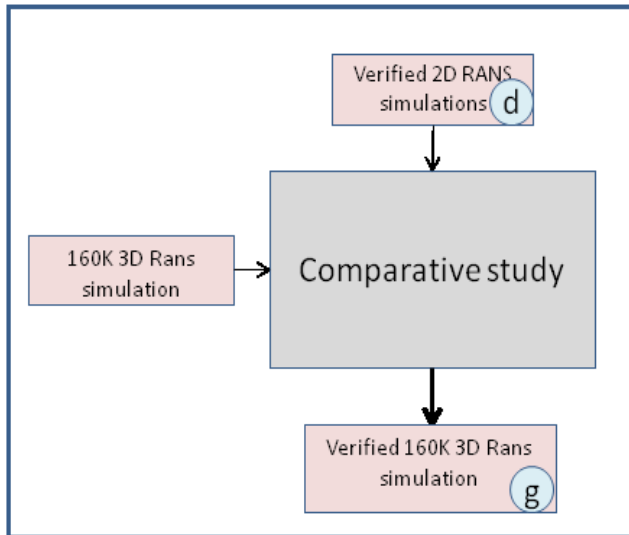
Figure 6.4
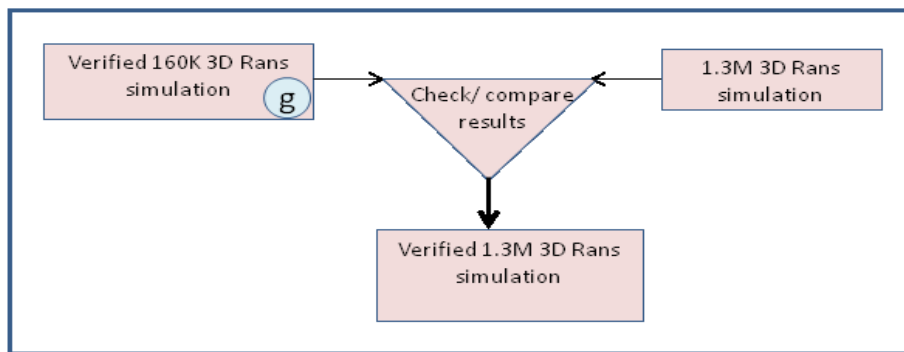
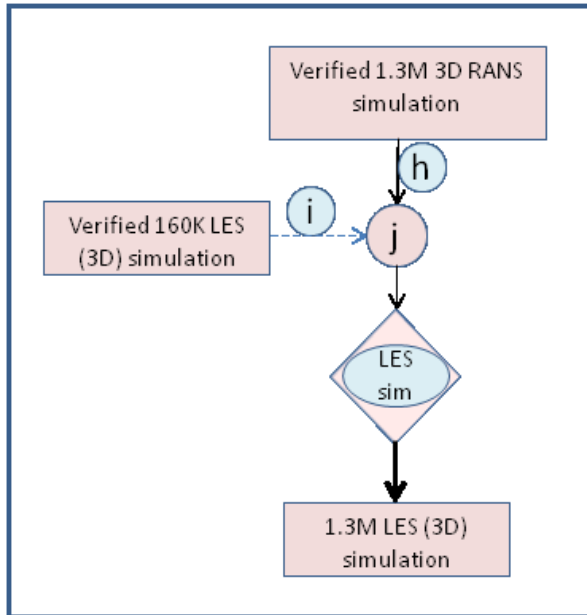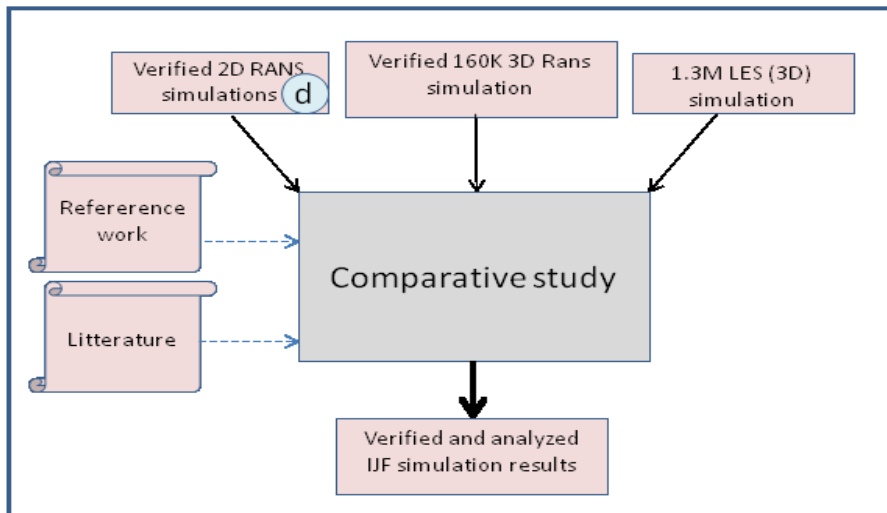**Figure 6.5**
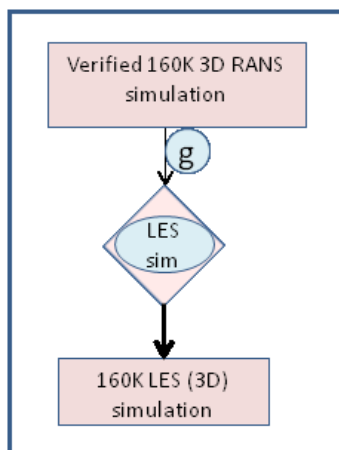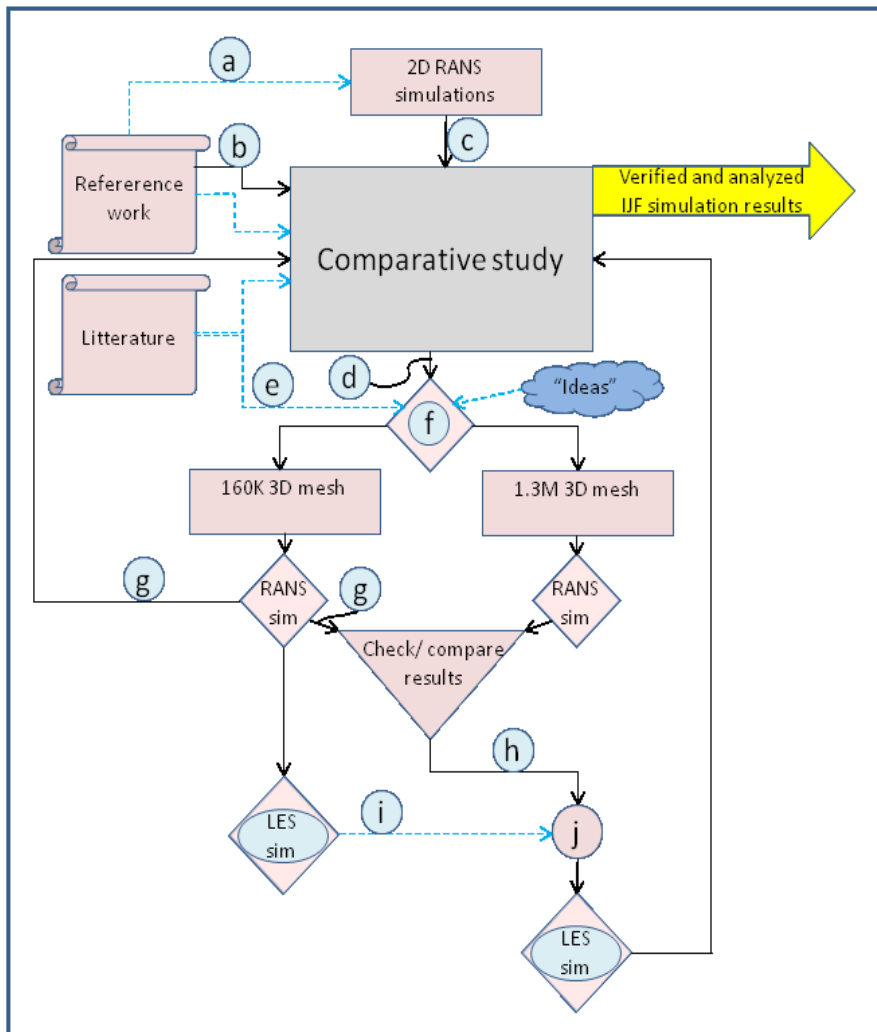

Figure 6.6

Figure 6.7

Figure 6.8

Figure 6.9

Line marking explanation:

a. Info from reference simulations regarding turbulence models, mesh coarseness etc.
b. Simulation data from references
c. Yielded 2D simulations results
d. Verified and analyzed 2D RANS simulation results
e. Info from literature on meshing 3D volumes
f. Meshing operations and decisions, here the meshes are made from shown input.
g. Verified 160K 3D RANS simulation results
h. Verified 1.3M 3D RANS simulation results
i. Useful info and experience found during coarse-meshed LES simulation to be applied to fine meshed LES simulation.
j. Verified 1.3M 3D RANS simulation results are paired with useful info and experience found during coarse-meshed LES simulation, before fine meshed LES simulation is initiated.

7 Comparative analysis:

In the following, the simulation results are analyzed, by means of observation and comparison of the plots described in section 5.2.
The analysis done in section[7], has the goal of yielding a number of observations later to form the basis for the discussion of section[0].

The discussion of this chapter is often funded on the assumption that the experimental data from ref[4] are closer to a physically correct representation of the analyzed quantities like profiles for mean velocity and Reynolds stresses, than those of the simulations.
This assumption may not however be followed uncritically for the high resolution LES simulation, which according to ref[9] sometimes can be suspected of exceeding the level of accuracy obtained by experiments.
In addition to factors like numerically induced discrepancies, the assumed higher credibility of the reference experiments of ref [4] springs from the fact that turbulent RANS simulation profiles are calculated from the eddy viscosity assumption of section[3.2.3], and also because the simulations originating from this project, were made with the use of a wall function.

7.1 Observations about simulations:

In the following sections, observations are made for the simulations, in order to supply input for the discussion of section 0.
Hence observations are made without any particular attempt to analyze or discuss the emerging results, leaving this for section 0 and 9.

The observations are made systematically for each of the individual profile types presented in section 5.2, and respective plots are presented and referred to when observations need to be illustrated.

7.1.1 The mean velocity profiles

When the profiles for mean velocity profiles are analyzed, special weight is put on the following four comparisons to form the basis for the analysis.
1. Comparison between the different grid resolutions.
2. Comparison between simulations at different Re_0 values.
3. Comparison Between simulations from this thesis and simulations from ref [6 & 8] and experiments from ref [4].
4. Comparison of experimental data and RANS (RNG k-ε) simulations to the 1.3M LES simulation.

All profiles of mean velocities from the RNG k-ε RANS simulations of this thesis fit the profiles of the experimental data better than the profiles of the fine 500K SKE simulations of ref [6 & 8] as can be seen from Figure 7.1 and Figure 7.2.
The profile of the 3D RANS simulation is in general seen to yield the lowest velocity values of the simulations of this thesis, whereas the 4K simulation in general yields the highest values.
The 41K simulation profiles place somewhere in between the 3D and the 4K profiles.

The difference between the three RANS profiles of this thesis is however seen to be minute, as can be seen in Figure 7.3 and Figure 7.4.

RANS velocity magnitudes are seen to be spuriously high for z/D< 0.01 approximately Figure 7.1, Figure 7.2, and Figure 7.5.
For the LES simulation this is not the general case.
The LES peak velocity is seen to grow violently in comparison to e.g. experimental data for increasing r/D ratios as Figure 7.8 to Figure 7.10 illustrate.
This growth eventually (at r/D=3) also affects the velocity in the near wall region.
Strictly speaking it is wrong to say that the LES profiles grow. Rather they remain more or less constant with increasing r/D values.
RANS and experimental data profiles on the other hand display a much more rapid decay of velocity for increasing r/D ratios, which will be more thoroughly investigated in section[7.1.3].

Over all it is seen that the RANS RNG k-ε simulations emulate the shape and magnitude of the experimental data velocity profiles rather well although the peak velocity magnitudes are generally somewhat underestimated compared to the experiment profiles see figure[Figure 7.1 & Figure 7.2].
As for the LES velocity profiles of figures[Figure 7.6 to Figure 7.10], very good agreement is seen in the region close to the centre axis (r/D=0→1) between simulation and experimental results.
The further away from the centre axis , the worse the agreement between simulation and experimental results becomes as can be gathered from comparing figures[Figure 7.8 & Figure 7.10].

When comparisons are made between the high and low Reynolds number simulations (Re_0=23K and Re_0=230K comprehensively), it is seen that the normalized Re_0=230K creates a higher peak velocity than the Re_0= 23K simulation.
The Re_0=230K simulation also displays a larger overestimation of the near wall velocity.
This can be seen from Figure 7.5, the velocity overshoot of the Re=230K starts around the same z/D position as the location of the peak in the experiment profile then to deviate ever more as z/D decreases and to the impingement plane is approached.

Vel-mag	Velocity magnitude					
r/D	1.5			3		
Statistic	Normalized velocity magnitude			Normalized velocity magnitude		
Simulation	41K sim	LES	experimental	41K sim	LES	experimental
Normalized peak value	0.86018	1.13268	0.9607	0.411419	0.92311	0.4632
% deviation of sim from exp	10.46320391	17.90153013		11.17897237	99.28972366	

Table 7.1
In Table 7.1 the %-wise deviation of the peak velocity values of the wall-jet are tabulated for the 41K RANS simulation, and the LES simulation at r/D=1.5 & r/D=3
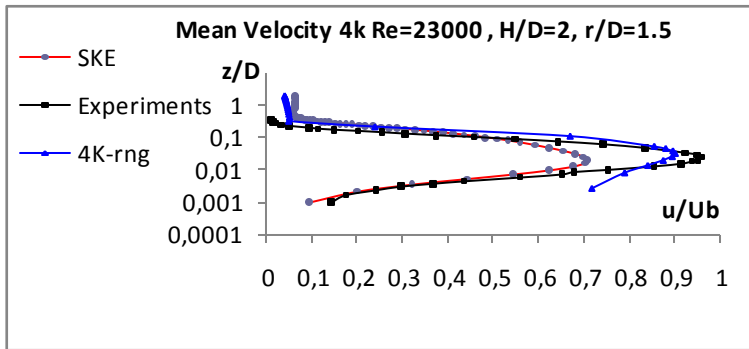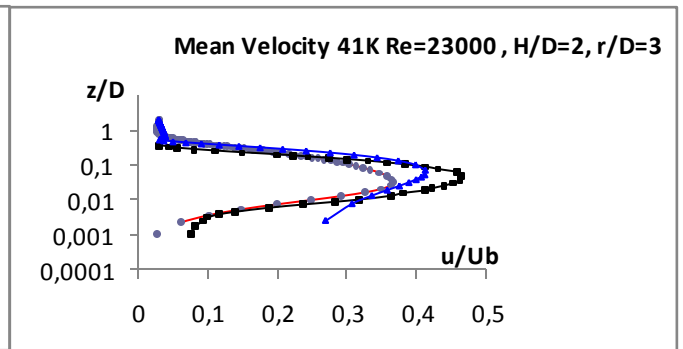
Plots of RANS & Experimental profiles

Figure 7.1

Figure 7.2

Figure 7.1and Figure 7.2:   Comparison of SKE and RNG k-ε simulations to Experimental results
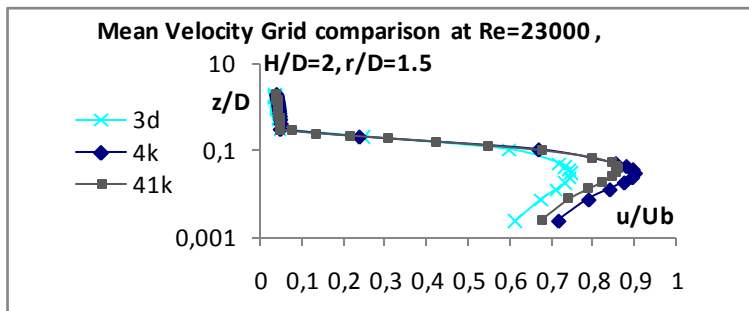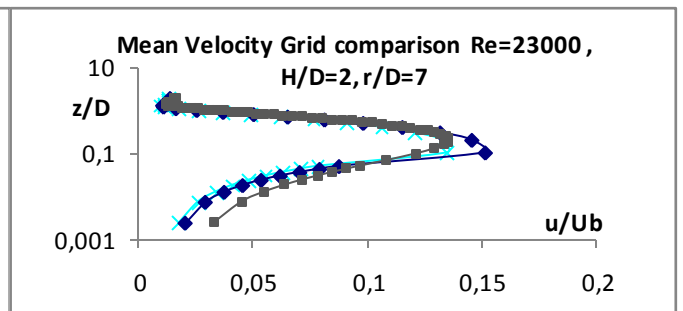

Figure 7.3

Figure 7.4

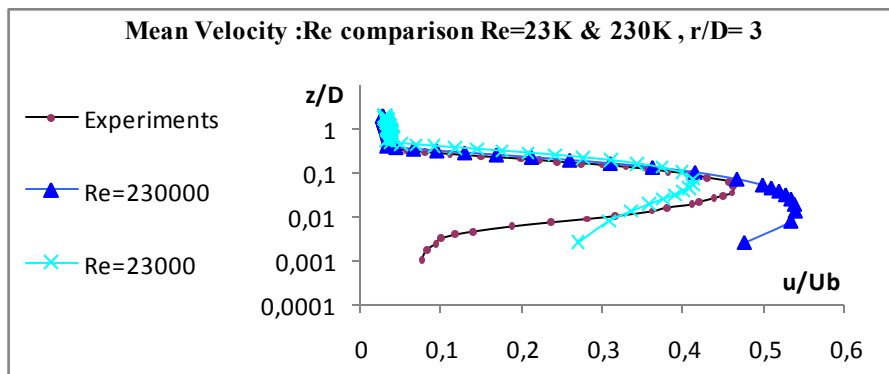Figure 7.3and Figure 7.4:   Comparison of RNG k-ε simulations velocity profiles from grids of different resolutions

Figure 7.5

Figure 7.5: Comparison between $Re_0 = 23K$ and $Re_0 = 230K$ RNG k-ε simulations

Velocity magnitude comparison between: LES simulation, SKE simulation, and Experiments
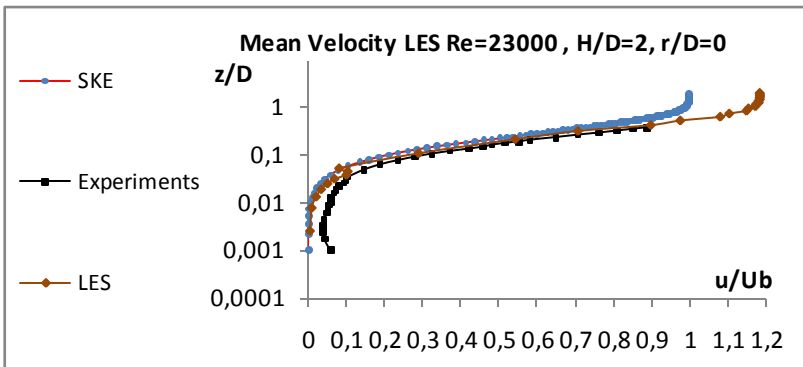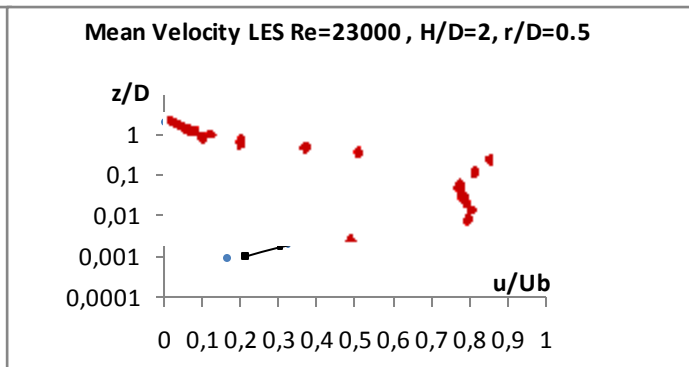
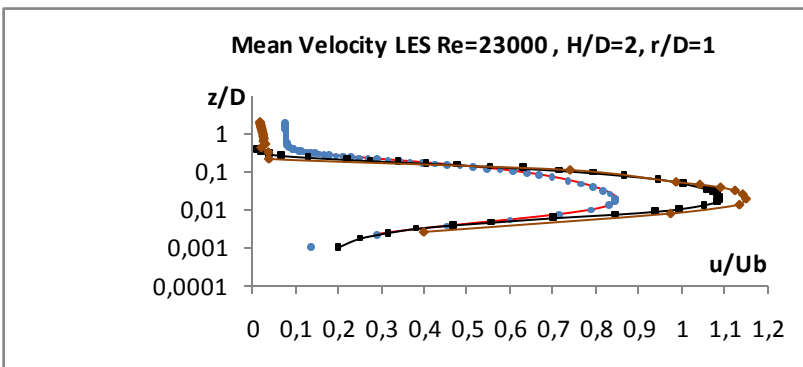**Mean Velocity LES Re=23000 , H/D=2, r/D=0**

- SKE
- Experiments
- LES

Figure 7.6

Mean Velocity LES Re=23000 , H/D=2, r/D=0.5

Figure 7.7

Mean Velocity LES Re=23000 , H/D=2, r/D=1

Figure 7.8

Mean Velocity LES Re=23000 , H/D=2, r/D=1.5

Figure 7.9

Mean Velocity LES Re=23000 , H/D=2, r/D=3

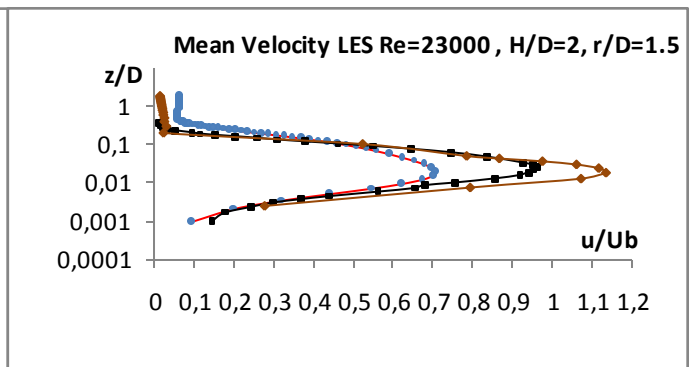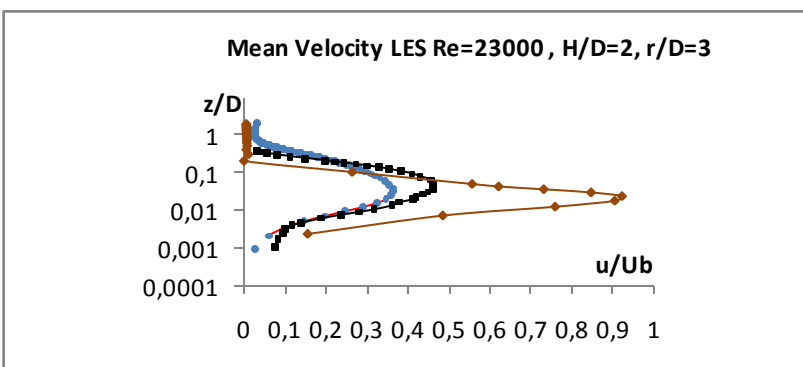**Figure 7.10**

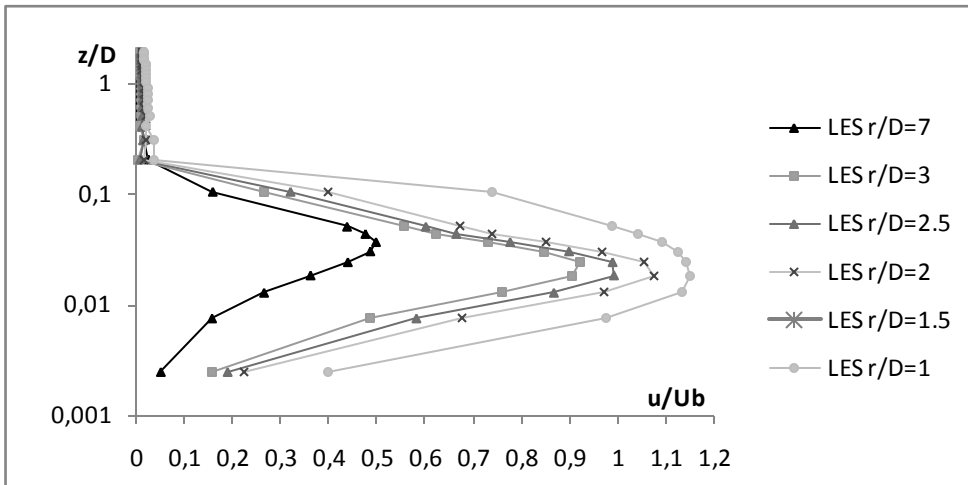Figure 7.6 toFigure 7.10: Comparison between SKE, Experimental, and LES velocity profiles

Figure 7.11: Visualization of LES profile development with increasing r/D

7.1.2 The turbulent statistics $\overline{u'_i u_j}'$:

As can be seen in section [3], the $\overline{u'_i u_j}'$ term in the RANS equations is important in describing turbulence.

The $\overline{u'_i u_j}'$ term is popularly referred to as the Reynolds stresses, then denoted $-\rho \overline{u'_i u'_j}$ having the dimension $\frac{N}{m^2} = Pa$ which makes it a stress tensor.

The $\overline{u'_i u_j}'$ term is used to close the RANS equations in turbulence modelling.

For more on turbulence modelling, see sections[3.2.1 to 3.2.3] or appendix [D].

Like for the mean velocity profiles some comparisons are made to form the fundament for the analysis for the turbulence profiles:
1. Comparison between the different grid resolutions.
2. Comparison between simulations at different Re_0 values.
3. Comparison Between simulations from this thesis and simulations from ref[6 & 8] and experiments from ref[4].
4. Comparison of experimental data and RANS simulations to the 1.3M LES simulation.

The values for the $\overline{u'_i u_j}'$ term presented in graphs, and analyzed in this section, have been normalized in the same way as in ref[Roger& Couss+ experiments] by U_b^2 $(= 3.45^2)$, introducing the dimensionless $\frac{\overline{u'_i u'_j}}{U_b^2}$ term to express the $\overline{u'_i u_j}'$ term. Hence it is important to bear in mind that the discussed profiles for $\overline{u'_i u_j}'$ are scaled.

However, for brevity the $\frac{\overline{u'_i u'_j}}{U_b^2}$ term will hereafter only be referred to as $\overline{u'_i u_j}'$ implicitly meaning $\frac{\overline{u'_i u'_j}}{U_b^2}$.

7.1.2.1 The $\overline{u'u'}$ observations:

As figures[Figure 7.12 & Figure 7.13] exemplify, the values of the $\overline{u'u'}$ stresses are generally under predicted by the RANS simulations compared to the experimental values of ref[5]. This under prediction is especially clear for $0.005 \leq z/D \leq 0.025$.

It is also seen that this under-prediction increases downstream of the impingement point.

Further, when z/D increases towards O(1), the SKE simulation of ref[8] on the 500K mesh spuriously over estimates the turbulent $\overline{u'u'}$ stresses, seen in figures[Figure 7.12 & Figure 7.13].

The RNG k-ε and experimental values are much better matched in this region as profiles practically overlap.

Neither the SKE 500K simulation or the RNG k-ε simulation manage to give an accurate prediction of the peak $\overline{u'u'}$ value for any of the profiles analyzed(again exemplified in Figure 7.13).

Near the impingement point, the SKE simulation is seen to perform slightly better than the RNG k-ε at predicting the maximum $\overline{u'u'}$ value (Figure 7.12). However, the RNG k-ε simulation performs slightly better than the SKE simulation away from the impingement point Figure 7.13.

The percent-wise deviation of the peak $\overline{u'u'}$ value. Predictions of the RANS RNG k-ε and LES simulations are presented in Table 7.2.

For the $\overline{u'u'}$ normal stresses of the LES simulation, good agreement is seen between the experimental and LES profiles close to the impingement region (r/D≤ 1) fig[Figure 7.16 & Figure 7.17] .

After r/D=1, the LES simulation $\overline{u'u'}$ magnitude drops off relative to the experimental data until r/D=2 exemplified in figs[Figure 7.18 &Figure 7.19].

From r/D=2.5-3, the LES $\overline{u'u'}$ profiles display a growing peak value, eventually far exceeding the peak values of the experimental data and the RANS simulations exemplified in Figure 7.20.

It is however, seen that the LES simulation succeeds in predicting / emulating the general shapes of the $\overline{u'u'}$ profiles.

For instance both the experimental data the LES simulation yield profiles for r/D= 1.5 and r/D= 2 displaying respectively a two peaked profile, and a profile with a peak followed by a small second plateau figs [Figure 7.18 Figure 7.19].

Like for the velocity magnitude profiles, the height of the LES $\overline{u'u'}$ profiles in the z-direction is observed to be lower than the height of the $\overline{u'u'}$ profiles from the experimental data and the RANS simulations figs[Figure 7.16Figure 7.20].

At r/D=7 the 4K and 3D RANS simulations yield some suspicious looking profiles displayed in Figure 7.15. Further, at this point the profiles for 4K and 3D RANS simulation are essentially identical (Figure 7.15).

It is suspected that the profile of the 41K simulation of Figure 7.15 might display a more physically correct profile shape. Unfortunately neither ref[4, 6, or 8] deliver data further than r/D=3 downstream of impingement point.

u'u'	u'u' turbulence					
r/D	1.5			3		
Statistic	u'u' magnitude			u'u' magnitude		
Simulation	41K sim	LES	experimental	41K sim	LES	experimental
Normalized peak value	0.03029	0.018234	0.03833	0.01325	0.038536	0.02065
% deviation of sim from exp	20.97573702	52.42890686		35.83535109	86.61501211	

Table 7.2

In Table 7.2 the %-wise deviation of the turbulent u'u' fluctuations are tabulated for the 41K RANS simulation, and the LES simulation at r/D=1.5 & r/D=3
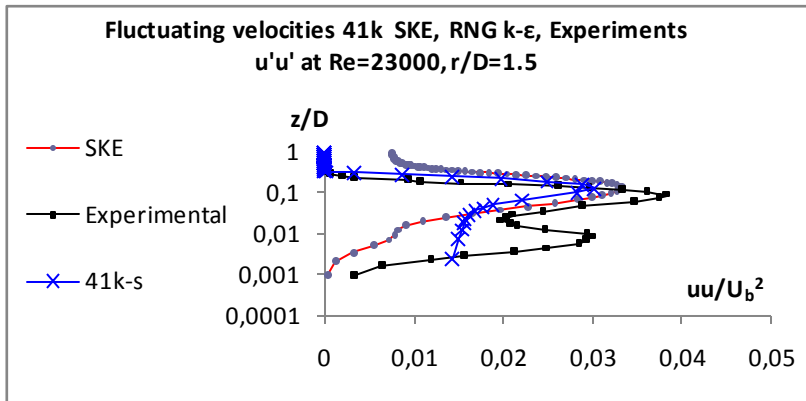
Fluctuating velocities 41k SKE, RNG k-ε, Experiments u'u' at Re=23000, r/D=1.5

z/D

SKE

Experimental

41k-s

uu/U_b²

Fluctuating velocities 41k SKE, RNG k-ε, Experiments u'u' at Re=23000, r/D=3

z/D

uu/U_b²

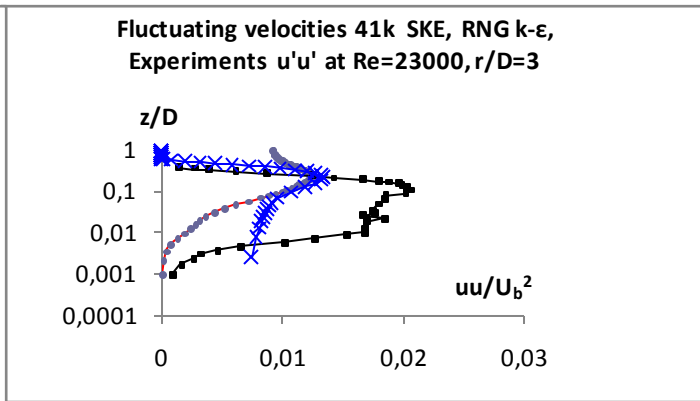**Figure 7.12**   **Figure 7.13**

Figure 7.12 and Figure 7.13: Comparison between u'u' turbulence profiles from Experimental values, against SKE 500K, and RNG K-ε 41K simulations.
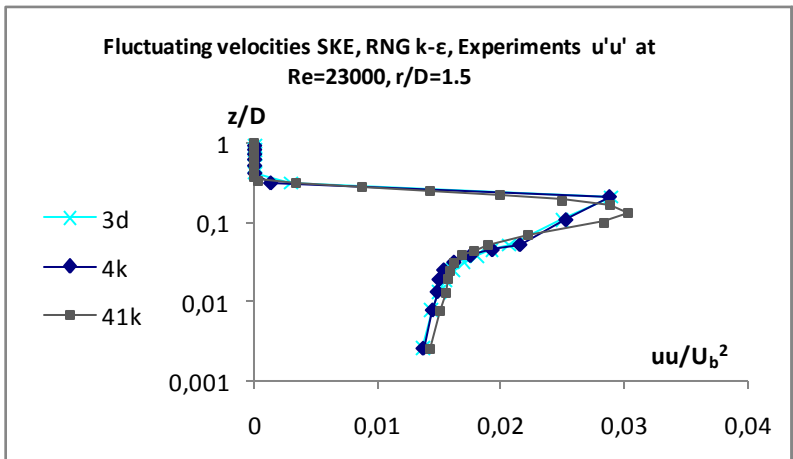
Fluctuating velocities SKE, RNG k-ε, Experiments u'u' at Re=23000, r/D=1.5

z/D

3d

4k

41k

uu/U_b²

Fluctuating velocities RNG k-ε u'u' at Re=23000, r/D=7

z/D

uu/U_b²

Figure 7.14   **Figure 7.15**
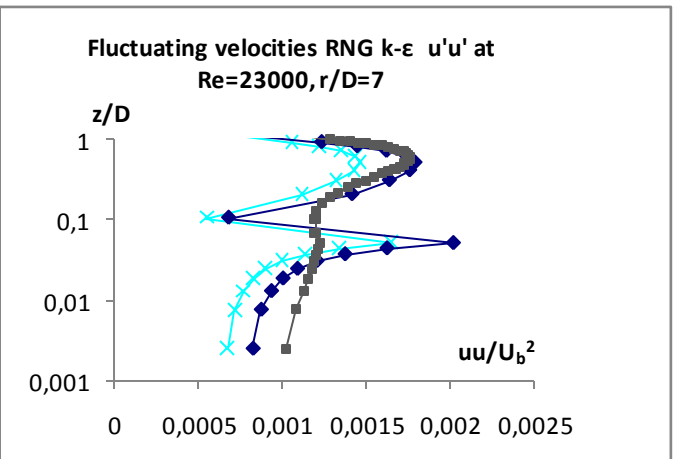
Figure 7.14 and Figure 7.15: Comparison between u'u' turbulence profiles from RNG K-ε simulations in 3D, 4K, and 41K meshes.
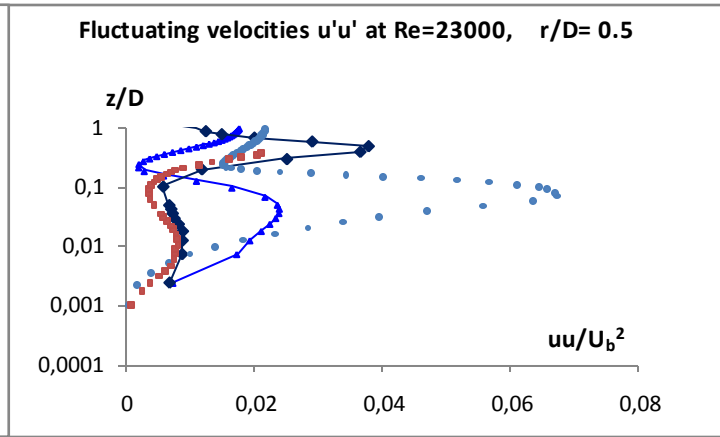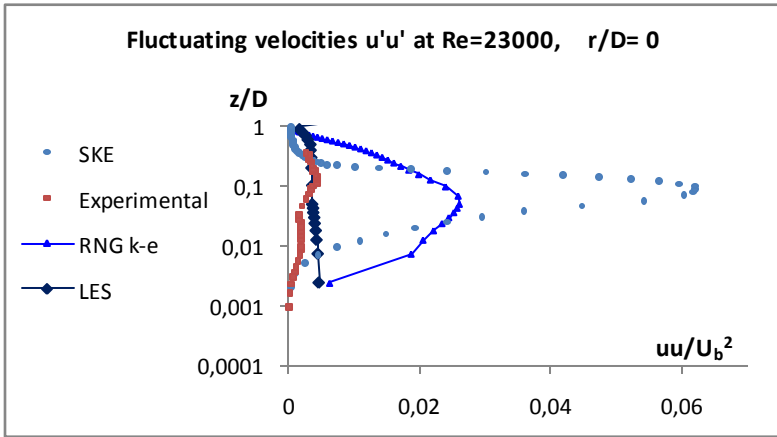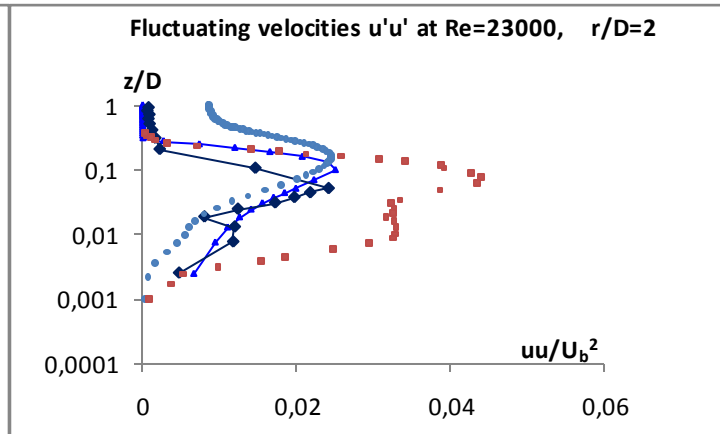
70

Figure 7.16
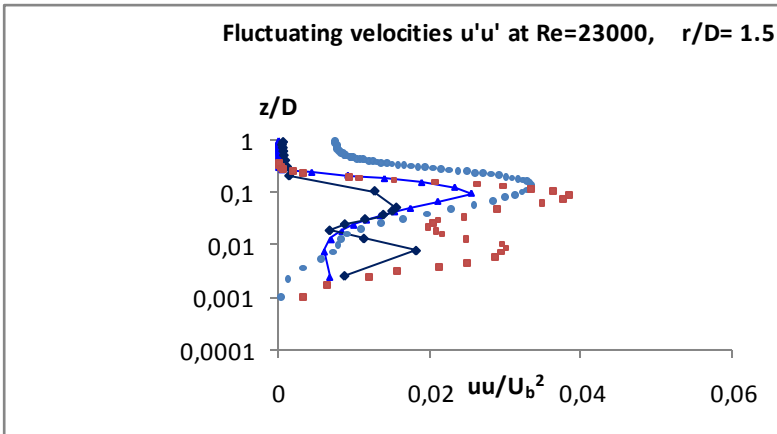

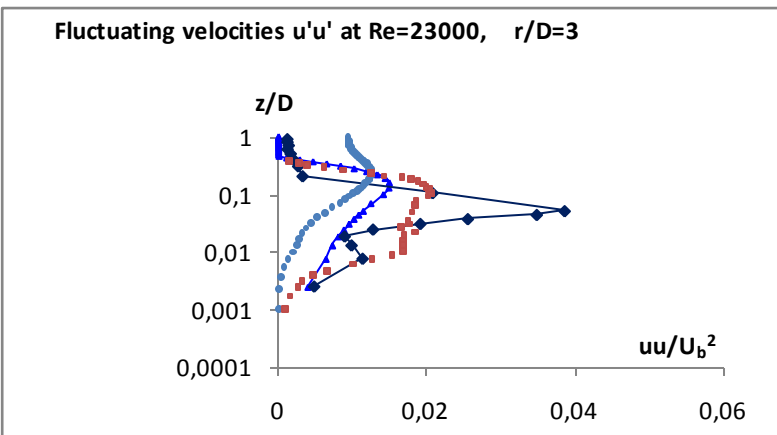
Figure 7.17

Figure 7.18

Figure 7.19

Figure 7.20

Figure 7.16 to Figure 7.20: Comparison between u'u' turbulence profiles from SKE, RNG K-ε, and LES simulations to Experimental profiles.

71

7.1.2.2 The $\overline{v'v'}$ observations:

When it comes to experimental data for $\overline{v'v'}$ profiles, such data can unfortunately only be found for r/D=0.5, 1, 2.5, and 3 in the work of refs[4, 6, and 8].

It is seen that all RANS simulations of all grid resolutions, and both Re_0=23K and Re_0=230K severely over predict the peak values of the $\overline{v'v'}$ profiles compared to experiments of ref[4]. Figure 7.25 shows the $\overline{v'v'}$ profiles for the RNG k-ε and the SKE simulations together with the $\overline{v'v'}$ profile from ref[1144] at r/D=3.

Like in the $\overline{u'u'}$ analysis, the profiles for $\overline{v'v'}$ at r/D=7 show the same suspicious looking profile shapes in conjunction with the simulations grid resolution as the $\overline{u'u'}$ profiles. Indeed when compared, the RANS profiles for $\overline{u'u'}$ and $\overline{v'v'}$ stresses are found to be identical (Figure 7.21)
The unphysical isotropic normal turbulent stress is caused by the k-ε turbulence model, and is one of its well known flaws (ref[7]).

When the LES $\overline{v'v'}$ profiles are analyzed, the following observations are made:
For r/D=0.5 all LES profile values are higher than experimental values.
However, the profile shape /curvature is seen to approximate the shape /curvature of the experimental data well, or at least far better than the RANS simulations figs[Figure 7.22 to Figure 7.25].
It is also noticed that at r/D=0.5, the best agreement between data from experiments and LES simulations is seen close to the wall Figure 7.22.
For r/D=1, 2.5, and 3 seen in figs[Figure 7.23 to Figure 7.25], a peak value develops in the profiles from the experimental $\overline{v'v'}$ data. This peak is approximately located at z/D≈0.1.
It is observed that the LES $\overline{v'v'}$ profiles are slow in picking up on this trend, i.e. the LES peak $\overline{v'v'}$ values are lower, and grow slower than the peak $\overline{v'v'}$ values of the experimental data figs[Figure 7.23 to Figure 7.25].
It may however be observed that the LES simulations approximate the experimental $\overline{v'v'}$ profiles far better than any of the RANS simulations.
This fact is backed by the results presented in Table 7.3, that shows the percent-wise deviation of the simulated peak $\overline{v'v'}$ stress at r/D=3 compared to experimental values

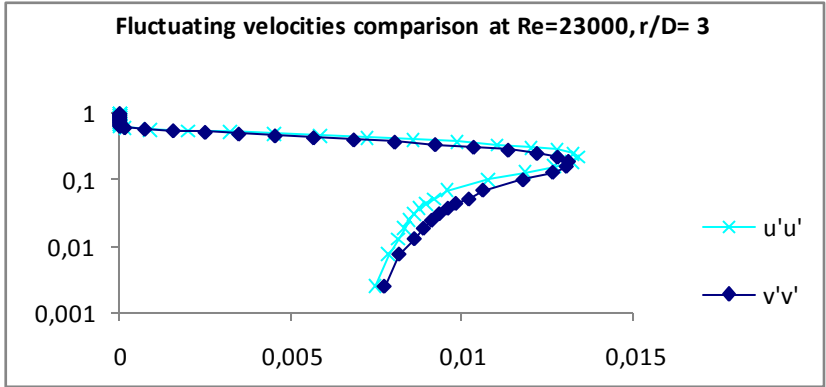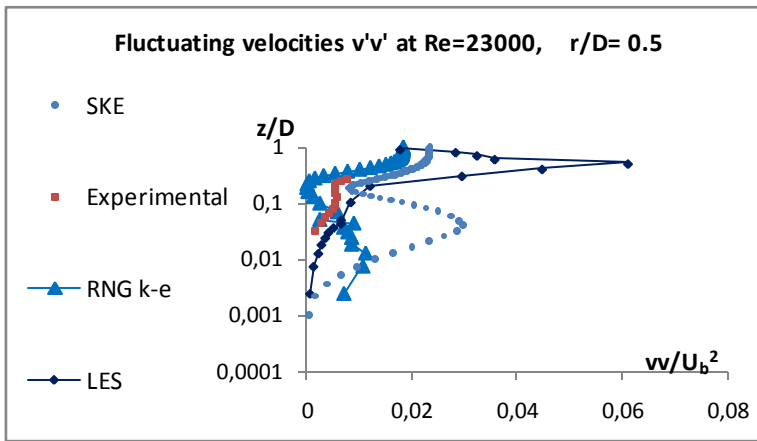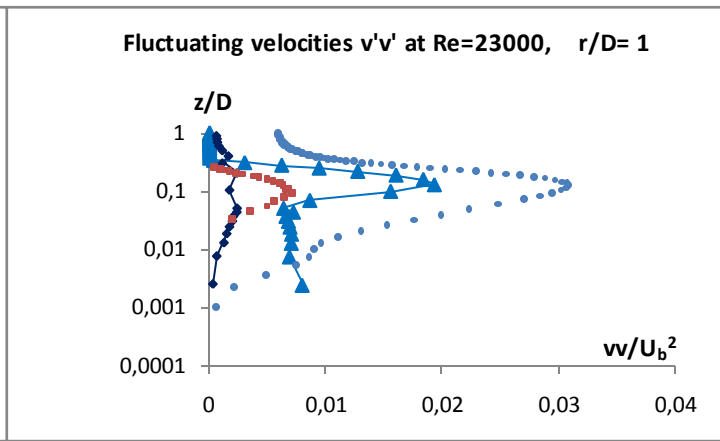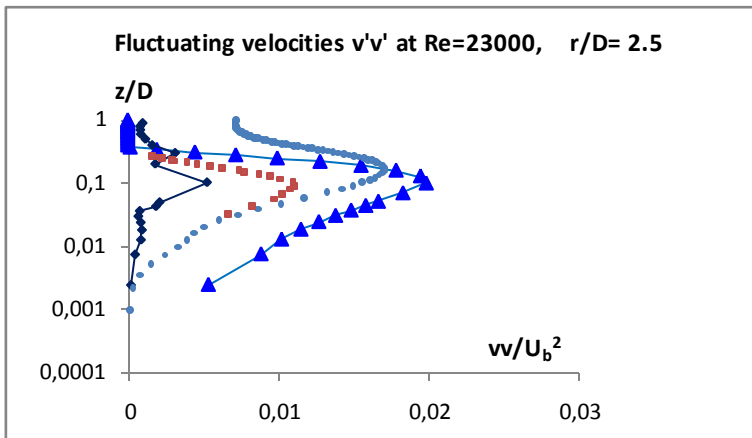| v'v'	v'v' turbulence		
r/D	r/D=3		
Statistic	v'v' magnitude		
Simulation	41K sim	LES	experimental
Normalized peak value	0.01312	0.005834	0.008
% deviation of sim from exp	64	27.075	

Table 7.3
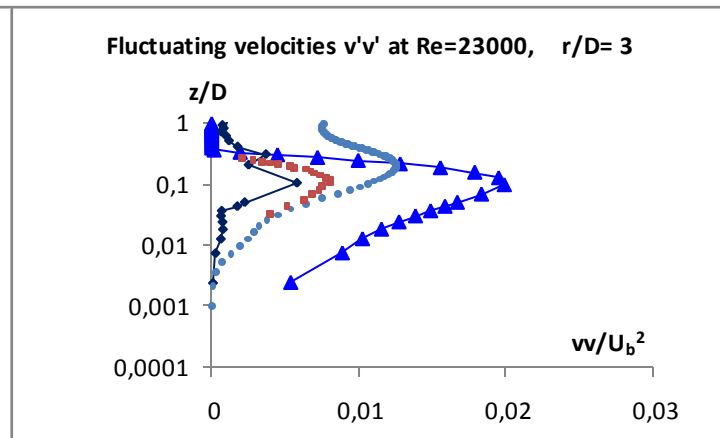
Figure 7.21

Figure 7.22

Figure 7.23

Figure 7.24

Figure 7.25

Figure 7.22 to Figure 7.25: Comparison between u'u' turbulence profiles from SKE, RNG K-ε, and LES simulations to Experimental profiles.

7.1.2.3   The $\overline{u'v'}$ observations:

Like for the $\overline{v'v'}$ profiles, $\overline{u'v'}$ profiles for experimental data can only be found for r/D=0.5, 1, 2.5, and 3.

When the $\overline{u'v'}$ profile plots are examined, it appears clear that the RANS simulations from this project have a spurious data point closest to the wall figures[Figure 7.26 & Figure 7.27]. This point was checked to originate from high $\frac{\partial u}{\partial z}$ values in the grid-point closest to the wall. $\frac{\partial u}{\partial z}$ is used in eq 3.9 from section[3.2.3] to calculate $\overline{u'v'}$. This data point occurs at z/D=0.0025.
It can be noted that this is well below the region in which ref[5] provides experimental data, which only extends down as far as y/D=0.03 for the $\overline{u'v'}$ measurements.
This missing near wall resolution of the experiments for the $\overline{u'v'}$ fluctuations may be due to the limitations of the double hotwire, needed to measure $\overline{u'v'}$ fluctuations.

Disregarding the first data point, the $\overline{u'v'}$ profiles of the RANS RNG k-ε simulations fit well with the profiles of ref[4].
The RNG k-ε $\overline{u'v'}$ profiles, and the profiles of the SKE simulations of ref[8] are also seen to give results that cohere relatively well (Figure 7.26).
The RNG k-ε simulations seem to somewhat over-predict $\overline{u'v'}$ values including the maximum $\overline{u'v'}$ value, and then seems to underestimate the profile slightly as the impingement plane is approached.
The whole RNG k-ε $\overline{u'v'}$ profile appears to be "elevated" in the z- direction compared to the profile from the experimental data (Figure 7.26).
It is seen when the Re_0=23K and the Re_0=230K RNG k-ε simulations are compared that the Re_0=230K simulation does not display the drop of in $\overline{u'v'}$ profile close to the wall.
However the (scaled) $Re_0 = 230K$ $\overline{u'v'}$ profile is observed to over predict all $\overline{u'v'}$ magnitudes on the profile (Figure 7.27).
The $Re_0 = 230K$ RANS simulations over predicts the peak of the $\overline{u'v'}$ profile slightly more than the $Re_0 = 23K$ RANS simulations.

When analyzing the $\overline{u'v'}$ profiles from the LES simulation, the following is found:
For the sake of having done a thorough investigation, the sub grid $\overline{u'_i u'_j}$ stresses from the LES simulation were calculated according to eq 3.35 from ref[10], and superimposed on the profiles for resolved $\overline{u'_i u'_j}$ stresses from the LES simulation.

$$\tau_{ij\ sg} = -2\mu_{t\ sg} + \frac{1}{3}\tau_{kk}\delta_{ij}$$

eq 3.35

This was done in order to check whether the unresolved turbulent stresses would give any substantial contribution to the total $\overline{u'_i u'_j}$ stress profiles.
As exemplified in figs[Figure 7.28 & Figure 7.29], the contributions from the sub grid stresses to the total $\overline{u'v'}$ stress profiles proved small. The same negligible contributions of the sub grid stresses were found for the $\overline{v'v'}$ and $\overline{u'u'}$ profiles.
Hence, the sub-grid stress contributions were considered to be negligible and were thus omitted from any lengthy analysis.

At r/D=0,5 the LES $\overline{u'v'}$ simulation profile of Figure 7.28 deviate substantially from the experimental data. The absolute value of the maximum LES $\overline{u'v'}$ value is approximately 300 times higher than the maximum $\overline{u'v'}$ value of the experimental data.

The LES profile displays a negative peak with magnitude -0.366 (normalized value $\left(\frac{\overline{u'v'}}{u_b^z}\right)$), as opposed to the experimental profile, which has values all in the range of $O(10^{-4})$ which is approximately equal to zero in comparison.

I.e. the experiments of ref[4] give approximately zero turbulent $\overline{u'v'}$ stresses at r/D=0.5, whereas the LES simulation gives the highest $\overline{u'v'}$ peak value for any of the r/D position at r/D=0.5 .

It may be noted that the experimental $\overline{u'v'}$ data of ref[4] have positive magnitudes, whereas the LES $\overline{u'v'}$ profile mainly consist of negative $\overline{u'v'}$ values.

The deviating signs (+ and -) describe two different representations of the turbulence physics of appendix[B], at r/D=0.5.

The physics of the $\overline{u'v'}$ stress component can be closer investigated in appendix[B].

u'v'	u'v' turbulence		
r/D	r/D=3		
Statistic	u'v' magnitude		
Simulation	41K sim	LES	experimental
Normalized peak value	-0.006118	-0.002997	-0.005057
% deviation of sim from exp	20.98081867	40.735614	

Table 7.4

In Table 7.4 the %-wise deviation of the turbulent u'v' fluctuations are tabulated for the 41K RANS simulation, and the LES simulation at r/D=1.5 & r/D=3
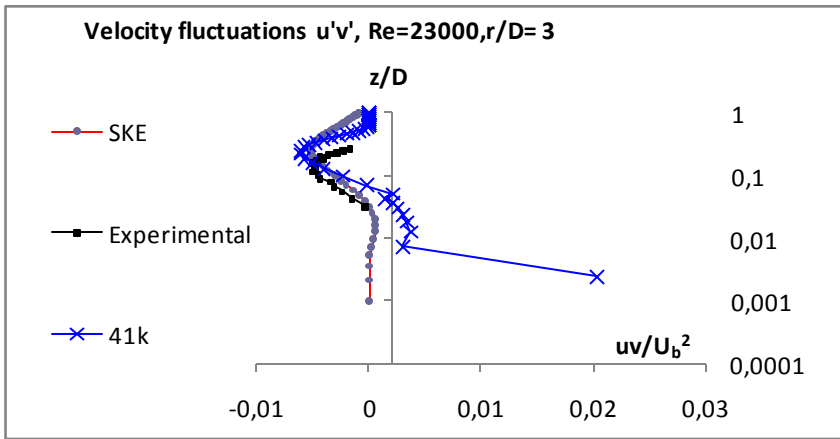
Figure 7.26

Figure 7.26: Comparison between u'v' turbulence profiles from Experimental values, against SKE 500K, and RNG K-ε 41K simulations.

Figure 7.27

Figure 7.27: Comparison between u'v' profiles from $Re_0 = 23K$ and $Re_0 = 230K$ RNG k-ε simulations
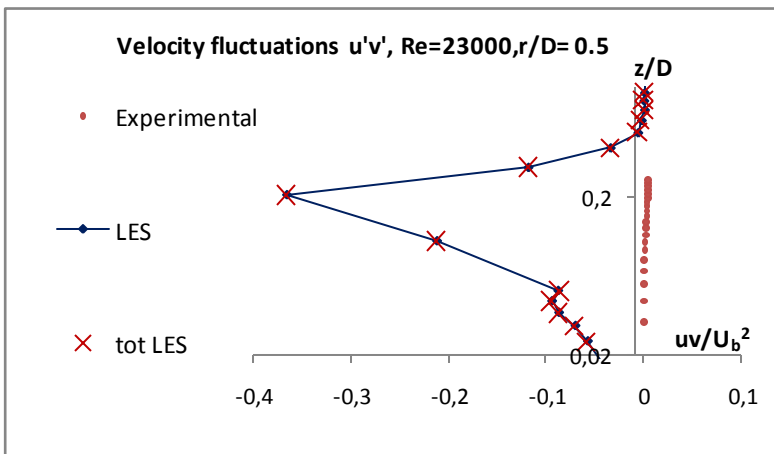
Figure 7.28
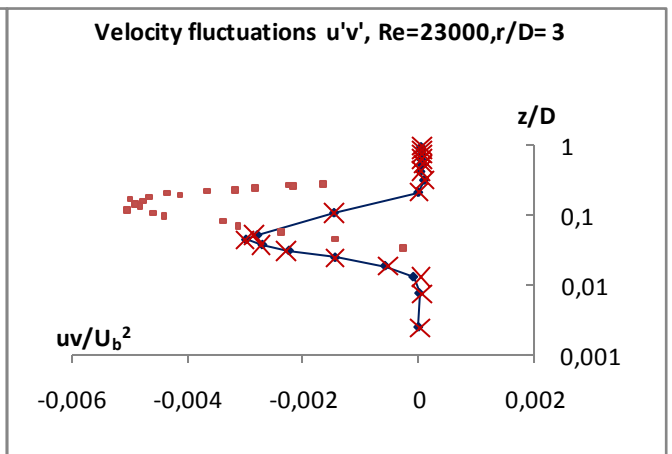
Figure 7.29
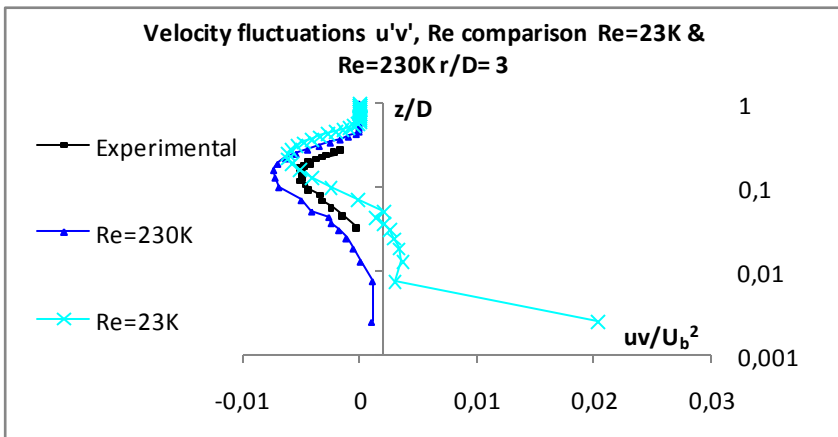
Figure 7.28 to Figure 7.29: Comparison between u'v' turbulence profiles from LES simulations with(tot LES) and without (LES) SGS stress contributions, to Experimental data.

78

7.1.3 Overall flow analysis:

In this part of the comparative analysis, the flow is examined from a more "distanced" vantage point. This meaning that the focus no longer is on the individual velocity or turbulence profile, but rather on how the overall flow develops within the domain of Figure 2.2 .

In order to gain this overview of the flow, the Spread rate and Velocity Decay plots described in sections[5.2.1 & 5.2.2] are used.

Like in the profile analysis sections, comparisons are made to form a basis for further analysis. These comparisons are:

1. Comparison between the different grid resolutions.
2. Comparison between simulations at different Re_0 values.
3. Comparison of experimental data and RANS simulations to the 1.3M LES simulation.

In addition the trends of the spread and decay plots are analyzed.

7.1.3.1 Spread rate

As was also seen for the individual profiles, the Spread Rate plots for the different RANS simulations of equal Re_0, show good accordance with each other.
This means that for a given Re_0 value, the different grid resolutions yield roughly the same trends and results.
This can be seen from Figure 7.35.
When examined, the spread rate curves show a linear development downstream $r/D \approx 3$ with gradients reported in Table 7.5 and Table 7.6.
In ref[4] the region where $r/D \leq 3$ is referred to as the impingement region, hence it can be said that the spread rate follows a linear trend outside the impingement region.

For some of the spread rate curves, especially the max velocity spread rate curves, and the spread rate curves for the coarser meshes (4K and 3D RANS), a pronounced stepwise behavior can be observed.
When the finer 41K mesh yields curves of stepwise behavior, the steps are smaller and come closer than the steps of the coarser mesh curves (4K and 3D RANS) figures[Figure 7.30 & Figure 7.31Figure 7.32]

As can be seen from figures[Figure 7.30 & Figure 7.31Figure 7.32], the 4K and 3D RANS meshes give virtually similar U_h and U_{max} simulation curves. Here the reader is reminded that the 4K mesh, and cross section resolution of the 3D mesh in the radial direction, are equal.
Finally the $Re_0 = 230K$ RANS simulations yield flatter spreadrate curves than the $Re_0 = 23K$ RANS simulations Figure 7.35.

When it comes to the spread rate of the LES velocities, they can be observed in figures[Figure 7.32 to Figure 7.34].
When compared to the RANS spread rate curves in Figure 7.34, it is seen that the LES velocity spread curves are much flatter than the RANS curves (Figure 7.34).
In fact the automatically generated spread rate curves of Figure 7.32 from the program of appendix[C], display large regions of absolutely no spreading of the U_h and U_{max} profiles of the LES curves with increasing r/D.
This was thought to be such a curious fact that the interpolated spread rate plot of Figure 7.33 was made.
This interpolation show that the spread rate curves have a slight spreading also of U_h.
Yet the interpolated spread rates show nowhere close to the magnitudes of the spread rates of the RANS simulations are seen to have in Figure 7.34.
However it is also observed that for r/D<4 the 4K RANS simulation and the LES simulation yield approximately the same spread rate (Figure 7.34).
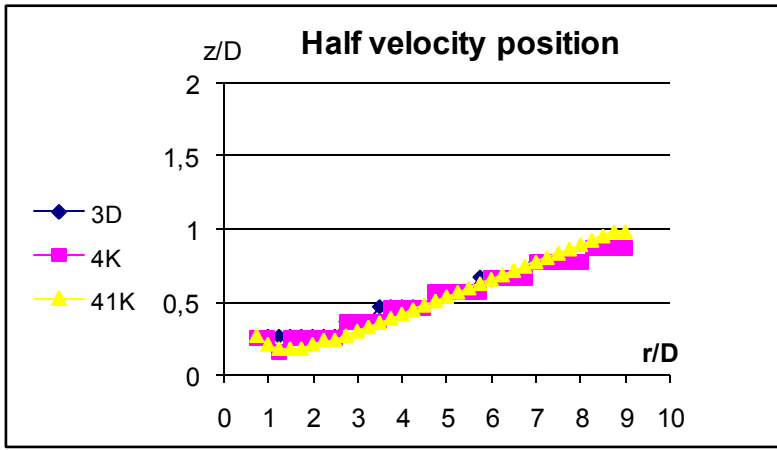
Figure 7.30
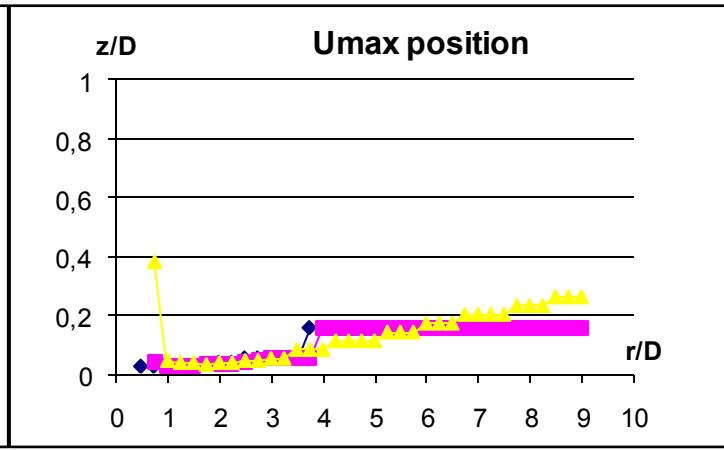
Figure 7.31

Figure 7.30 and Figure 7.31: Comparison between spread rates for the 3D, 4K, and 41K RNG k-ε simulations

Figure 7.32
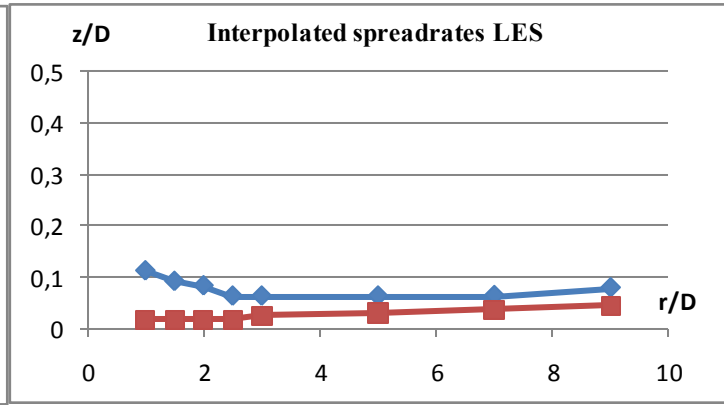
Figure 7.33

Figure 7.32 and Figure 7.33: Spread rates of Half velocities and max velocities for the LES simulation (Figure 7.32 is generated automatically (appendix[C]), while Figure 7.33 is interpolated)
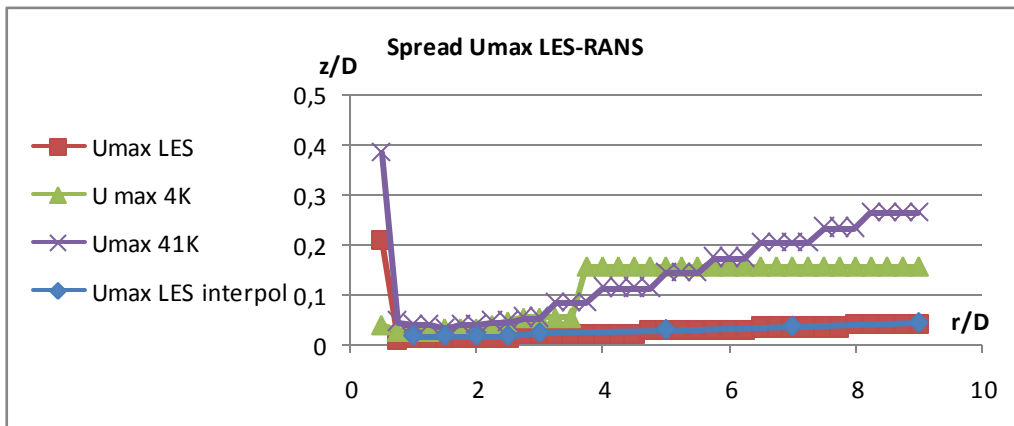
Figure 7.34

Figure 7.34: Comparison between Half velocity spread rates for the 4K, and 41K RNG k-ε simulations, and the LES simulation.

82

Half velucity spread comparison

z/D

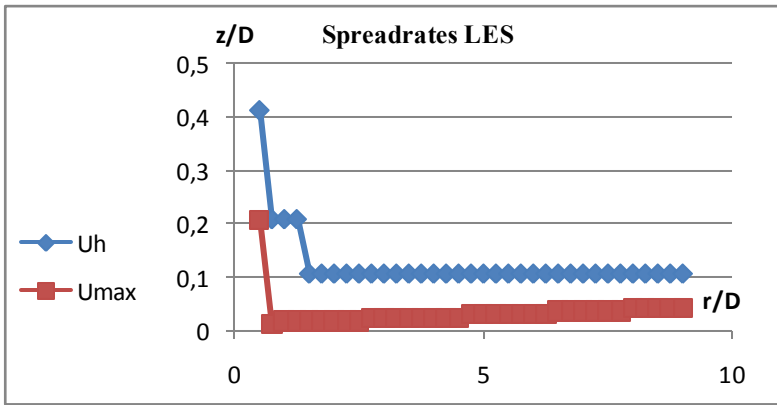- 3D S Re=23*10^4
- 4K S Re=23*10^4
- 41K S Re=23*10^4
- 4K US Re=23*10^5
- 41K US Re=23*10^5

r/D
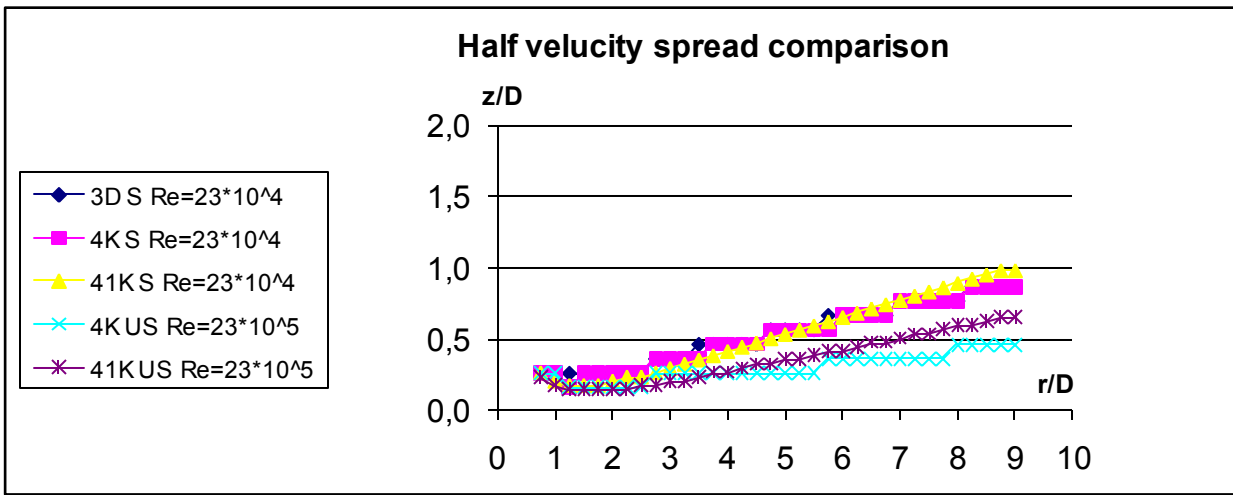
Figure 7.35:Comparison between Half velocity spread rates for the3D, 4K, and 41K RNG k-ε simulations at $Re_0 = 23K$ and $Re_0 = 230K$.

	Uh spread rates					
Re	23K			230K		
	$\Delta(r/D)$	$\Delta(z/D)$	$\Delta(z/D)/\Delta(r/D)$	$\Delta(r/D)$	$\Delta(z/D)$	$\Delta(z/D)/\Delta(r/D)$
3D	5.5	0.5118	**0.093**			
4K	5.5	0.5118	**0.093**	5.25	0.205	**0.039**
41K	5.5	0.65834	**0.1197**	5.25	0.4189	**0.0798**
LES	5.5	0	**0**			

Table 7.5

	Umax spread rates					
Re	23K			230K		
	$\Delta(r/D)$	$\Delta(z/D)$	$\Delta(z/D)/\Delta(r/D)$	$\Delta(r/D)$	$\Delta(z/D)$	$\Delta(z/D)/\Delta(r/D)$
3D	7.25	0.12349	*0.017*			
4K	7.25	0.12349	*0.017*	5.5	0.01821	**0.0033**
41K	4.5	0.17953	**0.0399**	5.5	0.0393	**0.00715**
LES	5.5	0.02557	**0.000465**			

Table 7.6

Table 7.5 and Table 7.6 contains tabulated data about the velocity spread curves of this thesis.

7.1.3.2 Decay

As was also seen for the individual profiles, the RANS velocity decay plots show good accordance for similar conditions. Meaning that for a given Re_0 value, the different grid resolutions yield roughly the same trends and results as can be gathered from Figure 7.40.

When curves for the velocity decay of the RANS simulations are plotted in a double logarithmic diagram as exemplified for the 41K RANS simulation in Figure 7.37, the curve takes on a linear shape for r/D≥ (2.5 − 3).

From the linear trend of the log-log plot it can be concluded that the curve of the velocity decay outside of r/D≈3 fits an exponent function on the form $u = A \left(\dfrac{r}{D}\right)^m$
, where m is the incline of the curve in the log-log plot.
The functions for the fitted curves are displayed in Table 7.7.

The approximated curves resulting from this operation are displayed in Figure 7.39, and the 41K degrading curve together with its fitted curve is displayed in Figure 7.38.

In Figure 7.40, the decay curves for the 41K, 4K AND 3D RANS simulations at Re_0=23K, are plotted together with the curves for the 41K and 4K simulations of Re_0=203K.
It is observed that for the low Re_0(23K) simulations, a refinement of the mesh leads to a less curved degrading graph, and higher velocity values for 1≤r/D≤4.5.
For the high Re_0 (230K) simulations, the same mesh refinement brings about lower U_{max} velocity magnitudes, hence giving a lower degrading curve (Figure 7.40).

For the high Re_0 (230K) simulations, the linear relation in the double logarithmic plot is not as clear as for the low Re_0(23K) simulations, hence the Re_0 (230K) simulations do not inhere the same exponent- function properties as the low Re_0 (23K) simulations.

The LES simulation, in turn, yields the decaying curve shown in Figure 7.41 together with the RANS decaying curves.
When compared to the decaying curves of the RANS simulations and the curve from the experimental data for r/D≤3, a number of differences are observed.
Firstly, the decaying curves of the LES and RANS simulations cohere well for r/D≤ 0.75.
After this point however, the negative slope of the LES curve is far flatter, and displays far less curvature than the RANS generated curves.
In fact it appears to be close to linear for r/D≥ 4-5
For r/D≈4 the negative gradient of the LES curve is steeper than those of the RANS curves.
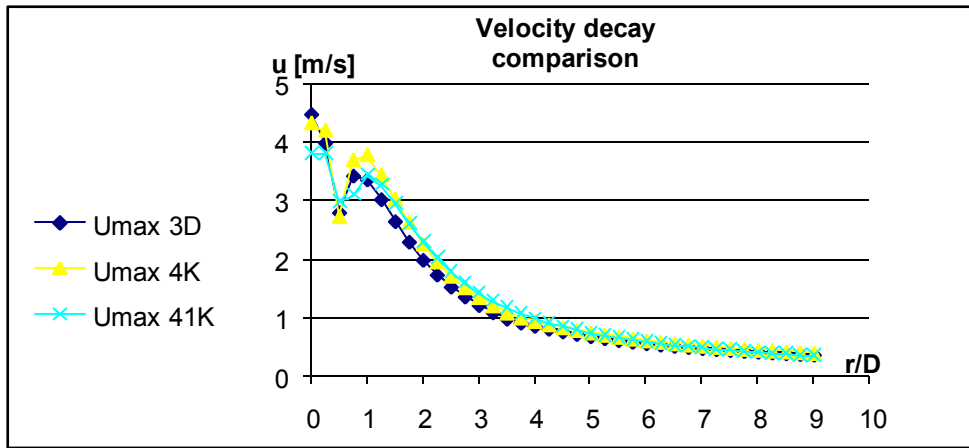
Figure 7.36Comparison of decaying curves for 3D,4K, and 41K RNG k-ε simulations
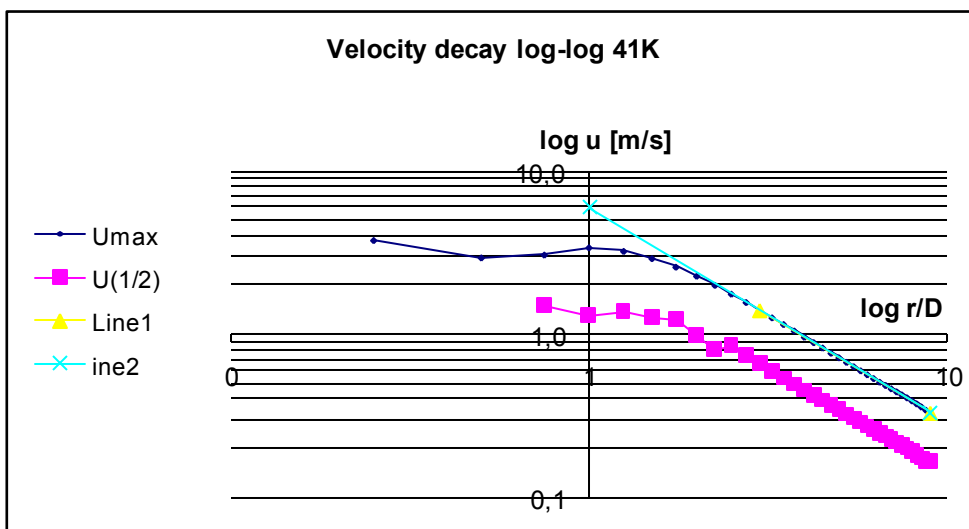
Figure 7.37: Double logarithmic plot of decaying curve of 41K RNG k-ε simulation
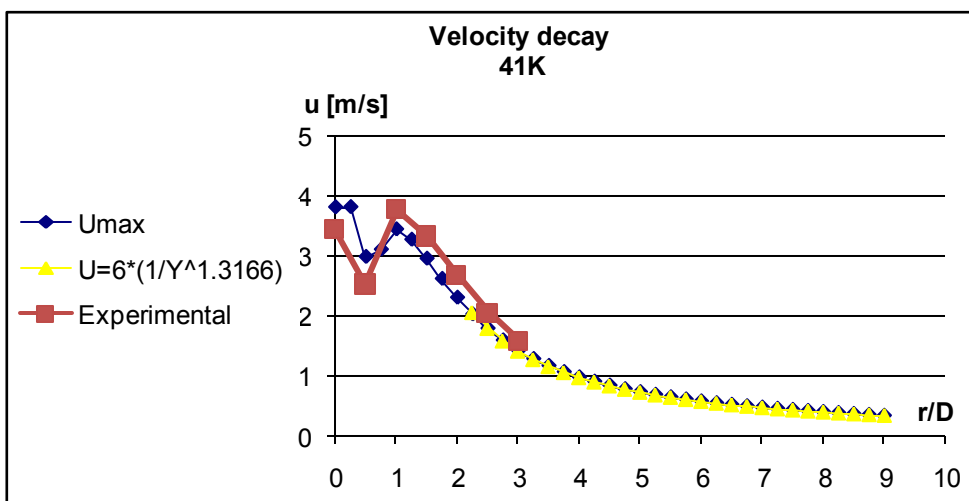
Figure 7.38: Decaying curve of 41K RNG k-ε simulation (blue), together with fitted curve (in yellow), and Experimental decaying curve (red)

Velocity decay curve fit
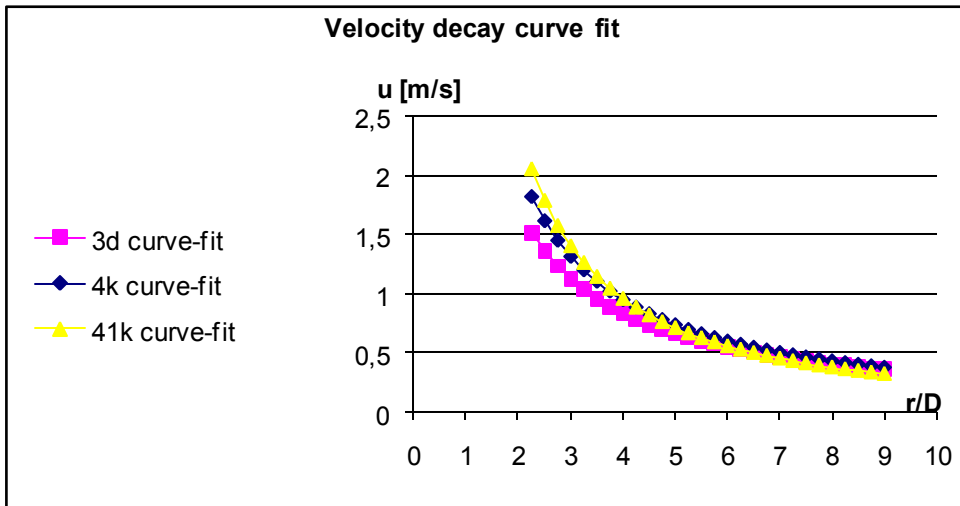
Figure 7.39: Fitted decaying curves for 3D, 4K, and 41K RNG k-ε simulations.

Velocity decay Re comparison
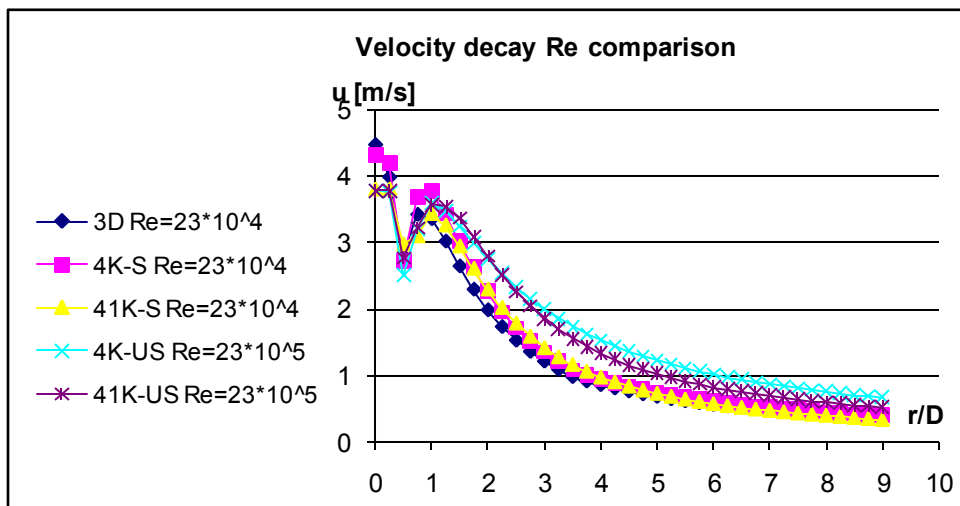
Figure 7.40: Decaying curves for 4K, and 41K RNG k-ε simulations at $Re_0 = 23K$ & $Re_0 = 230K$, and 3D simulation decaying curve for $Re_0 = 23K$.

Velocity decay LES v.s. RANS
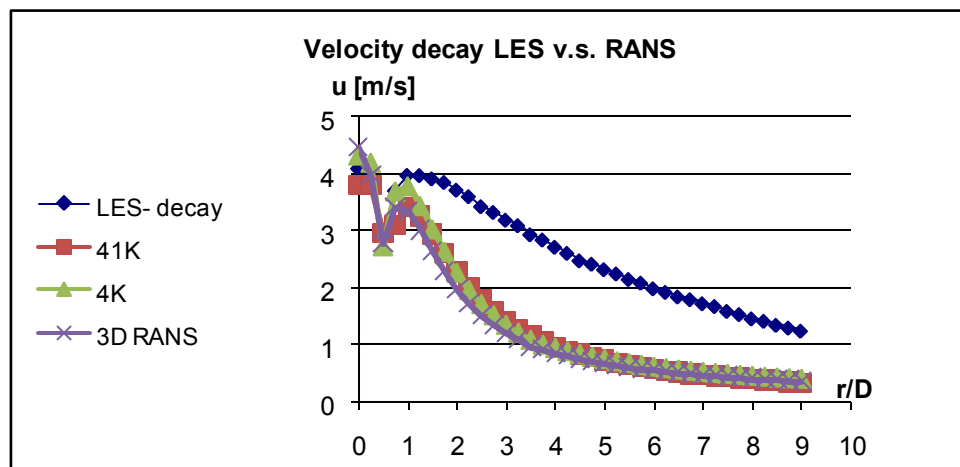
Figure 7.41: Comparison between decaying curves for 3D,4K, and 41K RNG k-ε simulations, and decaying curve for LES simulation.

86

Mesh	curve fit function r/D≥3
3D coarse	$$U_{max} = 3.55\left(\frac{1}{(r/D)^{1.042}}\right)$$ eq 7.1
4K	$$U_{max} = 4.55\left(\frac{1}{(r/D)^{1.275}}\right)$$ eq 7.2
41K	$$U_{max} = 6\left(\frac{1}{(r/D)^{1.317}}\right)$$ eq 7.3

Table 7.7

Table 7.7 tabulates the curve-fitting functions for the decaying curves for some of the simulations of this thesis.

7.1.4 Nozzle Jet:

In order to gain an overview of the flow throughout the whole domain, the inlet jet velocity profiles from J of Figure 2.2 were examined.
The plots accompanying this section show vertical z velocity plotted against r/D.

As the flow exits the nozzle J in Figure 7.42, it has already been treated like section[4.5] explains, in order to be a fully developed turbulent pipe flow of $Re_0 = 23K$.
As can be seen from figures[Figure 7.42 to Figure 7.44], the exit profile shapes of the LES and the 41K RANS simulations are not similar.
The flatter "nose" region of the RANS profile indicates higher levels of $\overline{u'v'}$ stresses at the nozzle exit of Figure 7.42 (see appendix [B]).

Knowing that both the RANS and LES inlet profiles were initiated from fully developed turbulent pipe flow RANS simulations, described more thoroughly in section[4.5], and that the RNG k-ε RANS model that was used is known to give good results for wall bounded flows ref[7], the fundament for the boundary conditions would appear to be solid.
It was indeed verified that the RANS boundary profile used as a boundary condition for the nozzle of the LES simulation, was equal to the inlet profiles of the RANS simulations.
However, as explained in section[4.5], LES simulations need to initiate unsteady turbulence from steady boundary conditions (e.g. RANS simulations).
In this thesis, a spectral synthesizer method was used for this purpose as explained in section [4.5] and ref[10].

I n addition to the peak of the RANS profile being "flatter" it is observed that the RANS and LES profiles react differently as the impingement plane is approached.
For the RANS jet of figures[Figure 7.43 & Figure 7.44], the stagnation point seems to affect the jet further away from the impingement plane then what is the case for the LES jet.

In Figure 7.45 it is seen that the LES peak velocity shape equivalent to the RANS peak velocity shape at z/D=0.5, can be found at z/D=0.25.
Here, however, the LES velocity magnitudes are far lower than the RANS velocity magnitudes.
As can be seen from figures[Figure 7.42 to Figure 7.44], the radial spreading of the jet profiles is slightly higher for the RANS compared to the LES profiles.
This may be caused by the suspected higher $\overline{u'v'}$ turbulence of the RANS jet profile (appendix [B]).
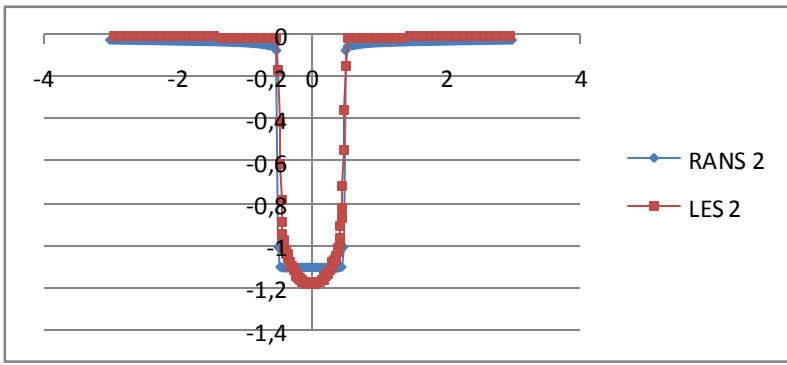
Figure 7.42 displays the nozzle jet profile at z/D=2.0

Figure 7.43 displays the nozzle jet at z/D=1.0
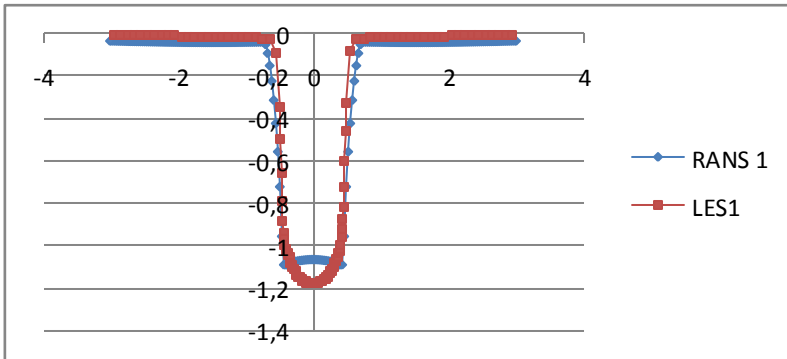
Figure 7.44 displays the nozzle jet at z/D=0.5
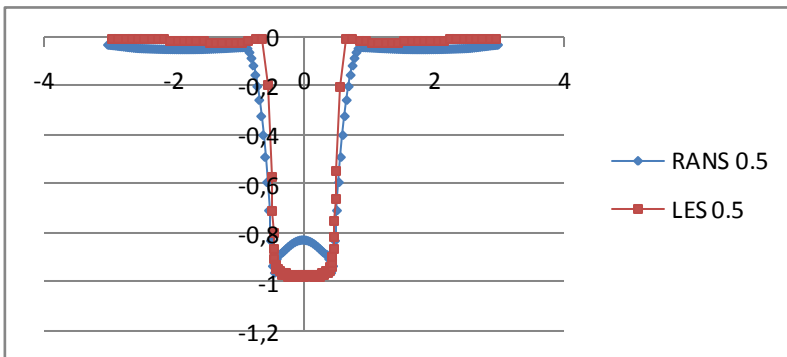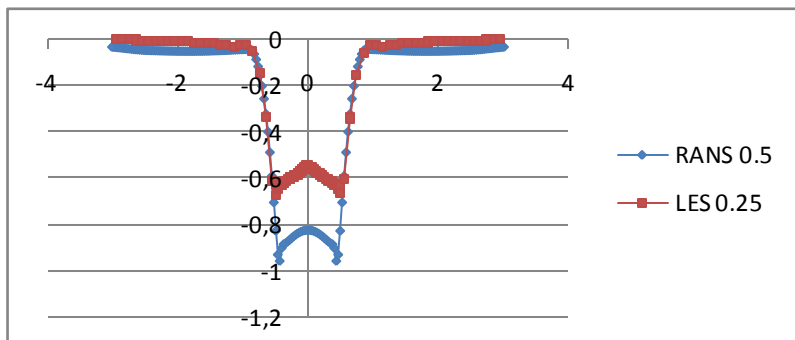
Figure 7.42to Figure 7.45: LES and RNG k-ε nozzle jet velocity profiles at z/D=2, 1.5 ,1, 0.5   Figure 7.45: compares jet profiles of RNG k.ε at z/D= 0.5 and LES at z/D =0.25

89

8   Discussion/ Discussion of results comparative analysis:

In this section interesting observations and connections found from the observations made in section[7.1] are discussed.
Solutions or reasons for the problems that appear from the constellation of the data and results of section[7.1] will also be discussed .

Some of the observations made in section[7.1], will not be discussed any further in the following sections.
Such omissions should be regarded as a sign that the phenomena were in fact noticed and investigated, but that no results worthy of any lengthy discussion came from the investigation.
Hence the structure of this section will not be like in section[7.1] where each separate profile-type and plot was investigated separately.
Rather, the current section will focus on tying the observations and facts of section [7.1] together, and linking them to the theory of section[3] and appendices[B-D], like Figure 6.8 and Figure 6.9 of section[6.2] illustrate.

8.1   Flow Details

From the investigation of the observations made in section[7.1], the following results were considered appropriate for further analysis and discussion:

A) RANS simulations:

   1) Good agreement between RANS simulations of this thesis, and reference experiments and simulations.
   2) RNG k-ε on coarse mesh outperforms SKE simulations on fine 500K mesh.
   3) Convergence of decay plot of low and high Re_0 values
   4) Higher Reynolds numbers Re_0 give lower spread rate incline.

B) LES simulations:

   5) Discrepancies in LES profiles away from impingement
   6) LES inlet jet-profile differs from RANS inlet jet profile
   7) LES jet develops differently from RANS jet when impingement plane is approached.
   8) LES generally predicts profile <u>shapes</u> well, but give suspicious profile magnitudes with increasing r/D.
   9) Less spreading of wall-jet flow coheres well with higher peak velocities for LES simulation (preservation of momentum).
   10) Good coherence between experimental data and LES for r/D $\leq$ 1.5
   11) Sub Grid stresses found to give negligible contributions to resolved turbulent stresses.
   12) RANS: U_h and U_{max} spreadrates "diverge", LES, U_h and U_{max} spreadrates "converge"

C) Domain/Mesh related:

13) Grid possibly affecting spread rates, and overall solution
14) Stepwise spread rate curve behaviour: grid related?

8.2   RANS simulations:

As reported in section[7.1], there is good agreement between the experimental data, and the RNG k-ε RANS simulations.

Interestingly, when studied closer, the RNG k-ε model is found to yield better results for the velocity profiles at all r/D positions and for at all grid resolutions (3D-160K, 4K, and 41K), compared to the SKE simulation of ref[8], which was made on a 500K mesh.
From this observation it is possible to draw a likely conclusion:
Firstly, if the goal for the RANS simulation merely was to get good agreement to experiments for the velocity profiles, a grid resolution equivalent to the 4K 2D mesh, would appear to be sufficient, since all RNG k-ε velocity profiles match the experimental profiles better than the SKE simulation of ref[8].
In other words the number of grid cells could be cut by more than a factor of 100 (500K/4K=125) compared to the simulations of ref[8], thus tremendously reducing the computational requirements of the simulation.
This discovery/ assumption was used as a basis for the generation of the 3D meshes in the stage illustrated in Figure 6.2 of section[6.2], and can be thought of as being a part of the "ideas" cloud.
When the profiles for turbulent stresses are analyzed for the RANS simulations, it is found that resolutions equivalent to the 4K mesh (includes 3D meshes of 160K and 1.3M resolutions) in general give good results.
However, in order to get turbulence profiles that can be relied on to agree well with experimental data, a grid resolution equivalent to the 41K mesh would appear to be the safe solution seen from the plots of sections[7.1.2].
As reported in section[4.5.2 and 4.5.3] the computational requirements of the 3D simulations (RANS and LES), effectively hindered the luxury of extra grid refinement for the sake of safety, hence the 3D meshes were constructed to match the resolution of the 4K mesh like reported in section[4.5.2] and visualized in section[6.2].

When the overall flow pictures of the RANS simulations were analyzed, the results from the high and low Re_0 simulations, 23K and 230K respectively, were found to give the U_{max} velocity decaying profiles of Figure 7.40.
Like reported in section[7.1.3.2], the high and low Re_0 profiles seem to approach each other as the grid resolution is increased.
The decaying curves of the SRN IJF problem may be suspected of having an inherent convergence on some shared decaying curve common for all scaled U_{max} decaying profiles.
This type of behaviour would probably require a constant H/D ratio, and an Re_0 value ensuring a fully turbulent jet coming out from the nozzle J of Figure 2.2.
However, in order to argue more for or against such a converging decaying curve behaviour, a more comprehensive study would have to be carried out.

Further, when the RANS spread rate curves are investigated, they display the reported linear development for r/D> 2.5 reported in section[7.1.3.1].
A behaviour of the spread rate curves worth noticing is that the low Re_0 simulations (23K), give spread rate curves of higher incline than the high Re_0 simulations (230K).
This, seen in context with the previous paragraph about the shared U_{max} decaying profiles of low and high Re_0 value simulations, reveals something about the IJF flow.
Since the scaled maximum velocities of high and low Re_0 simulations decay at much the same rate, albeit the high Re_0 simulations yield flatter spreading rates resulting in narrower wall-jet profiles, the

viscous and turbulent dissipation along the impingement plane is likely to be higher for IJF flows with high Re_0 values.

This is probable since the higher spreading of the low Re_0 flow leads to a diffusion/spreading of the momentum of the wall jet profile hence spreading the momentum.

So since decaying rates are approximately equal Figure 7.40, but the diffusion of the high Re_0 simulations is lower, the viscous and turbulent losses are likely to be causing the extra losses in momentum of the high Re_0" wall-jet" profiles.

8.3   LES simulations:

As reported in section[7.1] the LES simulation delivers results of varying promise.
To sum up section[7.1], the LES results close to the centre axis r/D=0, look very promising indeed.
As can be seen from figures[Figure 7.6, Figure 7.8, Figure 7.16, and Figure 7.17], both the velocity profiles and the turbulence $\overline{u'_1 u'_1}$ profiles of the LES simulation in general match the experimentally acquired profiles very well for r/D≤1.5.

For larger r/D values, the agreement between experimental profiles, and the LES simulation profiles steadily deteriorate as r/D increases.
The deterioration is mainly manifested through the LES displaying the following tendencies:

1. Higher peak velocity of wall jet profiles (Figure 7.10)
2. "Narrower" wall jet velocity profiles (Figure 7.10)
3. Lower magnitudes for $\overline{u'v'}$ wall jet profile (Figure 7.29)
4. "Narrower" $\overline{u'v'}$ wall jet profiles (Figure 7.29)
5. Lower magnitudes for $\overline{v'v'}$ wall jet profile (Figure 7.23)
6. Lower magnitudes for $\overline{u'u'}$ wall jet profile (Figure 7.18)
7. Flatter velocity spreading rate curves (Figure 7.34)
8. Slower radial decaying of maximum velocity (Figure 7.41)

It will in the following discussion become clear that the RANS and experimental data are thought to be correct outside r/D≈1.5, whereas the somewhat deviating LES profiles are thought to be caused by some error that will be sought after.

8.3.1   The differing LES profiles

The following section comprises a collection of possible causes for the observed deviating behaviour of the LES simulations.
Each possible cause will be discussed with the aim of clarifying its likely influence on the flow of the LES simulation.

8.3.2   Initial and boundary conditions:

Intuitively the region close to impingement (r/D=0) should be the area most difficult to simulate, since it houses the most difficult effects to predict like stagnation, high streamline curvature, and high accelerations.
In fact the RANS simulations seem to build under this assumption , since especially the turbulence profiles improve in relation to experimental values away from the centre axis from very poor

agreement at r/D=0, to good agreement at r/D=1.5 as figures[Figure 7.16 & 7.18, and Figure 7.22 &Figure 7.24]
illustrate.
However it is seen in figures [Figure 7.1 & Figure 7.2, and Figure 7.12 & Figure 7.13] of section [7.1] that also the agreement
between RANS and experimental data deteriorates slightly after r/D=1.5.
The LES simulation was initiated by using the converged and checked steady 1.3M RNG k-ε RANS simulation LIKE Figure 6.6 of section[6.2] as an " initial volume profile".
This initial RANS simulation was checked to yield results similar to
the 3D RANS simulation as Figure 6.5 indicates.
Further all outlet boundary conditions for the LES profile were set to "pressure outlets",
identically to the RANS simulations of this thesis and the simulations of ref[6 & 8].

Hence the LES simulation is seen to create its "RANS deviating" characteristics of its own accord.
It is also seen that the LES profiles develop especially clear deviations in the velocity profiles, and in the $\overline{u'v'}$ profiles away from r/D≈1.5, from a solution which initially was a RANS RNG k-ε simulation
The velocity profile deviation from experimental values is exemplified by. Figure 7.10.
Thus, if the experimental data are believed to be physically "correct", the fact that the RANS simulations outperform the LES simulation for r/D ratios larger than r/D≈1.5 for all profiles except for $\overline{v'v'}$ profiles, which the RANS k-ε models miscalculate severely for all r/D positions with the explanation of section[7.1.2.2].
This poor performance of the LES poses quite an enigma.
In the following sections the reason for the deviations found from the LES simulation is sought.

8.3.3 Reynolds stresses

The search for the root of the reported discrepancies in the LES simulations, begins with the analysis of the observations 3.→6. made in the section[8.3], i.e. observations concerning the turbulence profiles.

When the turbulence profiles are examined, it is recognized that all the $\overline{u'_i u'_j}$ stresses are under predicted in terms of magnitude for r/D≥1.5 .
In addition it is recognized that the $\overline{u'v'}$ component displays a narrower profile in the z direction, than the experimental and RANS profiles outside r/D≈1.5.
In practise this means that for the LES simulation, the region affected by the near wall turbulence is far narrower than what is the case for the RANS and experimental data.
Appendix[B] should be consulted for the physical interpretation of the $\overline{u'v'}$ term.
When looking at the profile plots, the reader should bear in mind that the z-axis has been logarithmically scaled.
This means that differences in the z direction in reality are far greater than what the plots give impression of.
Bearing this in mind, the possible impact of the difference seen in Figure 7.29 appears ever more important.

The magnitudes of the three Reynolds stress component profiles for the LES data, compared to the experimental data are as follows:

- $\overline{u'u'}$ magnitude is lower
- $\overline{v'v'}$ magnitude is: lower

- $\overline{u'v'}$ magnitude is: lower

The locations of the peak(s) of the three Reynolds stress components are situated as follows in the z/D direction for the LES data, compared to the experimental data:

- $\overline{u'u'}$ peak is situated: approximately same z/D
- $\overline{v'v'}$ peak is situated: approximately same z/D
- $\overline{u'v'}$ peak is situated: (far) lower z/D

Thus the general picture of the turbulence in the LES flow, compared to the flows of the experiments and RANS simulations outside r/D≈1.5 is; that there is less turbulence in terms of magnitude, and what turbulence there is, is in the case of the $\overline{u'v'}$ stresses situated closer to the impingement plane for the LES simulation.

As can be gathered from appendix[B], the $\overline{u'v'}$ stress component is responsible for effects clearly acting to diffuse the velocity profile.

Quadrant II and IV give intuitive descriptions of how the diffusion may happen, i.e.:

Q II   Low velocity element enters region of higher velocity
Q IV: High velocity element enters region of lower velocity

When seen in relation with the physics of appendix[B], it becomes clear that the under prediction of wall-near turbulence of the LES simulation probably would cause a lower spreading and slower decaying of the wall-jet velocity profile.

This is, as can be observed in section[7.1], indeed the case.

However there should be some plausible explanation as to why these mal-predictions of turbulence are made in the LES simulation.

8.3.4 Inlet profile

After the jet profiles exiting from the nozzle J(Figure 7.42) are checked in section[7.1.4], the most important findings can be summed up in the following way:

Firstly it is seen from figure Figure 7.42 that the peak-shape of the axial velocity profiles at the nozzle outlet differ from the RANS to the LES simulation.

The RANS profile displays more of the characteristic flattened/ "blunt" peak shape associated with fully developed turbulent pipe profiles (consult appendix[B]), whereas the LES profile displays a profile shape more similar to the typical "round nosed" laminar profile shape.

Knowing that both the RANS and LES inlet profiles were initiated from fully developed turbulent pipe flow profiles, described more thoroughly in section[7.1.4], and that the RANS model used is known to give good results for wall bounded flows ref[7], focus must be put on what makes the boundary conditions for the LES simulation differ from the RANS simulations when looking for the reason for the differing jet- profiles shapes.

As explained, it has been verified that the RANS boundary profile used to create a boundary condition for the LES nozzle jet , is equal to the inlet profiles of the RANS simulations.

However, as explained in section[4.5], the LES simulation needs to initiate unsteady turbulence on boundaries where the inflow is turbulent.

In this thesis, a spectral synthesizer method was used for this purpose as explained in section [4.5], and ref[10].

Since the steady jet inlet boundary profile of the LES is the same as for the RANS simulations boundary profiles, albeit the time average of the unsteady velocity profile of the LES simulation deviates from the RANS profiles, it is suspected that there is some error connected to the initiation of the unsteady turbulent boundary conditions in the LES simulation.
It is unknown what might have caused this error, as advice from ref[10] and the FLUENT-user homepage (accessible from www.fluent.com), were followed with great care for the initiation of unsteady boundary conditions.

Further, it is also seen that the velocity profiles for fixed radial r/D positions of section[7.1.1] give better agreement between the LES simulation and experimental data, than between RANS simulations and experimental data close to the centre axis as figs[Figure 7.6 to Figure 7.9] exemplify.
So in this respect, the suspected faulty axial LES inlet-jet profile does not cause erroneous radial profiles close to the impingement point.

There could yet remain a possibility that the flow passing "above and past" the impingement point might cause the simulations to develop differently further away from r/D=0, due to differences in turbulence transport, and velocity .
In this way, an erroneous inlet-jet profile could affect the flow away from the centre axis, yet give good results near r/D=0.
This could happen due to the effects caused by the stagnation zone, dominating in the immediate vicinity of r/D=0.

This possibility can probably be discarded as the main cause though, as the radial LES profiles for velocity and turbulence, display good agreement with experimental results for z/D positions further away from the impingement plane.
The plotted profiles extend as far in the z/D direction as z/D=2, i.e. to the z position of the nozzle outlet J of Figure 2.2, and should thus have been able to capture any phenomena for z/D positions away from the impingement plane.

However since no substantial deviations in turbulence or velocity transport can be found in the LES simulation for r/D ratios close to impingement for any z/D ratios, the inlet jet may probably be dismissed from being the cause of the deviations found for r/D ratios further away from the centre axis (r/D=0).

To conclude, it seems unlikely that properties of the LES inlet jet-profile of section[7.1.4] figs[Figure 7.42 to Figure 7.45] are responsible for the incoherence between the LES results, and RANS and experimental results away from r/D≈1.5.
This seems plausible since the LES and experimental profiles are well matched close to r/D=0, and remain so until r/D≥1.5.

8.3.5 The mesh effects

There seems to be no apparent reason why the 3D RANS simulation should yield the velocity profile with the lowest velocity values among the RANS simulations, and at the same time the LES simulation should yield velocity profiles displaying very high peak values, and slow decaying rates knowing that both simulations originate from the same boundary conditions, and that the LES simulation in fact uses the RANS simulation as an initial condition (Figure 6.7).
It also seemed unlikely at first for the reported discrepancies in the LES simulation to be caused by the computational mesh, since the very same mesh was used in the RANS simulations verified like Figure 6.7 illustrates.
However when more closely analyzed a few previously unforeseen relations emerge.

One of the obvious signs that the flow of LES simulation, deviates from the flow of the RANS simulations and experiments, is the difference in the velocity position curves reported in section[**Feil! Fant ikke referansekilden.**], and well exemplified by figs[Figure 7.32,Figure 7.33, and Figure 7.34].

The LES half-velocity position found by the programme of Appendix[C] is situated constantly at z/D=0.106, which is the exact z/D location of the first vertical grid point above the top of the boundary layer cells.

The grid spacing from the top of the boundary layer to this cell is 0.05D, whereas the spacing to the next cell is 0.1.

The grid is uniform in the z-direction for the whole domain above the boundary layer, which is exemplified in fig [D] of appendix[E] .

 It is clear that the grid experiences a sudden change in grid point Δz right after the boundary layer cells (fig [E] of appendix[E]) .

In ref[10] the user is advised to be careful with introducing sudden changes in grid point distances, and mesh skewness. This is said to be especially important for LES simulations.

The meshes of this thesis, including those used for LES simulations, were made based for, and mainly tested on, RANS simulations as can be gathered from study of section[6.2].

For the RANS simulations the changes in grid point spacing, had no obvious effect, and the simulations cohered well with experimental results as reported in section[7.1].

The changes in grid point spacing may however have contributed to the spuriously low spread rate, and velocity decaying rates reported for the LES simulation in sect[7.1.3].

The fact that the half velocity position of Figure 7.32 is seen to be situated exactly at z/D=0.106, which is the z/D location of the first grid point above the boundary layer may be an important observation.

Since the Δz grid spacing gets coarser after the top of the boundary layer, the velocity found in the grid point above z/D=0.106 is found at z/D=0.208, thus giving the velocity profile a long way to drop off towards zero. This means that the first position above the z/D location of the maximum velocity found to have less or equal to half the U_{max} value is found at the z/D=0.106 point see appendix[C] for how the half velocity U_h position is found.

Thus it appears likely that the coarseness of the grid is responsible for the completely flat U_h Spread rate curve of Figure 7.32.

When checked, it can also be concluded that the stepwise spread rate curve shape seen in e.g. Figure 7.31 can be attributed to mesh coarseness, because each "step" occurs at z/D positions equal to the grid-point locations, and the z-wise length of each step exactly matches the local Δz distance of the mesh.

This means that the finer the mesh is, the more the spread rate curves will resemble smooth curves.

However, the interpolated spread-rate curves plot of Figure 7.33 still display very low spreading rates for the LES U_h and U_{max} profiles.

So the reported low decaying and spreading rates of the LES velocity profiles of section[7.1.3] will itself have to be explained in hope of clarifying the deviating behaviour of the LES simulations.

Further the highly stretched boundary cells *(*fig [C & D] of appendix[E]) within the boundary layer, might introduce some unwanted effects to the flow, ultimately resulting in the reported discrepancies for the LES simulation.

For instance, it is observed in section[3.1 & 3.2], and in ref[10] that the LES code in fluent uses the grid cell volume for filtering and SGS modelling, assuming constant and equal $\Delta x, \Delta y$, and Δz distances.

Then to have inhomogeneous grid features like described in this section, could in fact jeopardize the solution accuracy like explained in the following discussion.

Upon inspection, section[3.5] reveals some potentially clarifying facts about the Smagorinsky Lilly model.

The observation is that in the Smagorinsky-Lilly model the turbulent viscosity ν_t is directly coupled to the mixing length l_s, which in turn, according to expression

$$l_s = \min \begin{cases} \kappa y \\ C_s V^{-\frac{1}{3}} \end{cases}$$ (eq 3.39) is directly coupled to the grid cell volumes.

As can be seen from the expression $l_s = \min \begin{cases} \kappa y \\ C_s V^{-\frac{1}{3}} \end{cases}$, the model assumes the grid cells to

have equal sides since the length scale is computed as $V^{-\frac{1}{3}}$, where V is the volume of the grid cell.

If the model was to be used on a mesh of highly skewed cells, the mixing length would thus be miscalculated, due to the $V^{-\frac{1}{3}}$ term.

Further, according to ref[9] the mixing length l_s can be expressed as $l_s = C_s \Delta$, where Δ is the length scale of the largest subgrid scale eddies, and therefore the lengthscale associated with the filter described in section[3.5].

To get a picture of the physical meaning of the mixing length l_s, sections[3.2 & 3.3] may be consulted.

Four of the most clarifying expressions with regard to l_s from these sections are displayed below:

a) $\mu_t = \rho l_s^2 \left(\frac{\partial \overline{u}}{\partial y} \right)$

b) $\tau_t = \mu_t \left(\frac{\partial \overline{u}}{\partial y} \right)$

c) $\tau_t = \rho l_s^2 \left(\frac{\partial \overline{u}}{\partial y} \right)^2$

d) $\tau_t = \mu_t \frac{\partial \overline{u}}{\partial y} = -\rho \overline{u' v'}$ (for the 2D case).

As a)→c) illustrates, the mixing length l_s is a vital part of the turbulent viscosity μ_t, hence also a vital part of the turbulent stress τ_t.

Thus it can be gathered from d) that l_s plays an important role in the prediction of the turbulent fluctuation components.

It should be noted that the expressions of a)→d) are deduced from a RANS velocity representation (section[3.2.1]), and therefore cannot be directly implemented in the approach of filtered velocities of the LES approach (section[3.5]) .

Yet the equations give a correct and intuitively comprehendible description of the modelling of l_s, and its relation to turbulent stresses and fluctuations.

In retrospect it appears that greater care could have been taken to ensure that the computational mesh for the LES simulations had grid cells of even more equal sides on the whole computation domain.

However it may be noticed that this was attempted as described in section[4.5.2.4].

There was however the dilemma explained in section[4.5.2] of balancing between mesh quality and computational expense.

To conclude, it may well be that the described properties of the SGS modelling in FLUENT are to blame for some of the witnessed discrepancies in the LES simulation results.

9   Conclusions to discussion

From the RANS simulations of this thesis, it has been found that the RNG k-ε model indeed outperforms the SKE model when applied to the SRN IJF case like reported by ref[6].
This finding also includes the fact that the RNG k-ε model still outperforms the SKE model when the SKE mesh resolution is as much as 125 times higher, and makes use of enhanced wall treatment, as opposed to the wall function approach used for the RNG k-ε simulations.

The RANS simulated decaying rates of section[7.1.3] were found to follow a curve that could be approximated with expressions on the form:

$$ u = \frac{1}{\left(\frac{r}{D}\right)^n} $$

where n≈1-1.2 like displayed in Table 7.7 .
Further, the RANS simulations of different Re_0 values were not found to differ greatly from each other, yet some differences were found.
For instance the gradient of the velocity spreading of the high Re_0 simulations ($Re_0 = 230K$), was found to be lower than that of the low Re_0 simulations ($Re_0 = 23K$).
Overall the RANS simulations of this thesis are found to be of good quality, and upon comparison to be in good agreement with both the experimental and the simulated reference cases of refs[4, 6, and 8].

For the LES simulation of this thesis, very good agreement with experimental data is found close to the centre axis (r/D ≤ 1.5).
Outside this region, however, the agreement is found to deteriorate.
Following the analysis and discussion of sections[7 and 0], the observed deterioration with increasing r/D position for the LES simulation, is probably set in motion by one or a combination of the following points:

1. An abrupt change in the Δz grid spacing right above the boundary layer cells.
2. Skewed cell volumes in regions of the mesh.
3. SGS model is not designed to cope with skewed mesh volume-cells, and sudden grid changes.

As discussed in section[8.3], the under prediction of turbulence found in the LES simulation, is a likely to be caused by the above points 1-3.
The under predicted turbulence in turn, is a likely cause for the low spreading and decaying rates of the LES wall-jet velocity profiles reported and discussed in sections[7.1.3, 8.3.1].
Overall the LES simulation is seen to work excellently close to r/D=0.
However, the LES simulation approach is also found to be much more sensitive to simulation setup with regard to grid topography and simulation conditions than the RANS simulations.
According to the experiences gained from this thesis work, a LES simulation requires at least a good deal of preparatory work.
In addition, there will possibly be a need to do the LES simulation as an iterative process, where mesh design and boundary conditions gradually are found by means of trial and error.
In other words the LES approach proves far less robust, and a more difficult approach than the RANS approach.
It should therefore be questioned whether the LES approach in FLUENT is suited to treating problems where a verified solution is not known prior to the simulation.

Yet, a LES simulation can be of great use in supplying highly physically accurate data to simulation cases where an initial solution is available, or the flow has some features indicating whether the simulation is accurate or not.

Examples can be: the flow around a circular cylinder or sphere, or the IJF case.

In the problem definition of section[4.1], one of the goals of the thesis to test the LES option in FLUENT based on the following points:

- Added/reduced accuracy
- Simulation time consumption
- Computer resource requirements of simulation
- Model suitability as a tool for practical flow investigation.

From the experiences gained in this thesis, the strengths, weaknesses, and requirements of the LES approach places it more among the "scientific research tools", than among the "practical simulation tools".

It is true that the LES modelling adds accuracy to the solution in regions, and would probably give excellent results on the whole IJF domain if all initial and boundary conditions, and mesh properties, were ideal.

But the advantages of the LES approach come at a price.

The simulation was of this thesis required in excess of 11 days of physical simulation time, requiring in excess of 1 GB of memory.

Given the relative simplicity of the IJF geometry, the LES approach would thus indeed prove challenging if applied to some of the other geometries simulated for industrial and practical purposes today.

Hence the RANS approach will probably give the most reward for the simulation efforts, when applied to most practically motivated design and industrial simulations.

To summarize, a 2D RANS simulation on a 41K mesh would for most purposes be the most sensible and efficient approach to the IJF case with regards to computational expense, and simulation turnaround time.

10 Suggestions for improvements and further work.

The work reported in this thesis, has yielded some good and interesting findings about the IJF flow, presented in section[9].
In addition to these, there have been found some shortcomings, and areas for which the scope of the project has not allowed a thorough investigation.
In this section some areas where the project work with benefit could be improved or expanded are presented.

In terms of RANS simulations, the IJF case has both in this thesis, and earlier studies been well documented.
Nevertheless, the work of this thesis does not include any higher moment closure RANS simulations consult ref[7].
It would be particularly interesting to see how a good LES simulation performs compared to a RST RANS model.
In order to facilitate such a comparison, there would first have to be made some improvements to the LES simulation of this thesis in order to ensure better results throughout the whole IJF domain.
The improvements should probably comprise a more gradual transition from the boundary layer mesh to the general volume mesh. It may also be necessary to review the whole meshing approach for the domain in order to improve the volume-cell quality. Perhaps the simplest approach to this would be to mesh the whole domain like the centre region ($0 \leq r/D \leq 0.5$) was meshed for this thesis (consult   Figure 4.11).

Further, the initiation of field and boundary unsteadiness in the LES ought to be more thoroughly investigated.
This, since the work of this thesis never pinpointed the reasons for the disagreements related to the nozzle-jet profiles, observed in sections[7.1.4 and 8.3.4] and visualized in Figure 7.43 to Figure 7.42].
It would also be interesting to investigate what a good quality LES could provide of information about thermal phenomena.

11 Appendices
In the following appendices topics and elaborations relevant to understanding the theory and work incorporated in the thesis, are treated.

11.1 Appendix A

Calculation of step size:

In order to run the LES simulation, a value for the virtual time steps was needed.
The time step size was calculated as is shown in the following section:
Known quantities used in the calculation:

$$U = U_b = 3.45\frac{m}{s}$$

$$D_{\frac{1}{2}}: \text{Half the maximum Diameter of the domain} = 0.9m$$

$$\Delta x = \text{space between nodes in grid}$$

The Kolmogorov scales:
The Kolmogorov scales, are measures for the time, length and velocity of the smallest eddies of a flow before eddies dissipate as heat (Figure 3.6).
These scales are defined as:

$$\eta = \left(\frac{\nu^3}{\varepsilon}\right)^{\frac{1}{4}}$$

$$\tau = \left(\frac{\nu}{\varepsilon}\right)^{\frac{1}{2}}$$

$$v = (\nu\varepsilon)^{\frac{1}{4}}$$

Larger eddies have the time, length and velocity scales:
t,l, and u where l=u·t

This yields the following relations:

$$\frac{\eta}{l} = \left(\frac{ul}{\nu}\right)^{-\frac{3}{4}}$$

$$\frac{\tau}{t} = \left(\frac{\nu}{ul}\right)^{\frac{1}{2}}$$

$$\frac{v}{u} = \left(\frac{\nu}{ul}\right)^{\frac{1}{4}}$$

A common approximation for ε is to say that

$$\varepsilon \sim \frac{u^3}{l}$$

Where u is a typical magnitude of the turbulent fluctuation velocity, and l is a typical length scale for the eddies.

For simplicity the common assumption that $u \sim 0.1U = 0.345$ is used.

Further, since the goal is to determine the time step size needed to simulate the smallest resolved eddies in the LES simulation, the length scale l is set to be a typical grid point spacing in the mesh calculated thus:

$$l \sim \Delta x \sim \frac{\pi D_1/_2}{\# \Delta x} = \frac{0.9\pi}{280} \approx 0.01) : m$$

$$\varepsilon \sim \frac{u^3}{l} \sim \frac{(0.345)^3}{0.01} \approx 4.1 \left[{m^2}/{s^3} \right]$$

Now we have a value for ε, which will be put into τ equation below:

$$\tau = \left(\frac{\nu}{\varepsilon} \right)^{\frac{1}{2}} \approx 2.74 \cdot 10^{-3} [s]$$

With all probability the value for τ will not be the Kolmogorov time scale, since a length scale of the grid and not of the flow, and a very crude approximation to u, have been applied in order to calculate the value for ε.

However it may serve as an approximation for the described purpose.

By rearranging ()[τ/t equation], to

$$t = \frac{\tau}{\left(\frac{\nu}{ul} \right)^{\frac{1}{2}}} \approx \frac{1.9 \cdot 10^{-3}}{\left(\frac{1.5 \cdot 10^{-5}}{0.345 \cdot 0.01} \right)^{\frac{1}{2}}} \approx 0.03 [s]$$

There was always a great deal of doubt related to this calculation due to the rather liberal approach to the approximation of ε.

However as ref[experiments] report a sampling rate of 100Hz (t=0.01 seconds), at least the results from the calculation seemed credible in being of the same order of magnitude as the experimental sampling frequency.

However the author cannot rule out that a good deal of luck was involved in the good agreement between calculations and practised sampling rate.

The experimental sampling rate may also have been dictated by equipment limitations e.g. hence should not be relied too heavily upon.

However since the experiments would be used to benchmark the simulations, the time step size was decided to be within the same order of magnitude as the experiments.

Further since only a representative, and not the smallest Δx of the grid had been used to calculate Δt, the time step was set to the same as the Δt for the experiments being 0.01s.

A Δt of 0.01s was thus thought to be a rather well qualified assumption as to the time step needed to resolve the fluctuations of the in the flow.
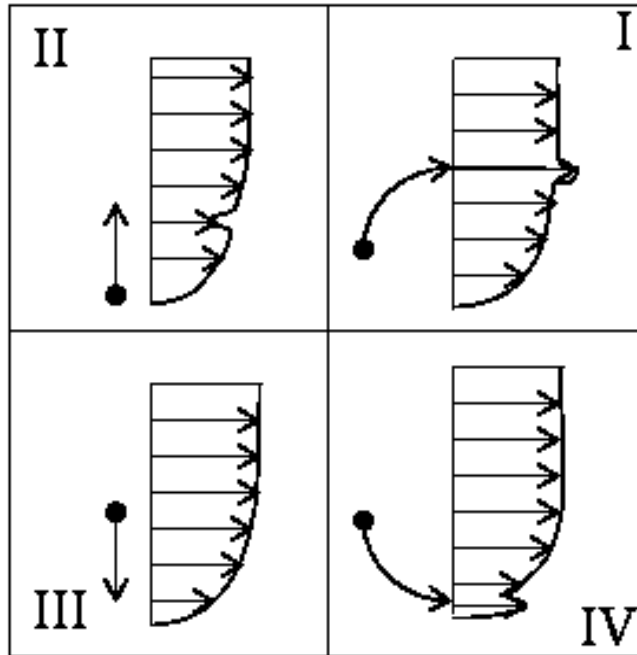
11.2 Appendix B
Quadrant analysis:

The quadrant analysis gives a quick and simple illustration of the basic physics behind the Reynolds shear stresses:

(1) $-\rho\overline{u'_i u'_j}$ for $i \neq j$.

The physics described in the quadrants can be represented as follows:

I: $[u' > 0,\ v' > 0] \Rightarrow \overline{u'v'} > 0$

Fluid element of high velocity moves out away from the wall adding to the mean velocity.

II: $[u' < 0,\ v' > 0] \Rightarrow \overline{u'v'} < 0$

Fluid element of low velocity moves out away from the wall, reducing the mean-flow velocity.

III: $[u' < 0,\ v' < 0] \Rightarrow \overline{u'v'} > 0$

Fluid element of low velocity moves inn towards the wall, not substantially affecting the mean flow.

IV: $[u' > 0,\ v' < 0] \Rightarrow \overline{u'v'} < 0$

Fluid element of high velocity moves inn towards the wall, adding to the near wall velocity gradient, and thereby increasing the shear stress on the wall.

Important implications:

The magnitudes of the contributions from quadrant II and IV far outweigh the contributions from quadrant I and III.

Simply put, turbulent motions in a flow contribute to give higher velocity gradients close to solid surfaces, at the cost a of reduced mean flow velocity.

This effect of turbulence can be illustrated by comparing the velocity profiles of a laminar and a turbulent pipe flow, in principle looking similar to A) and B):

A) Laminar pipe-flow velocity profile:
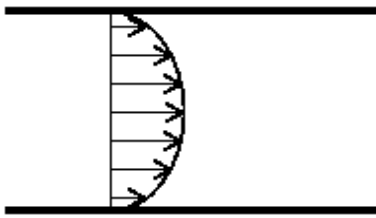
B) Turbulent pipe-flow velocity profile:
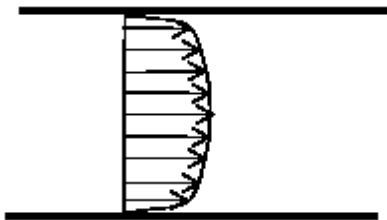
11.3 Appendix C
Data acquisition and processing program:

Below the basic functions of the data acquisition program is explained in general terms.
Then the code is listed in full, for more in detail information.
The data acquisition programme was made in order to simplify the extraction and processing of velocity profile data from fluent simulations.
The code was made and run in the programme Matlab 7.
The full programme comprises two modules.
In the first module labelled A_generator below, velocity profiles from different r/D positions are gathered from a directory where the files containing the actual data are listed descending from r/D=0 to r/D=9 at 0.025.
From these files a matrix is made, with odd numbered columns containing z position values, and even numbered columns containing velocity magnitudes.

The second module of the programme labelled Post_pros below, takes care of finding the maximum and half of the maximum velocities for each profile, with respect to z positions and velocity magnitudes.
Post_pros finds these quantities from the profiles read to A_generator, by calling A_generator as a function.

A_generator
§§§

```
function[A]=A_generator3D()
clear all;
% Denne koden henter først en liste med alle filnavnene i mappa
% 3D\Plot\vel-mag\
% Og så henter den ut data fra hver av filene og lagrer info verdier i A
list=dir('C:\Eirik08\Fluent\Ferdige simuleringer\3D\Plot\vel-mag');
l=length(list);
x=zeros;
u=zeros;
A=zeros;
G=zeros;

for t=3:l;
temp=importdata(['C:\Eirik08\Fluent\Ferdige simuleringer\3D\Plot\vel-mag\',list(t).name]);
sor=sortrows(temp,1); %sorterer kolonner etter x-verdi (temp,-1)->synkende x-verdi,
            %(temp,1)->stigende x-verdi: 2D bruk synkende,
            %3D bruk stigende
r=length(sor(:,1));
d=0.4-sor(:,1);    %Plukker ut posisjon NB!: skrevet for 3D
d=[d;0];
e=sor(:,2);    %Plukker ut hastighet
e=[e;0];
for s=1:r+1
A(s,(2*t)-5)=d(s);  %Limer inn posisjon
A(s,(2*t-4))=e(s);  %Limer inn hastighet
end
end
%oddetalls kolonner i A er posisjon, partall er fart
```
§§§

Post_pros

§§§

```
clear all
B=zeros;
[B]=A_generator3D;
B;

                %Finner verdier til umax-y plot
rows=length(B(1,:));
lager=zeros;

                %Genererer(:,5)lagermatrise, hvor kolonne1=x-verdier,
                %kolonne2=hast-verdier, og kolonne3=y-verdier, kolonne4=halv hastighets verdier
                %kolonne5= posisjon til halvhastigheter.
for i=2:2:rows;
lager((i/2),2)=max(B(:,i));
s=lager((i/2),2);
[r,col]=find(B==s);
row=max(r);          %finner x-verdien som ligger nærmest veggen dersom samme max verdi forekommer i to
punkter
xpos=B(row,i-1);
lager((i/2),1)=xpos;   %lagrer den x- verdien som ligger nærmest veggen dersom samme max verdi forekommer
i to punkter
lager((i/2),3)=(i/8)-0.25;
                % finner x-posisjon hvor u=0.5umax
Ud=0.5*s;
[c,d]=find(B(:,i)<=Ud); %finner posisjoner i matrise B hvor hast<= 1/2 umax
g=[c];                %lagrer alle disse matrise referansene (tall= vertikal pos i B) i vektor g
k=[find(g(:)>row)];    %finner alle elementer i g som ligger over umax
k;
q=k(1);              %finner første element i k ): første element hvor u<=1/2umax
[colpos]=g(q);
Uh=B(colpos,i);
lager((i/2),4)=Uh;     %finner til størrelsen til halvhastigheten Uh
lager((i/2),5)=B(colpos,i-1);  % finner x- verdien til Uh
end
lager
```

§§§

11.4 Appendix D

k-ε Turbulence Models
In the following, the SKE and RNG k-ε models used for simulations in this thesis are explored.
This appendix has been made with the help of ref[10]

11.4.1 The standard k-ε model:

$$\frac{D(\rho k)}{Dt} = \frac{\partial}{\partial x_j}\left[\left(\mu + \frac{\mu_t}{\sigma_k}\right)\frac{\partial k}{\partial x_j}\right] + G_k + G_b - \rho\varepsilon - Y_M + S_k$$

$$\frac{D(\rho\varepsilon)}{Dt} = \frac{\partial}{\partial x_j}\left[\left(\mu + \frac{\mu_t}{\sigma_\varepsilon}\right)\frac{\partial\varepsilon}{\partial x_j}\right] + C_{1\varepsilon}\frac{\varepsilon}{k}(G_k + C_{3\varepsilon}G_b) - C_{2\varepsilon}\rho\frac{\varepsilon^2}{k} + S_\varepsilon$$

Where:
G_k represents the generation of turbulent kinetic energy k, due to mean velocity gradients.
G_b represents the generation of k due to buoyancy.
Y_m represents the expansion of turbulence in compressible flows
$C_{1\varepsilon} C_{2\varepsilon}$ and $C_{3\varepsilon}$ are fixed constants
σ_k and σ_ε are turbulent Prandtl numbers for k and ε.
S_k and S_ε are source terms.

μ_t is the turbulent viscosity, modelled from the Boussinesque approximation as can be seen from ref[Durbin].
In the k-ε equation μ_t is modelled as:

$$\mu_t = \rho C_\mu \frac{k^2}{\varepsilon}$$

Standard fixed values for constants in the k-ε model in FLUENT are displayed below:

$$C_{1\varepsilon} = 1.44$$

$$C_{2\varepsilon} = 1.92$$

$$C_\mu = 0.09$$

$$\sigma_k = 1.0$$

$$\sigma_\varepsilon = 1.3$$

11.4.2 The RNG version of the k-ε model.

According to ref [10] the RNG k-ε model differs from the SKE model on the following points:

- The RNG model has an extra term(R_ε) in the ε transport equation aiming to improve solution accuracy for rapidly strained flows
- The RNG theory gives an analytical formula for turbulent Prandtl numbers, whereas these are treated as constants and have to be defined the SKE model.
- The RNG k–ε provides features to enhance solution performance on low Reynolds number flows.

Relying on the work of ref[6], the RNG k-e model seems to be the most accurate among the two equation models in fluent.

A strongpoint of the k-ε model is that it supports the use of a wall function (which is not the case e.g. for the k-ω model).

The equations for the RNG k-ε model are as follows:

$$\frac{D(\rho k)}{Dt} = \frac{\partial}{\partial x_j}\left(\alpha_k \mu_{eff}\frac{\partial k}{\partial x_j}\right) + G_k + G_b - \rho\varepsilon - Y_M + S_k$$

$$\frac{D(\rho\varepsilon)}{Dt} = \frac{\partial}{\partial x_j}\left(\alpha_\varepsilon \mu_{eff}\frac{\partial \varepsilon}{\partial x_j}\right) + C_{1\varepsilon}\frac{\varepsilon}{k}(G_k + C_{3\varepsilon}G_b) - C_{2\varepsilon}\rho\frac{\varepsilon^2}{k} - R_\varepsilon + S_\varepsilon$$

Where the different *C* AND *G* parameters are model constants, and the **S** terms are sink and source terms.

The main difference between the SKE and RNG k-ε model is said to be the R_ε term.
The R_ε term is modelled as follows:

$$R_\varepsilon = \frac{C_\mu \rho \eta^3 \left(1 - \frac{\eta}{\eta_0}\right)\varepsilon^2}{(1 + \beta\eta^3)k}$$

$$\eta \overset{\text{def}}{=} \frac{Sk}{\varepsilon}$$

$$\eta_0 = 4.38$$

β=0.012

In short this term adjusts the variations of ε depending on the $\frac{\eta}{\eta_0}$ ratio.

η describes the ratio of turbulent kinetic energy k, to turbulent dissipation ε, which among other things may help to improve near wall flow modelling ($\eta < \eta_0$), and the modelling of flow in heavily strained regions ($\eta > \eta_0$) (ref [10]).

The following model allows the RNG model to accurately describe low Reynolds number and near wall flows.
Equation below is integrated and solved for $\hat{v}$:

$$d\left(\frac{\rho^2 k}{\sqrt{\varepsilon\mu}}\right) = 1.72 \frac{\hat{v}}{\sqrt{\hat{v}^3 - 1 + C_v}} d\hat{v}$$

Where $\hat{v} = \frac{\mu_{eff}}{\mu}$ and $C_v \approx 100$

For high Reynolds numbers the turbulent viscosity μ_t again takes on the form known from the SKE model:

$$\mu_t = \rho C_\mu \frac{k^2}{\varepsilon}$$

Further α_k and α_ε are inverse effective Prandtl numbers $(Pr)^{-1} = \frac{k}{\mu c_p}$ (k here representing thermal conductivity).

α_k and α_ε are computed from expression below, which according to ref[10] is analytically derived by the use of renormalisation group (RNG) theory.

$$\left|\frac{\alpha - 1.3929}{\alpha_0 - 1.3929}\right|^{0.6321} \left|\frac{\alpha + 2.3929}{\alpha_0 + 2.3929}\right|^{0.3679} = \frac{\mu_{mol}}{\mu_{eff}}$$

$\alpha_0 = 1.0$
Where μ_{mol} is the molecular viscosity, and μ_{eff} is the effective viscosity further explained in ref[10].
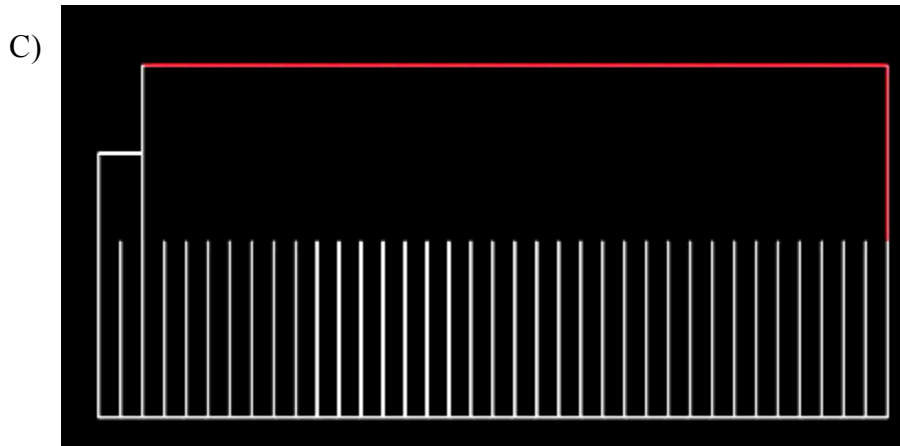
The rate $\frac{\mu_{mol}}{\mu_{eff}} \ll 1$ defines the limit between for what is regarded as a high and low Reynolds number flow ref[10].
For high Reynolds number flows $\alpha_k = \alpha_\varepsilon \approx 1.393$ yielding a $\frac{\mu_{mol}}{\mu_{eff}}$ ratio to be approximately 1.04.
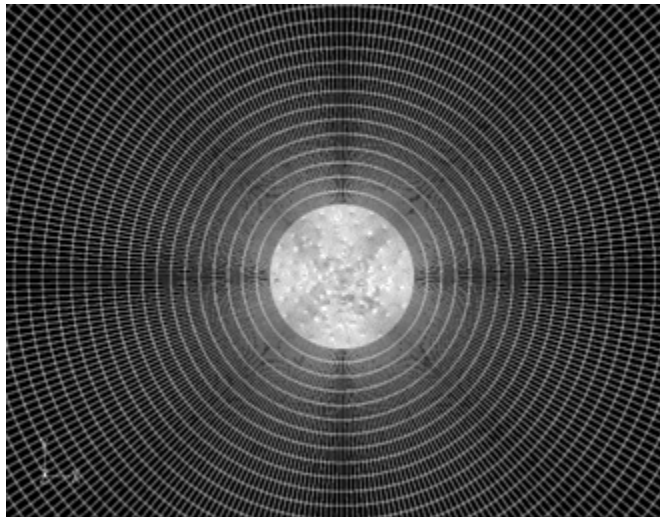
11.5 Appendix E
Grid pictures

In this appendix, pictures related to the meshes are presented with short explanations:
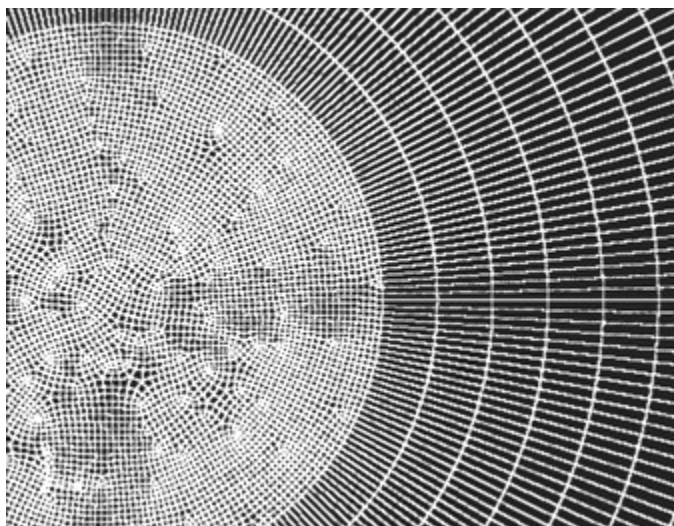
C)

C) Displays the lines from which values for the profiles are gathered.
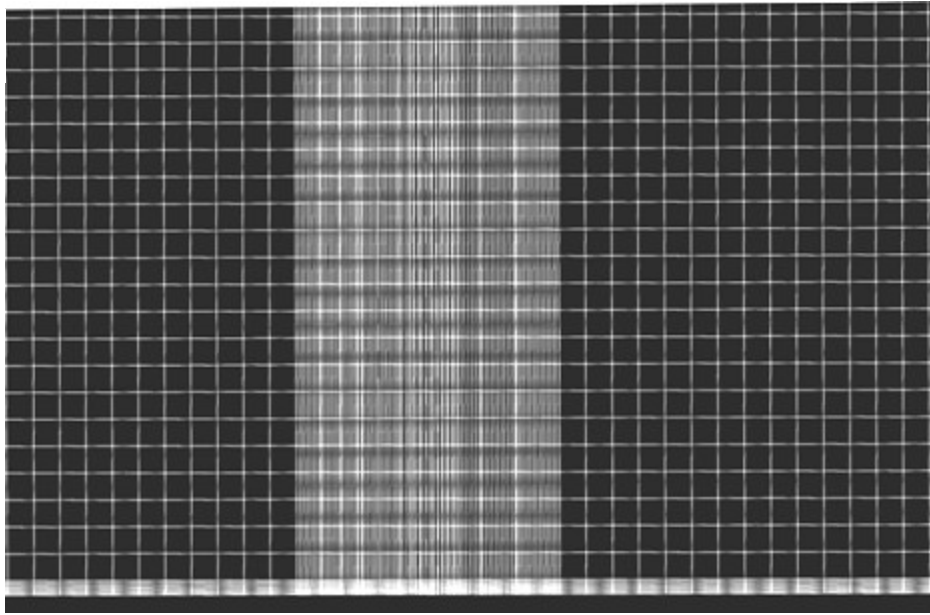
B)

B) Displays the centre of the 1.3M mesh seen looking down onto the impingement plane.
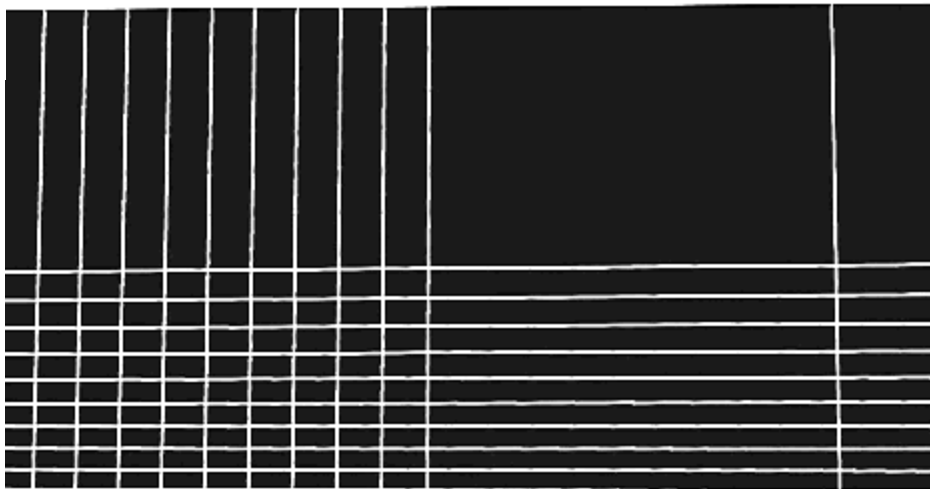
A)

A) Displays the centre of the 1.3M mesh seen looking down onto the impingement plane zoomed in compared to B).
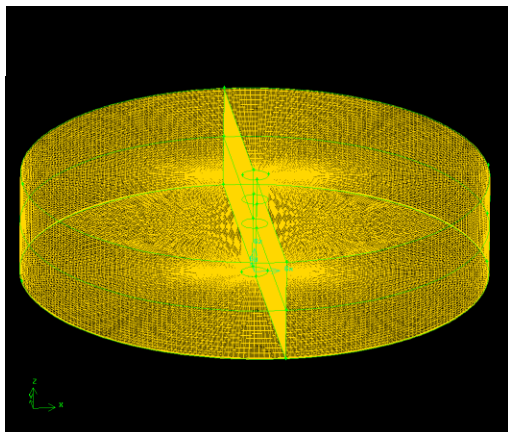
F)

F) Displays a side-view of the 1.3M mesh near to the impingement plane at the centre region.

E)

E) Displays a side-view of the 1.3M mesh near to the impingement plane where the centre region cylinder-mesh intersects the boundary layer mesh of the impingement plane.

D)

D) Displays the meshed surfaces or the 1.3M mesh.

113

12 References

1. Badra, J, Masri, A.R, Freeman, M, Fitch, M, 2007, Enhanced Heat Transfer from Arrays of Jets Impinging on Plates, 16. Australasian Fluid Mechanics Conference, University of Sidney, Australia

2. Balram,P, 2007, Review of article "Direct and Large Eddy Simulation of Turbulence by Joel H Ferziger ", lecture notes from course EP8405 Turbulence at NTNU during autumn semester of 2007, Trondheim, Norway

3. Bertin, J. J, 2002, Aerodynamics for engineers Fourth Edition. Prentice-Hall, Inc, New Jersey, USA

4. Cooper, D, Jackson, D.C, Launder, B.E, Liao, G.X, 1992, Impinging jet studies for turbulence model assessment-l. Flow-field experiments, Int.J. Heat Mass Transfer Vol.36, No 10, pp. 2675-2684

5. Cooper,D et al,1992, Case 25, "Normally Impinging Jet from a Circular Nozzle " http://cfd.mace.manchester.ac.uk/ercoftac

6. Coussirat ,M , van Beek, J, Mestres, M, Buchlin ,J.M , Escaler, X, 2005, Computational Fluid Dynamics Modeling of Impinging Gas-Jet Systems: 1.Assessment of Eddy Viscosity Models, Journal of Fluids Engineering vol 127, p.p:691-703

7. Durbin, P.A, 2004, Turbulence Closure Models For Computational Fluid Dynamics Encyclopaedia of computational mechanics, volume 3: Fluids John Wiley & Sons,Ltd New Jersey, USA

8. Oria Fernández, R, 2007, CFD applied to impinging gas-jet systems. Study of parameters-sensivity in production/dissipation terms in Eddy Viscosity Model equations, Thesis from: Escola Universitaria d'Enginyeria Tècnica Industrial de Barcelona (UPC), Catalunya, Spain

9. Ferziger, J.H, 1998, Direct and Large Eddy Simulation of Turbulence, Centre de
   Recherches Mathématiques CMR Proceedings and Lecture Notes
   Volume 16, pp: 53-97

10. *FLUENT 6.3 User's Guide , 2006
    Fluent, inc. New Hampshire, USA

11. GAMBIT 2.4 User's Guide , 2006
    Fluent, inc. New Hampshire, USA

12. Incropera, F.P, de Witt, D.P, 200?, Fundamentals of Heat and Mass transfer fifth
    edition, John Wiley & Sons,Inc. New Jersey, USA

13. White, F.M, 2006, Viscous Fluid Flow third edition
    McGraw-Hill, Inc. New York, USA

14. White, F.M, 2003, Fluid Mechanics Fifth Edition
    McGraw-Hill, Inc. New York, USA

13 Bibliography

Andersson, H.I, 1988, Introduction to Turbulence Modelling lecture notes in subject
76572 Turbulent Flow, Division of applied mechanics, Norwegian Institute of
Technology, Trondheim, Norway.

Coussirat ,M , van Beek, J, Mestres, M, Egusquiza, E , Buchlin ,J.M ,Valero, C, 2005,
Computational Fluid Dynamics Modeling of Impinging Gas-Jet Systems:
2.Application to an Industrial Cooling System Device, Journal of Fluids
Engineering vol 127, p.p:704-713

Davies, P.A, Valente, M.J, 1994, Recent Research Advances in the Fluid Mechanics of
Turbulent Jets and Plumes, NATO ASI Series E – Volume 255
Kluwer Academic Publishers, London, UK

de With, G, Holdø, A.E, 2005, The use of turbulent inflow conditions for the modeling of a
high aspect ratio jet, Fluid Dynamic Research 37, pp. 443-461

Introduction to the modelling of turbulence lecture series, 2000,
Von Karman Institute for Fluid Dynamics,
Rhode Saint Genèse, Belgium

Middleman, S, 1995, Modelling Axis symmetric Flows
Academic Press, Inc. San Diego, USA

Schlichting, H, Gersten, K, 2000, Boundary Layer Theory Eight edition
Springer, Inc. Heidelberg, Germany

Versteeg, H.K, Malalasekera, W, 1995, An introduction to Computational Fluid Dynamics-
The Finite Volume Method
Pearson Education, Inc. Harlow, Essex ,UK

Wheeler, J.A, Ganji,A. R, 2004, Introduction to Engineering Experimentation Second Edition Pearson Education, Inc. New Jersey, USA